ISTANBUL TECHNICAL UNIVERSITY ★ GRADUATE SCHOOL OF SCIENCE ENGINEERING AND TECHNOLOGY

REHABILITATION OF CORROSION DAMAGED SUBSTANDARD RC COLUMNS WITH USING FRP

M.Sc. THESIS

Aras KALYONCUOĞLU

Department of Civil Engineering

Earthquake Engineering Programme

JANUARY, 2013

REHABILITATION OF CORROSION DAMAGED SUBSTANDARD RC
COLUMNS WITH USING FRP

M.Sc. THESIS

Aras KALYONCUOĞLU
(501101205)

Department of Civil Engineering

Earthquake Engineering Programme

Thesis Advisor: Prof. Dr. Alper İLKİ

JANUARY 2013

İSTANBUL TEKNİK ÜNİVERSİTESİ ★ FEN BİLİMLERİ ENSTİTÜSÜ

STANDARTLARA UYMAYAN KOROZYON HASARLI BETONARME KOLONLARIN KARBON LİFLİ POLİMER KULLANILARAK GÜÇLENDİRİLMESİ

YÜKSEK LİSANS TEZİ

Aras KALYONCUOĞLU
(501101205)

İnşaat Mühendisliği Anabilim Dalı

Deprem Mühendisliği Programı

Tez Danışmanı: Prof. Dr. Alper İLKİ

OCAK 2013

Aras KALYONCUOĞLU, a **M.Sc.** student of ITU **Graduate School of Science Engineering and Technology** student ID **501101205**, successfully defended the **thesis** entitled "**REHABILITATION OF CORROSION DAMAGED SUBSTANDARD RC COLUMNS WITH USING FRP**", which he prepared after fulfilling the requirements specified in the associated legislations, before the jury whose signatures are below.

Thesis Advisor :   **Prof. Dr. Alper İLKİ**   ....
İstanbul Technical University

Jury Members :   **Prof. Dr. Mustafa ZORBOZAN**   ....
Yıldız Technical University

Assoc. Prof. Dr. Kutlu DARILMAZ   ....
İstanbul Technical University

Date of Submission : 17 December 2012
Date of Defense :   **30 January 2013**

If you can dream it, you can achieve it.
Z.Ziglar

FOREWORD

After a very long study period, I have finished my master degree thesis. Although, this thesis has been written by me, there are a lot of people who contributed to it in a direct or indirect way. I would like to express my gratitude to them. At first, I would like to thank to Prof. Dr. Alper İLKİ for all his suggestions, encouragements and guidance in approaching the different challenges during the thesis. His ideas and knowledge were guided me all the time during the thesis, hence his opinions extremely valuable for me.

Also I want to thank jury members, Prof. Dr. Mustafa ZORBOZAN and Assoc. Prof. Dr. Kutlu DARILMAZ for their support, vision and advisement which have helped to improve the quality of this thesis.

I am grateful to Dr. Çağlar GÖKSU for being a hidden heroine of this thesis. She was incredibly patient about me and whenever I need a help, she was a phone call away from me. This thesis would have been very poor and bad without her.

I would like to thank Pooya Ghaffari (M.Sc.) for all his effort on this thesis.

I am grateful to Res. Assist. Dr. Cem DEMİR, Ergün BİNBİR (M.Sc.), Res.Assist. Mustafa CÖMERT (M.Sc.), Hakan SARUHAN (M.Sc.) and Ali Osman ATEŞ (M.Sc.) contributions during the experimental phase of this thesis.

I am grateful to staff of ITU Structural and Earthquake Engineering and Building Materials Laboratories (Ahmet ŞAHİN and Mahmut ŞAMLI) for their excellent hard work and technical guidances, there would be no thesis without them.

Special thanks to my family (Afitap OKUYUCU, Raman KALYONCUOĞLU, Diclehan SÖNMEZOĞLU, Emre SÖNMEZOĞLU) and my fiancé (Neriman ERALP) for all kinds of financial and motivational support during my whole life.

January 2013

Aras KALYONCUOĞLU
Civil Engineer

x

TABLE OF CONTENTS

ABBREVIATIONS

$A_{core}^{confined}$	: Area of the confined core concrete
$A_{core}^{unconfined}$	: Area of the unconfined cover concrete
A_{frp}	: Area of the frp wrap
b	: Width of the rectangular member
CFRP	: Carbon-fiber reinforced polymer
f_y	: Yield tensile stresses of reinforceing bars
f_u	: Ultimate tensile stresses of reinforceing bars
f_{max}	: Maximum and ultimate tensile stresses of reinforceing bars
ε_{cc}	: Concrete strain corresponding to confined concrete compressive strength
ε_{co}	: Concrete strain corresponding to unconfined concrete compressive strength
E_{frp}	: Tensile elasticity modulus of CFRP
ε_{fu}	: Ultimate tensile strain of FRP;
$\varepsilon_{h,rup}$	: Ultimate tensile strain of FRP wrapped around concrete members
ε_y	: Yield strain of reinforcing bars
ε_{max}	: Maximum strain of reinforcing bars
ε_u	: Ultimate strain of reinforcing bars
f'_{cc}	: Confined concrete compressive strength;
f'_{co}	: Unconfined concrete compressive strength of the member at the day of testing.
f'_{co}	: Unconfined concrete
f_{cc}	: Confined compressive strength
f_{cd}^{unconf}	: Standard cylinder compressive strength of unconfined concrete
f'_l	: Effective lateral confinement pressure
FRP	: Fiber reinforced polymer
h	: Height of the rectangular member
k_a	: Confinement effectiveness factor
LVDTs	: Linear variable differential transformer
N_c	:The axial load capacity of the column without consideration of longitudinal bars
N_{cw}	:The axial load capacity of the column with consideration of longitudinal bars
r_c	: Corner radius of the rectangular section
RC	: Reinforced concrete
t_{wrap}	: Thickness of the FRP sheets
V_c	:Nominal shear strength capacity contributions from concrete
V_r	:Nominal shear strength capacity
V_u	:Nominal shear strength capacity
V_w	:Nominal shear strength capacity contributions from transverse reinforcement

V_s	**:** Nominal shear strength capacity contributions from transverse reinforcement
ρ_f of concrete	**:** Ratio of cross-sectional area of FRP jacket to the cross-sectional area
$\mu\delta$	**:** Displacement ductility factor
Pmax	**:** Maximum lateral load
δmax	**:** Lateral displacement corresponding to maximum lateral load
f'_c	**:** Standard cylinder compressive strength of concrete at 28 days

LIST OF TABLES

LIST OF FIGURES

xxii

REHABILITATION OF CORROSION DAMAGED SUBSTANDARD RC COLUMNS WITH USING FRP

SUMMARY

Due to increasing in country populations, building requirement is getting more important. Between 1960 and 1995, there have been 104% population increase in Turkey as like as other countries of the world. This breakneck population increment caused new building requirements such as building cooperations and apartments and this increase resulted as huge substandard reinforced concrete structure stock in Turkey. In those years, there were no seismic code or qualified engineers, who can design, control and check these buildings properly. There were some seismic and deisgn codes in foreign countries and the absence of any seismic or reinforced concrete design code in Turkey caused a building stock which had poor quality material. Even worse most of the buildings which built in that period, regulations and design codes were not taken into consideration. As a consequence, buildings which has been building after beginning of '60s in our country, which do not meet the standard codes, has potential of damage during the earthquakes. Turkey is in seismic zone and there have been a lot of grand earthquake happening and if 95% of Turkey lands are in seismic zone considered, size of the problem could be realized easily. Also these building stock have another huge problem which have been increasing due to time which is corrosion risk of the reinforced concrete elements. Especially in old existing buildings corrosion problem could be seen due to insufficient concrete cover, contain high percent chloride and low pH, temperature, water/cement ratio, humidity, insufficient using of vibration and problematic water drainage systems. Some defects due to workmanship or material on these building stocks could cause corrosion problem within the years. Corrosion causes significant decrease in drift capacity and strength due to cross-section loss of reinforcing bars, bond alteration between reinforcing bar and concrete, and cover cracking along the reinforcing bars on concrete. Although steel has a natural protector for corrosion reactions. The alkaline environment of concrete provides steel to corrosion protection (shown in Figure 2.4). At the high pH, a thin oxide layer forms on the steel and prevents metal atoms from dissolving. This passive film does not actually stop corrosion; it reduces the corrosion rate to an insignificant level. Because of concrete's inherent protection, reinforcing steel does not corrode in the majority of concrete elements and structures. However, corrosion can occur when the passive layer is destroyed. The destruction of the passive layer occurs when the alkalinity of the concrete is reduced or when the chloride concentration in concrete is increased to a certain level. All these corrosion damages will result in the loss of property and life in a possible earthquake if eventuated earthquake is considered in last 10 years.

Furthermore, if the reinforced concrete (RC) structure with corroded reinforcing bars, designed and built without complying seismic design codes, then it would be in urgent need of economic seismic rehabilitation/retrofitting.

Due to these reasons, an experimental study was carried out for investigating a rehabilitation/retrofitting procedure that improves the seismic performance of substandard RC columns (extremely low strength concrete, plain longitudinal bars, insufficient lap-splice zone, insufficient amount of transverse bars in the potential plastic hinge regions) with corroded plain reinforcing bars. Six symmetrically reinforced cantilever column specimens were constructed to provide relatively old and existing structures, which were built without complying the design codes as usually encountered in Turkey and in developing countries. Substandard structures means extremely low quality of concrete, unsufficient lap-splice length and plain round bars. Cross-sectional dimensions of columns were 200 mm × 300 mm and 1400 mm height and supported by a 700 mm × 700 mm × 500 mm foundation. All transverse bars spaces were 20 cm, it means there is no conforming transverse bars like as common usage. Clear cover was 20 mm from the transverse bars.

One of the specimens was choosen as reference specimen without any retrofit process. Then, the other specimens were subjected to accelerated corrosion process. Due to the accelerated corrosion process, the concrete cover became weak and deteriorated due to corrosion of reinforcing bars. After accelerated corrosion, corroded concrete cover was removed except the reference one, then steel reinforcement surfaces was cleaned from any concrete traces and rust of the corrosion products. All bars diameters were measured again with caliper for every 1 cm and compared with the uncorroded bars cross section to find cross section loss of the reinforcing bars. After cleaning process reinforcement of the specimens were covered with a corrosion inhibitor material to prevent corrosion. As a final step for specimens which will retrofitted by carbon fiber reinforced polymer sheets, were wrapped around the specimen externally one, two and three times in transverse direction with 150 mm overlap at the end of the wrap to enhance the deformability and to avoid potential shear failure due to increased flexural strength. FRP was recommended for its less disturbance to the occupants and hindrance of the functions of the structure. Then, the specimens were tested under constant axial load and reversed cyclic loads. The efficiency of the number of the ply of FRP sheet and the seismic retrofit technique for the case of low strength concrete column specimens with corroded plain reinforcing bars, which were subjected to reversed cyclic loading conditions were examined due to the indicators of seismic performance such as strength, displacement capacity, ductility, strain distribution, moment-curvature relationship and displacement components. Furthermore, the flexural strengths of the reference and retrofitted specimens are predicted analitically. Based on the results of limited number of reversed cyclic lateral loading tests on substandard RC columns with corroded plain reinforcing bars and extremely low strength concrete, the substandard columns cannot reach their theoretical flexural capacity due to loss of bond between concrete and reinforcement. A certain level of corrosion causes increase of friction between the bars and concrete leading to better bond and enhanced strength. Rehabilitation of corrosion damaged column with repair mortar enhanced the strength of the damaged column significantly, whereas ductility was only slightly improved with respect to corrosion damaged column. Rehabilitation and retrofitting using CFRP sheets enhanced both strength and ductility of the corrosion damaged column significantly up to a limit. However, wrapping of substandard RC columns with corroded plain reinforcing bars and extremely low strength concrete with more than two layer of CRFP reduced ductility due to corroded reinforcement bar sections and elongation request of bars while equalizing the section stability. It should be noted that before any CFRP application, elongations of bars and

statement of concrete should calculate carefully otherwise retrofitting with CFRP could also reduce both strength and ductility of substandard columns with corroded reinforcement due to rupture risk of corroded bars. Even CFRP increases both strength and ductility, local corrosion damages on the reinforcements can affect end reduce the behavior of specimen.

STANDARTLARA UYMAYAN KOROZYON HASARLI BETONARME KOLONLARIN KARBON LİFLİ POLİMER KULLANILARAK GÜÇLENDİRİLMESİ

ÖZET

Türkiye'de 60'lı yıllar ve sonrasında başlayan ve günümüze kadar devam eden hızlı nüfus artışı, nüfusun en önemli ihtiyaçlarından biri olan barınma ihtiyacını da beraberinde getirmiştir. Barınma ve konut ihtiyacının bu kadar hızlı artış gösterdiği bir dönemde bu ihtiyaçlar düzensiz ve problemli bir betonarme yapılaşma ile giderilmiştir. Bu problemli süreçte yapılmış olan yapılarda mevcut bir mühendislik hizmeti alımı söz konusu değildir. Yapılan yapıların üretim süreçlerinde deprem vb. dış etkilere karşı yapılmış detaylı bir yönetmelik bulunmaması, kullanılan malzemelerin herhangi bir standarda bağlı olmadan üretilmiş olmaları, günümüze kadar ki süreçte de o ya da bu nedenle hasarlı hale gelmiş ya da olası bir afette hasar görme olasılığı çok yüksek olan bir yapı stoğu oluşturmuştur. Günümüze kadar hızla artan bu yapı stoğu o dönemden bu döneme gerçekleşen depremlerde birçok mal ve can kaybına neden olmuştur ve olası gelecekteki depremlerde de can ve mal kaybına devam edecekleri aşikardır. Önceki dönemlerde yapılmış bu mevcut yapı stoğunun birçoğu, kullanılan malzemeler açısından hiçbir şekilde teste tabi tutulamamış, yapıldıkları dönemde sahip oldukları bir çok yapım ve plan kusurlarının yanı sıra yıllar içerisinde de o ya da bu nedenle belirgin düzeylerde hasarlara uğramışlardır.

Türkiye topraklarının %90'ının aktif fay hatları içerisinde yer alan deprem bölgeleri içerisinde bulunduğu göz önüne alınırsa, herhangi bir sismik harekette ya da gerçekleşebilecek bir afette bu yapıların ciddi hasarlar alabileceği, hatta yıkılabilecekleri, bunun sonucunda da büyük mal ve can kayıplarının ortaya çıkacağı gerçeği aşikardır. Bu sorunlu yapı stoğunun en büyük problemlerinden biride özellikle kullanılan beton kalitesinin düşük olması, paspayı mesafesinin bırakılmaması ve yıllar içerisinde aldığı kullanım hasarları nedeniyle betonarme elemanların içerisinde bulunan çelik donatıların korozyona uğramasıdır. Donatı korozyonu, yapı ve betonarme elemanların öteleme kapasitelerini donatı kesit alanlarında oluşan kesit kayıplarıyla doğru orantılı olarak düşürmekte, donatı ve beton arasındaki aderans kuvvetlerinin azalmasına ve donatı ile beton arasındaki yük aktarımının yitirilmesine neden olmaktadır. Bunların yanı sıra korozyona uğrayan çelik donatıların hacmi, çeliğin korozyona uğraması sonucu korozyon artıkları nedeniyle genişlemekte, bu da oluşturduğu basınçla beton örtüsünde çatlaklara neden olup betonun işlevini kaybetmesiyle sonuç vermektedir. Korozyona maruz kalmış betonarme yapıların deprem vb. yükler altındaki davranışı olumsuz yönde etkilenmekte, yapı dayanımlarını ve deprem performanslarını önemli ölçüde düşürmektedir.

Türkiye'de yer alan mevcut betonarme yapıların bir çoğunun önceki dönemlerde yapılmış olması, çeşitli nedenlerle korozyona maruz kalmış oldukları göz önüne alınırsa olası bir depremde bu tip yapıların neden olacağı can ve mal kaybı bir şekilde engellenmelidir. Mevcut yapı sayısının çok olması ve bu tip yapıların yıkılıp yeniden yapılabilmesi gibi durumlar ciddi bir ekonomik zorluktur. Ülkenin mevcut ekonomik

durumu ve halkın alım gücü göz önüne alındığında, yönetmeliklere uymayan hasarlı yapı stoğunun depreme karşı davranışının iyileştirilebilmesi için ekonomik rehabilitasyon/güçlendirme yöntemlerine acilen ihtiyaç vardır. Mevcut yöntemler ekonomik olmadıklarından dolayı yaşadıkları yapıları deprem ve etkilerine karşı iyileştirmek isteyen insanlar için masraflı olmakta güçlendirilmeyen binalarda büyük risk oluşturmaktadır.

Bütün bu nedenlerden dolayı bu tez çalışmasında ülkemizde bir çok yerde görülebilecek olan dikdörtgen kesitlere sahip kolonlar üzerinde deneysel bir çalışma gerçekleştirilmiştir. Yapılacak deneysel bir çalışma ile, donatıları korozyona uğramış betonarme kolonların güçlendirilmesi adına efektif ve ekonomik bir yöntemin bulunması amaçlanmış, elde edilecek deneysel sonuç veritabanları ile bu alanda ortaya çıkan sorunları çözmek adına inşaat mühendisliğine katkı yapılması istenmiştir. Korozyonun global bir problem olduğu göz önüne alındığında bulunacak basit bir yöntemin tüm dünyada ekonomik ve uygulanabilir bir sonuca sahip olacağı kesindir. Deneysel çalışmada kullanılan numuneler yönetmeliklere hiçbir şekilde uymayacak şekilde(çok düşük beton dayanımına, düz donatılara, yetersiz sıkılaştırma bölgesine, yetersiz donatı bindirme boyuna sahip) tasarlanmışlar ardından da yıllar içerisinde gözlenebilecek korozyon hasarlarını gerçekleştirebilmek için literatürde geçerli olan hızlandırılmış korozyon yöntemleriyle korozyona maruz bırakılmışlardır. Yönetmeliğe uymayacak şekilde tasarlanmış 6 numunenin 5 adedi hızlandırılmış korozyona maruz bırakılmaları sonucunda hasara uğramış, diğer numune ise referans olarak korozyon hasarının kolonlar üzerindeki davranış değişikliklerini tespit edebilme adına bırakılmıştır. Korozyona maruz bırakılan numunelerde oluşan korozyon sonucunda donatı hacimlerinde artış meydana gelmiş, artan donatı hacimleri betona basınç uygulayarak çatlaklara sebebiyet vermiştir. Bu numunelere güçlendirme işleminin yapılabilmesi için öncelikle mevcut korozyonun oluşturduğu hasarların temizlenmesi gerekmiştir. Korozyon hasarlarının tespit edilebilmesi için öncelikle bu korozyon sonucu oluşan çatlaklar ölçülmüş, ölçümler sonucunda korozyon oranları tespit edilmiştir. Ardından numunelerde oluşan korozyon hasarları ve artıkları, numunede paspayı mesafesinde bulunan beton örtüsünün kaldırılması ve açığa çıkarılan korozyonlu donatıların mekanik temizleyicilerle temizlenmesi sonucu ortadan kaldırılmış, beton örtüsünün kaldırılmasının ardından ortaya çıkan donatılar iki yönde de birer cm aralıklarla ölçülmüş ve korozyon kesit kayıpları belirlenmiştir. Kaldırılan korozyon hasarlı beton örtüsünün yerine, yüksek dayanımlı tamir harcıyla bir katman uygulanmış, korozyonlu betonun kaldırılması ve içerisindeki donatılarının temizlenip yeni bir tamir harcıyla tamir edilmesi sonucu, betonarme kolon iyileştirilmiştir. Ardından bir diğer kolon daha deney grubundan çıkarılmış geride kalan numuneler ise korozyonlu kısımlarının temizlenmesi ve tamir harcıyla onarılmasının ardından karbon katkılı lifli polimerler ile etriyelere paralel yerleşim olacak şekilde güçlendirilmiştir. Karbon lifli polimerler yapı strüktürel fonksiyonlarına minimum zararı veriyor olmasından, yapıda herhangi bir simetri kaybına neden olacak bir ağırlığı bulunmadığından dolayı bu tür yapılarda uygulanabilecek en iyi güçlendirme araçlarından birisidir. Güçlendirme işlemi 3 numunenin her birinin farklı kat sayısına sahip(1, 2 ve 3 kat) lifli polimerler ile sarılması ile gerçekleştirilmiştir. Güçlendirme işlemlerinin tamamlanmasının ardından bütün numuneler üzerine ölçüm cihazları yerleştirilmiş ve deprem davranışına en yakın düzeyde performans gösteren sabit eksenel yük altında tersinir çevrimli yüklemeyle teste tabi tutulmuştur. Test edilen numunelerde dayanım-deplasman kapasitesi, süneklik, uzama dağılımı, moment-eğrilik ilişkileri ve deplasman

bileşenleri incelenmiş güçlendirme şekillerinin ve güçlendirme de kullanılan CFRP kalınlığının sabit eksenel yük ve tersinir çevrimli yük altındaki davranışa etkisi incelenmiştir.

Yapılan deneyler sonucunda elde edilen dayanım, yerdeğiştirme kapasitesi, süneklik, donatıda oluşan şekil değiştirme dağılımı, moment eğrilik ilişkileri ve yerdeğiştirme bileşenleri değerlendirildiğinde, sabit eksenel yük ve tersinir çevrimli yük altında yapılan kısıtlı sayıda test sonucunda, içerisindeki donatıları korozyonlu ve nervürsüz olan, çok düşük beton basınç dayanıma sahip standartlara uymayan kolon numunelerde, donatılardaki korozyona bağlı olarak oluşan kesit kaybına ve beton ile donatılar arasındaki aderasyonun kaybolmasına bağlı olarak numune teorik eğilme kapasitesine ulaşamamıştır. Hızlandırılmış korozyon uygulanması sonucu numune donatılarında oluşan bir miktar korozyon, donatı ile beton arasındaki sürtünmeyi artırarak aderansı artırmış ve bu sayede korozyona uğramış düşük standartlı numune, korozyonsuz numuneden daha yüksek bir dayanım göstermiştir. Yine de eksenel yük ve korozyon sonucu oluşan beton hasarı, yeterli sıkılaştırma yapılmamış donatılarda burkulmaya neden olmuş bu da numune dayanımını bir anda düşürerek gevre bir davranış göstermesine neden olmuştur. Tamir harcıyla onarılmış numunede korozyonlu donatıların temizlenmesi sonucu oluşan pürüzlü donatı yüzeyi, nervürlü donatı gibi davranarak aderansı artırmış, buna bağlı olarak bir dayanım artışı tespit edilirken, herhangi bir gözle görünür süneklik artışı gözlemlenmemiştir. Numunelerin karbon lifli polimerler ile güçlendirilmesi numune davranışını hem dayanım yönünden hem de süneklik yönünden bir sınıra kadar artırmıştır. Ne yazık ki bu tip çok düşük beton dayanımına sahip kolonların lifli polimerler ile sarılması sonucu kesit içerisindeki tarafsız eksen kesit sınırına kaymış bunun sonucunda da korozyon hasarlı donatılarda oluşan uzama istemi, donatıların kopmasına neden olmuştur. Yine de elde edilen sonuçlar karşılaştırıldığında karbon lifli polimer kullanımının dayanıma ve sünekliğe bir noktaya kadar yarar sağladığı aşikardır.

Çalışmanın sonuçlarına bakıldığında, kullanılan güçlendirme ve iyileştirme yöntemlerinin dayanıma ve öteleme kapasitesine bir iyileştirme sağladığı fakat bu iyileştirmenin yine numunelerin standartların çok altında olmalarından dolayı yeterli olmadığı tespit edilmiştir. Gelecek çalışmalarda bu problemin çözümüne yönelik çalışmalar yapılmasına olanak tanıması nedeniyle elde edilen bilgilerin tüm betonarme yapılarda ortaya çıkan korozyon problemini çözmesi adına büyük yararlarının olduğu aşikardır.

xxx

1. INTRODUCTION

After 1950, there have been huge illegal and dense housing in Turkey parallel to population increment. In those years there were no seismic code or qualified engineers, who can design, control and check these buildings. By the 1990s, there were huge reinforced concrete structure stock in Turkey which built without seismic code or qualified engineers. When 95% of Turkey is in seismic zone considered, size of the problem can be realized easily. Some defects due to workmanship or material on these building stocks could cause corrosion problem within the years. Due to damage assessment report of İstanbul, which was published by İstanbul Büyükşehir Belediyesi first reason of the building damage was corrosion, because of humidity and the second one was unsufficient material using (Demirtas, 2008).

Especially in old existing buildings corrosion problem could be seen due to insufficient concrete cover, contain high percent chloride and low pH, temperature, water/cement ratio, humidity, insufficient using of vibration and problematic water drainage systems. If the 64% of the buildings were damaged because of corrosion is considered, new economic rehabilitation/retrofitting methods for these buildings is urgent. Because, corrosion is one of the major problem for especially substandard (extremely low strength concrete, plain longitudinal bars, insufficient lap-splice zone, insufficient amount of transverse bars in the potential plastic hinge regions) reinforced concrete buildings.

In this thesis new rehabilitation and retrofitting process is offered for substandard reinforced concrete columns with corroded steel reinforcement and experimental study was performed.

Nine chapters, a list of references, and one appendices are included in the thesis.

In chapter one, the aim of the thesis is described with a general introduction.

In chapter two, reinforced concrete, steel corrosion, and effects of the corrosion to reinforced concrete are described.

In chapter three, review of the effect of corrosion on mechanical properties of reinforcing bars, flexural behavior of RC members with corroded reinforcement, previous experimental and analytical studies on various constitutive bond stress-slip models available in literature, studies on corrosion monitoring of RC members, the emphasize of corrosion of reinforcing bars in relevant codes and standards are introduced.

In chapter four, the characteristics of specimens, and the test setup with its instrumentation are introduced.

In chapter five, rehabilitation and retrofitting process of the specimens are introduced.

In chapter six, theoretical predictions was calculated.

In chapter seven, test results are reported.

In chapter eight, the comparison of all column specimens with each other are reported.

In chapter nine, all thesis is concluded and some suggestians are made.

2. REINFORCED CONCRETE AND CORROSION

Concrete is a structural material which is mixing of aggregates, cement and water in a specific proportions. Cement is solidify after a time mixed with water and the aggregate is use for filler material which form the physical state of concrete .

Concrete has relatively low tensile strength and ductility thus, this deficiency is resolve with the reinforcement steel material which has high tensile strength and ductility. These steel reinforcing bars (rebar) is usually embedded passively in the concrete before it sets and this composite material is named as "Reinforced Concrete". Basically, the portland cement and the concrete is a natural protector for the reinforcement steel corrosion. But some defects due to workmanship or material like as insufficient concrete cover, contain high percent chloride and low pH, temperature, water/cement ratio, humidity, insufficient using of vibration and problematic water drainage systems especially in old buildings.

As a word, "Corrosion", comes from latin language "Corrosus", that means abrade, corrode (Gedikli, 2004). Corrosion can be explained as an electrochemical reaction between a metal and its environment that produces a deterioration of the material and its properties (ASTM G15-04).

Iron is the most used metal for reinforcing steel on constructions and as we commonly recognize it, iron is not generally found in nature because of its instability. It takes a great deal of energy to produce iron from its ore, and even then it is so unstable that it must be coated to keep it from reverting back to its ore forms. This process is called corrosion (URL-1).

For corrosion, there must be at least two metals, an electrolyte and a metallic connection must be in the process. In reinforced concrete, the rebar may have many separate areas at different energy levels. Concrete acts as the electrolyte, and the metallic connection is provided by wire ties, chair supports, or the rebar itself.

Corrosion is an electrochemical process involving the flow of charges (electrons and ions). At active sites on the bar, called anodes, iron atoms lose electrons and move into the surrounding concrete as ferrous ions. This process is called as a half-cell oxidation reaction, or the anodic reaction, and is represented as:

$$2Fe \rightarrow 2Fe^2 + 4e^- \qquad (2.1)$$

The electrons remain in the bar and flow to sites called as cathodes, where they combine with water and oxygen in the concrete. The reaction is represented as:

$$2H_2O + O_2 + 4e^- \rightarrow 4OH^- \qquad (2.2)$$

For keep the equation neutral, the ferrous ions migrate through the concrete pore water to these cathodic sites where they combine to form iron hydroxides, or rust:

$$2Fe^{+2} + 4OH^- \rightarrow 2Fe(OH)_2 \qquad (2.3)$$
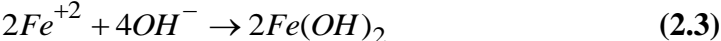
Electrochemical process of the corrosion is shown in Figure 2.1.

The increases in volume as the reaction products react further with dissolved oxygen leads to internal stress within the concrete that may be sufficient to cause cracking and spalling of the concrete cover.
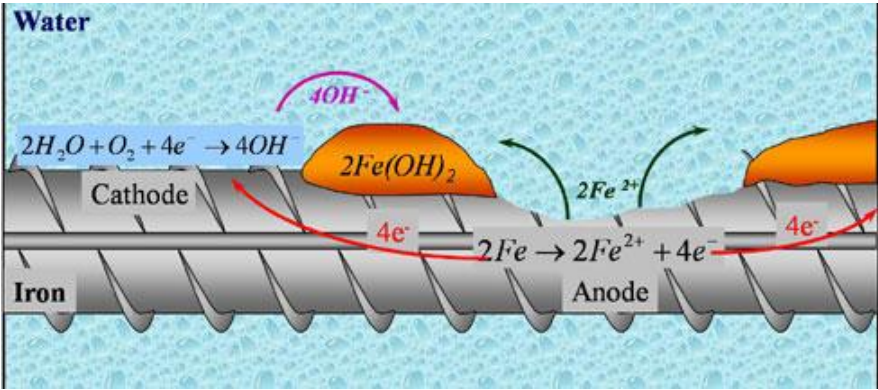
Figure 2.1 : Corrosion process on reinforced concrete steel bar (URL-1).
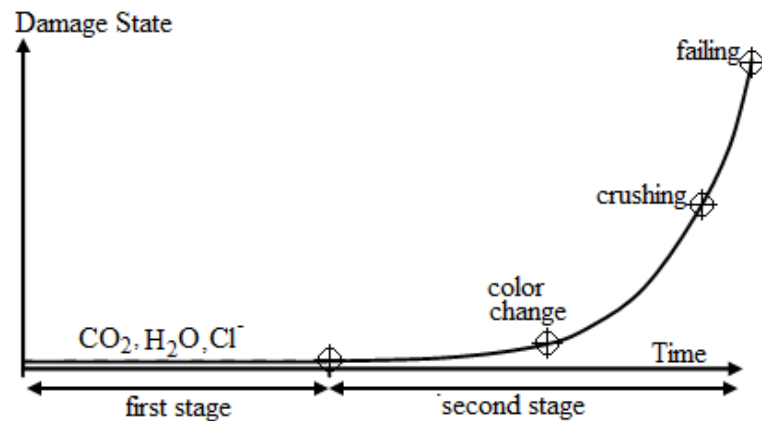
Figure 2.2 : Stage of corrosion on reinforced concrete with rusting (Gulikers, 2005).

Stage of corrosion in reinforced concrete with rust products are shown in Figure 2.2. As seen from the figure firstly uncorroded materials were exposed to CO_2, H_2O and Cl. After a time of exposure, concrete starts to change its color. After a time it starts to crushing and at last it fails.

The most common type of corrosion damage on reinforcing steel is pitting corrosion. Pitting corrosion is the localized corrosion type which a metal surface confined to a point or small area, that takes the form of cavities. Pitting corrosion is one of the most damaging forms of corrosion.

Pitting corrosion is usually found on passive metals and alloys such as aluminium alloys, stainless steels and stainless alloys when the ultra-thin passive film (oxide film) is chemically or mechanically damaged and does not immediately repassivate. The resulting pits can become wide and shallow or narrow and deep which can rapidly perforate the wall thickness of a metal. ASTM-G46 has a standard visual chart for rating of pitting corrosion. Due to ASTM-G46, standard visual chart for rating of pitting corrosion is shown in Figure 2.3. The shape of pitting corrosion can only be identified through metallography where a pitted sample is cross-sectioned and the pit shape, the pit size, and the pit depth of penetration can be determined. (URL-2)
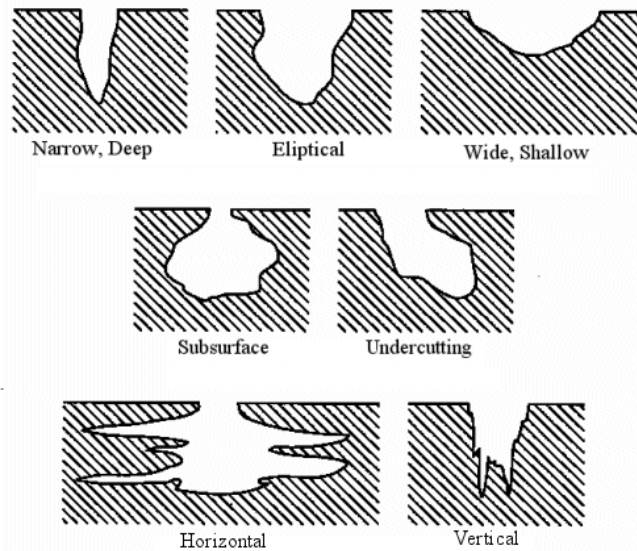
Figure 2.3 : Standard visual chart for rating of pitting corrosion due to ASTM-G46.

Although steel has a natural protector for corrosion reactions. The alkaline environment of concrete provides steel to corrosion protection (shown in Figure 2.4). At the high pH, a thin oxide layer forms on the steel and prevents metal atoms from dissolving. This passive film does not actually stop corrosion; it reduces the corrosion rate to an insignificant level. For steel in concrete, the passive corrosion rate is typically $0.1\mu m$ per year. Without the passive film, the steel would corrode at rates at least 1,000 times higher (ACI222, 2001).

Because of concrete's inherent protection, reinforcing steel does not corrode in the majority of concrete elements and structures. However, corrosion can occur when the passive layer is destroyed. The destruction of the passive layer occurs when the alkalinity of the concrete is reduced or when the chloride concentration in concrete is increased to a certain level.
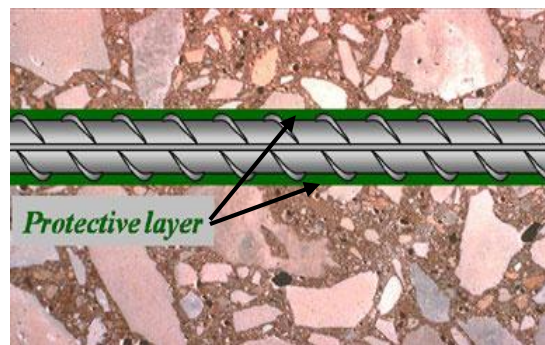
Figure 2.4 : Illustration of corrosion protector layer of steel (URL-1).

6

3. LITERATURE REVIEW

This section contains experimental and analytical studies from the literature. Effect of reinforcement corrosion in reinforced concrete have been studied by several researchers but, most of these researches were performed their studies in outside of Turkey. For this reason, typical problematic Turkish structure with substandard detailing were not taken into consideration in the studies which have been done.

Lee (1998) studied repair of reinforced concrete columns using CFRP sheets on seven large scale columns after subjected five of them to accelerated corrosion and the three of rest were repaired. Specimens have diameter size 305 mm and circular cross section. Accelerated corrosion was simulated by adding sodium chloride to the mixing water, applying a current to the reinforcement, and subjecting the column to wetting and drying cycles. For repair process two continuous layers of CFRP with a 4-inch overlap were applied. Corrosion-damage reduced the load carrying capacity of the specimens by 7%. The strain at ultimate load was also reduced. Repair of columns using CFRP sheets was quick and simple to use and CFRP repair increased the load-carrying capacity of the corroded columns by 28%.

Pantazopoulou et al. (2001) studied an experimental parametric study as a repair alternative for corroded structures. Several smallsize (300 mm in height and 150 mm diameter) concrete columns with various reinforcement configurations were subjected to accelerated corrosion to simulate natural corrosion damage the specimens. Then the columns were repaired using a variety of repair alternatives. Most of the repair schemes considered the damaged specimens with glass-fiber wraps, in combination with grouting the voids between the jacket and the original lateral surface of the specimen with either conventional or expansive grouts. All the repair options considered was slowing down the rate of the corrosion reaction, and imparting ductility and strength to the affected structural element. FRP wraps, being strong and corrosion-resistant, proved very effective as jacketing material. Compared with the conventional repair methods all the alternatives considered performed much better in terms of strength and durability. Performance was markedly improved when increasing the

number of FRP layers used in the jacket. Testing the performance of FRP-jacketed corroded members of rectangular cross sections, and consideration of combined flexure/axial load action in assessing the effectiveness of the repair schemes would be necessary prior to recommending general implementation of this technology to field applications.

Lee et al. (2002) studied on the retrofitting effects of reinforced concrete columns damaged by rebar corrosion strengthened with carbon fiber sheets. A cyclic horizontal loading test was carried out using RC columns damaged by different degrees of rebar corrosion and strengthened with CFS. As a result, it was revealed that the deterioration of their structural behavior was mainly caused by the decline in the confining effect due to the falling off of concrete cover and the reduction of mechanical properties of corrosion rebar. The local corrosion of hoops of an RC column, where axial force is dominant, causes fracture of the hoops and brittle shear failure due to the buckling of the longitudinal reinforcement when subjected to cyclic positive–negative shear forces as in earthquake. Shear strengthening using CFS is an extremely effective retrofitting method which prevents bond splitting cracks and shear cracks from growing and improves the ductility of RC columns with corroded bars because of the confining effects of CFS.

Bousias et al. (2002) studied seismic retrofitting of corrosion-damaged RC columns. RC columns which had 18-20 MPa concrete strength, corroded plain reinforcement bars were designed as not to fit regulations and seismic codes. Then these columns were retrofitted by using FRP and behavior of the specimens about different type and different layer number of FRP were examined under constant axial load and reverse cyclic load.

Wang et al. (2004) studied experimentally and analytically the behavior of fiber-reinforced plastic (FRP) retrofitted reinforced concrete beams, possessing a high chloride content and rebar corrosion under static loading. The test beams were characterized as falling into three different groups according to the state of their corrosion damage (natural corrosion, cathodic protection, and accelerated corrosion). The load carrying capacities of the beams, with or without FRP patching, were tested in the laboratory. The experimental results show that the state of corrosion of the steel, the water/cement ratio of the concrete material, and the arrangement and the number of FRP patches all affect the strength as well as the failure mechanisms of retrofitted

RC beams. Some simple analytical models and a design concept for retrofitting cracked and corroded RC beams with FRP sheets are also presented.

Tastani and Pantazopoulou (2004) studied experimental evaluation of FRP jackets in upgrading RC corroded columns with substandard detailing. Console columns which were 200 mm×200 mm size and 320 mm height with 30 MPa concrete strength were subjected to accelarated corrosion first, then some of them was retrofitted with EMACO-S66 which have 50 MPa concrete strength, some of them were retrofitted with CFRP (Carbon Fibre Reinforced Polymer) and the rest were retrofitted with both repair mortar and CFRP. Then the specimens were tested. For all retrofitting procedures, effective strength increase were examined. Ductile behavior were examined for the specimens which were retrofitted with CFRP.

Soudki et al. (2007) studied behavior of CFRP strengthened reinforced concrete beams in corrosive environment. Eight beams were cracked by subjected up to 300 wetting and drying cycles with deicing chemicals(3% NaCl) and repaired with CFRP sheets while the other three beams were kept uncracked as a control. All the specimens were subjected to an aggressive environment. The beams were 150 mm wide by 250 mm deep by 2400 mm long and reinforced with a reinforcement ratio of 0.6%. In addition, non-destructive test were performed to determine the corrosion rate, as well as destructive tests to determine chloride diffusion and reinforcing bar mass loss. Based on the findings of the study, the long-term effectiveness of the CFRP strengthened reinforced concrete in aggressive corrosive environments was established. CFRP strengthening significantly enhanced the performance of RC beams with the load capacity of almost double that of unstrengthened specimens. CFRP sheets and the resin system appeared to decrease chloride ionic diffusion and may reduce the corrosion rate of reinforcing steel in the beams. The ultimate capacity of the CFRP strengthened beams decreased by 11 to 28% over 300 cycles. The stiffness and yield load was not affected by the environmental exposure. Failure mode for a beam strengthened with CFRP strips was by debonding of the strips and the time to delaminate was shortened by increased wet-dry cycles.

Maaddawy (2008) studied about behavior of corrosion-damaged RC columns wrapped with FRP under combined flexural and axial loading. Console columns which were 125×125×500 mm sizes were casted with a concrete 28.5 MPa compressive concrete strength. Accelerated corrosion process were subjected and damaged columns due to

corrosion were rehabilitated with CFRP by wrapped the columns. Then performance of columns was studied under axial load. Wrapping process were applied by two different types, first full wrapping which whole column edge were wrapped and partly wrapping which is strip with 125 mm width on end-points of columns and with 65 cm strip on middle points of column with a 40 cm spacing. %26 strength improving were examined on partly wrapped columns and %40 strength improvin were examined on full wrapped columns as a results of experiments.

C. Goksu (2012) studied seismic behavior of rc columns with corroded plain and deformed reinforcing bars. Thirteen specimens which were classified into three different types, were produced and subjected to accelerated corrosion process then tested under constant axial load and reversed cyclic loads. The first type specimens were constructed using low strength concrete and plain reinforcing bars and with insufficient lap splices at column-footing connection to represent the existing relatively old structures built without complying the design codes. The second type specimens were designed and constructed according to current seismic design codes in Turkey. The third type specimen had the same characteristics with the first type specimens with an additional hook at ends of longitudinal bars lapped over at the column-footing connection. None of the specimens of the first type reached their theoretical capacity considering uncorroded reinforcing bar cross-sections. The slip of longitudinal bars dominated the behavior of specimens without corrosion and with low level corrosion. The bond strengths of heavily corroded specimens increased due to better bond conditions friction) by rust products on the surface of the plain bars and these specimens reached their theoretical capacity determined considering corroded reinforcing bar cross-sectional area, which is less than the theoretical capacity considering uncorroded reinforcing bar cross-sectional area.

As a result of literature review, there are a lot of research and researchers who studied about corrosion and rehabilitated performance of corrosion with FRP but, none of them were studied about rehabilitation of substandard columns because most of these researches were performed outside of Turkey. For this reason, typical problematic Turkish structure with substandard detailing were not taken into consideration and research on this topic is essential and urgent.

4. EXPERIMENTAL DESIGN

4.1 Design of Specimens

Six test specimens were constructed to provide relatively old and existing substandard structures in Turkey. Substandard structures means extremely low quality of concrete, unsufficient lap-splice length and plain round bars. Cross-sectional dimensions of columns were 200 mm × 300 mm and 1400 mm height and supported by a 700 mm × 700 mm × 500 mm foundation. Due to concrete compressive strength test results that made by another research in ITU (Goksu, 2012). The mean 28-day compressive concrete strength of the specimens are 3.7 MPa. The elastic modulus of the concrete was determined as 6200 MPa. All transverse bars spaces were 20 cm, it means there is no conforming transverse bars like as common usage. Clear cover was 20 mm from the transverse bars. The reinforcing cage and specimen details are shown in Appendix A.

Two different types of hot rolled reinforcing bars were used, bar with a 14 mm diameter were used for both starter and longitudinal bars, and bar with a 8 mm diameter were used for transverse bars. The mechanical characteristics of reinforcing bars are given in Table 4.1. In this table; fy, fmax, fu are yield, maximum and ultimate tensile stresses, and ε_y, ε_{max} and ε_u are the tensile strains corresponding to fy, fmax and fu, respectively.

Table 4.1 : Mechanical characteristics of reinforcing bars.

Reinforcing capacity bars		f_y [MPa]	ε_y	f_{max} [MPa]	ε_{max}	f_u [MPa]	ε_u
S220a	$\phi14$	337	0.0016	499	0.2148	366	0.2838
	$\phi8$	377	0.0018	494	0.1895	324	0.3202

Axial load capacity of the columns is calculated by using Eq. (4.1) and Eq. (4.2) which is 124 kN (55% and 30% of the axial load capacity of the column without and with consideration of longitudinal bars, respectively).

$$N_C = 0.5 \times (f_C \times b \times h) = 0.55 \times 3.7 \times 200 \times 300 = 122100\,N \qquad \textbf{(4.1)}$$

$$N_C W = 0.3 \times [(f_C \times b \times h) + (f_y \times \pi \times \frac{d^2}{4})] =$$
$$= (3.7 \times 200 \times 300) + (4 \times 337 \times \pi \times \frac{14^2}{4}) = 126850N \qquad \textbf{(4.2)}$$

The cyclic behavior of the columns was dominated by flexure damage. The average moment capacities of the columns were calculated as 34.2 kNm (Figure 4.1) by XTRACT(2007) computer program. For the moment-curvature analysis, the models proposed by Mander et al (1988) are used for unconfined and confined concrete stress-strain behavior. Steel reinforcing bars are assumed to behave in an elastic-plastic manner with strain hardening. Concrete and steel material models of reinforced concrete section is shown in Figure 4.2.
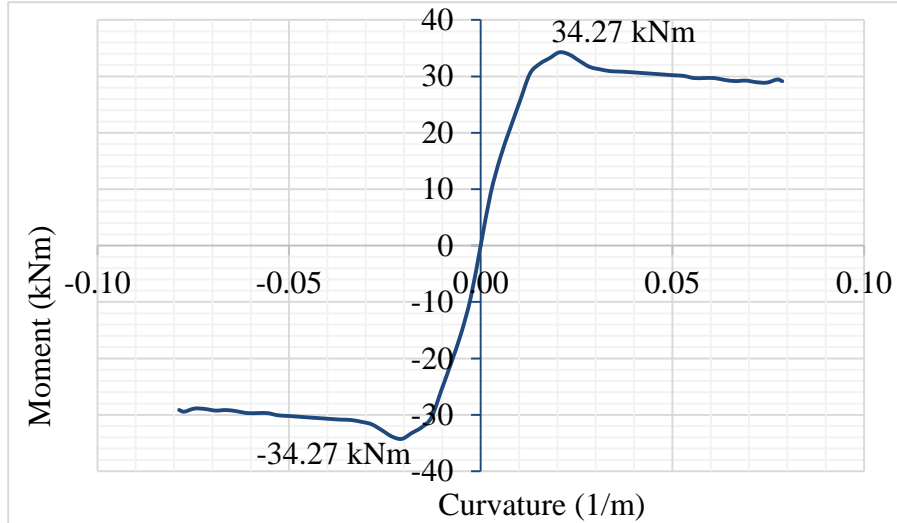
Figure 4.1: Theoretical moment-curvature relationships of the reference column.
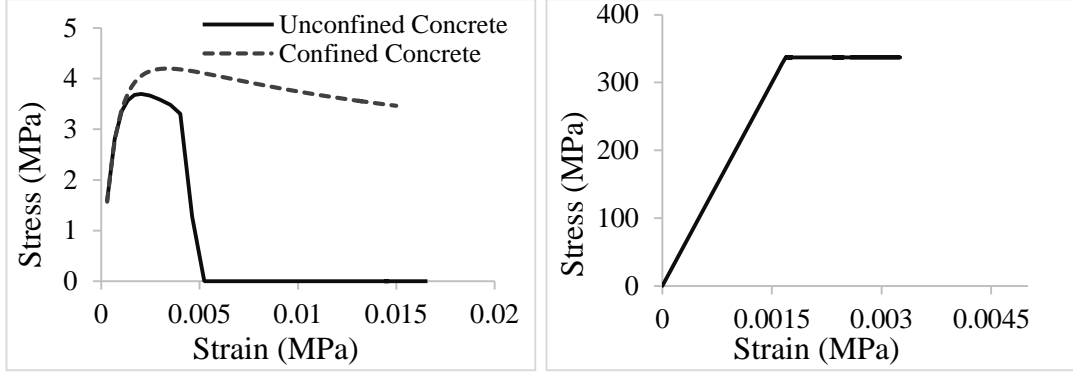
Figure 4.2: Concrete and steel material models of reinforced concrete section of reference column.

According to the theoretical calculation of the reference specimen, the column failure mode was with the crushing of concrete cover followed by crushing of core concrete and then yielding of longitudinal tension bar.

4.2 Shear Strength

For determination of shear strength capacity, three several models which where common and have been using in the world were used. These were TS500 (2000), Sezen and Moehle (2004) and ACI318 (2011).

According to TS500 (2000), the nominal shear strength capacity, V_r, is calculated as the sum of contributions from concrete, V_c and the transverse reinforcement, V_w. Results of materials tests are used in the calculations by dividing materials coefficients which are γ_{mc} and γ_{ms} taken as 1.5 and 1.15, respectively.

$$V_r = V_c + V_w \tag{4.3}$$

$$V_c = 0.8 \times V_{cr} \tag{4.4}$$

$$V_{cr} = 0.65 \times f_{cr} \times b \times (h - d\,') \times (1 + \gamma \times \frac{N}{b \times h}) \tag{4.5}$$

$$f_{ck} = \gamma_{mc} \times f_c = 1.5 \times 3.7 = 5.55 \text{ MPa} \tag{4.6}$$

$$f_{ct} = 0.35 \times \sqrt{f_{ck}} = 0.35 \times \sqrt{5.55} = 0.82 \text{ MPa} \tag{4.7}$$

$$V_{cr} = 0.65 \times 0.82 \times 200 \times (300 - 35) \times (1 + 0.07 \times \frac{122100}{200 \times 300}) = 32.335 \text{ kN} \tag{4.8}$$

$$V_c = 0.8 \times 32.335 = 25.86 \text{ kN} \tag{4.9}$$

$$V_w = \frac{A_{sw}}{s} \times f_{yw} \times d = \frac{2 \times \pi \times 8.37^2 / 4}{200} \times 378 \times \left[300 - 20 - (\frac{8.37}{2}) \right] = 57.36 \text{ kN} \quad \textbf{(4.10)}$$

$$V_r = V_c + V_w = 25.86 + 57.36 = 83.23 \text{ kN} \quad \textbf{(4.11)}$$

According to Sezen and Moehle (2004), the nominal shear strength capacity, V_r, is calculated as the sum of contributions from concrete, V_c and the transverse reinforcement, V_s.

$$V_r = V_c + V_s \quad \textbf{(4.12)}$$

$$V_c = k(\frac{0.5\sqrt{f'_c}}{\dfrac{a}{d}} \times \sqrt{1 + \frac{P}{0.5\sqrt{f'_c} \times A_g}}) \times 0.8 \times A_g$$

$$= 1(\frac{0.5\sqrt{3.7}}{\dfrac{1200}{265}} \times \sqrt{1 + \frac{122100}{0.5\sqrt{3.7} \times 200 \times 300}}) \times 0.8 \times 200 \times 300 = 17.99 \text{ kN} \quad \textbf{(4.13)}$$

$$V_s = k \frac{A_v \times f_y \times d}{s} = 1\frac{110 \times 378 \times 265}{200} = 55.09 \text{ kN} \quad \textbf{(4.14)}$$

$$V_r = 17.99 + 55.09 = 73.08 \text{ kN} \quad \textbf{(4.15)}$$

According to ACI318 (2011), the nominal shear strength capacity of concrete for members subject to axial compression, V_U, is computed by equation 4.16 where V_C is nominal shear strength provided by concrete and V_S is nominal shear strength provided by shear reinforcement.

$$V_u = V_c + V_s \quad \textbf{(4.16)}$$

$$V_c = 2\left(1 + \frac{N_U}{2000 \times A_g}\right) \times \lambda \times \sqrt{f_c'} \times b_w \times d$$

$$= 2\left(1 + \frac{27449.17}{2000 \times 11.81 \times 7.87}\right) \times 1 \times \sqrt{536.64} \times 7.87 \times 10.43 = 4364.608 \text{ lb} \quad \textbf{(4.17)}$$

$$V_c = 19.41 \text{ kN}$$

$$V_s = \frac{A_v f_{yt} d}{s} = \frac{0.1705 \times 54824.25 \times 10.43}{7.87402} = 12381.83 lb \quad \textbf{(4.18)}$$

$$V_s = 55.07 \text{ kN}$$

$$V_u = V_c + V_s = 55.07 + 19.41 = 74.487 kN \qquad (4.19)$$

According to calculations, the nominal shear strength capacity of the specimens were found as 83.23 kN, 73.08 kN and 74.487 kN according to TS500 (2000), Sezen and Moehle (2004) and ACI318 (2011).

4.3 Accelerated Corrosion

As known the corrosion is a long term process that effect the earthquake performance of the buildings widely. For this reason accelerated corrosion method was used for get shorten that process. All specimens except the reference one were exposed to accelerated corrosion for modelling the real corrosion effects.

For accelerated corrosion, calcium chloride was added in the mixing water during concrete casting. The weight of calcium chloride was 4% of cement weight (cement weight: 384.4 kg, $CaCl_2$: 14.8 kg). After casting, to increase the corrosion rate even more, calcium chloride solution was sprayed from the outer sides of the specimens and a fixed potential of 6 Volts was applied. Longitudinal and transverse cracks occured at the specimens after the accelarated corrosion process. The crack pattern of specimens due to corrosion is presented in Figure 4.3.

Previos studies pointed out a reduction in concrete compressive strength after the reinforcing bars in the respective reinforced concrete number have corroded. However, concrete compression test results obtained for core specimens that were extracted from the columns with heavily corroded reinforcing bars, showed that there was no significant change in the compressive characteristic of concrete for the speciments tested in this study. A similar result was also obtained for the mechanical characteristics of reinforcing bars, which were taken from the unccorroded region. For this reason the mean 28-day compressive concrete strength of the specimens and were taken as 3.7 MPa for all specimens.

Figure 4.3: Photos of the cracked sections on specimens.

4.4 Test Setup

4.4.1 Testing Procedure

All specimens were tested at Istanbul Technical University Structural and Earthquake Engineering Laboratory. The transverse load was applied at the top of the specimen, approximately at 1200 mm height from the base of the column with a MTS hydraulic actuator of 250 kN capacity. An axial load of 124 kN (55% and 30% of the axial load capacity of the column without and with consideration of longitudinal bars, respectively) was applied by using a hydraulic jack at the top of the columns. Two 6-wire-strand post tensioning tendons were used for applying the axial load. Steel tendons were passed through inside of the bottom steel beam to the steel beam which located at top of the column. Axial load was given by using these steel tendons and the hydraulic jack. The load was measured by load cell which was located on the jack. All specimens were tested under axial load and reversed cyclic load. Test setup is shown in Figure 4.4, Figure 4.5 and Figure 4.6.
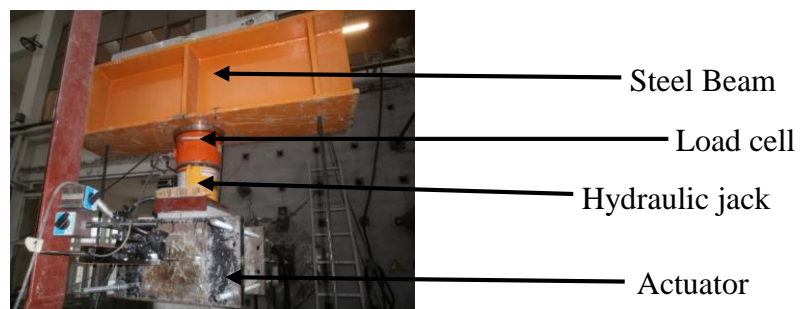
Figure 4.4: Axial Load Setup.

a)   b)

Figure 4.5: Test Setup.

— Steel Beam

— Load cell
— Hydraulic jack
— Actuator

— Post tensioning
tendons

— Column
— Reaction
Wall

— Footing

— Adaptor
foundation

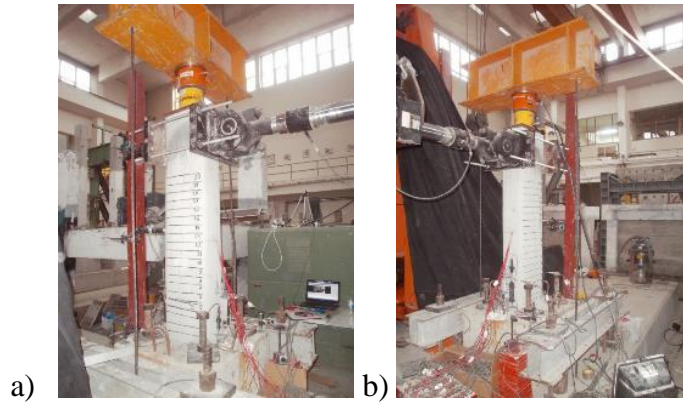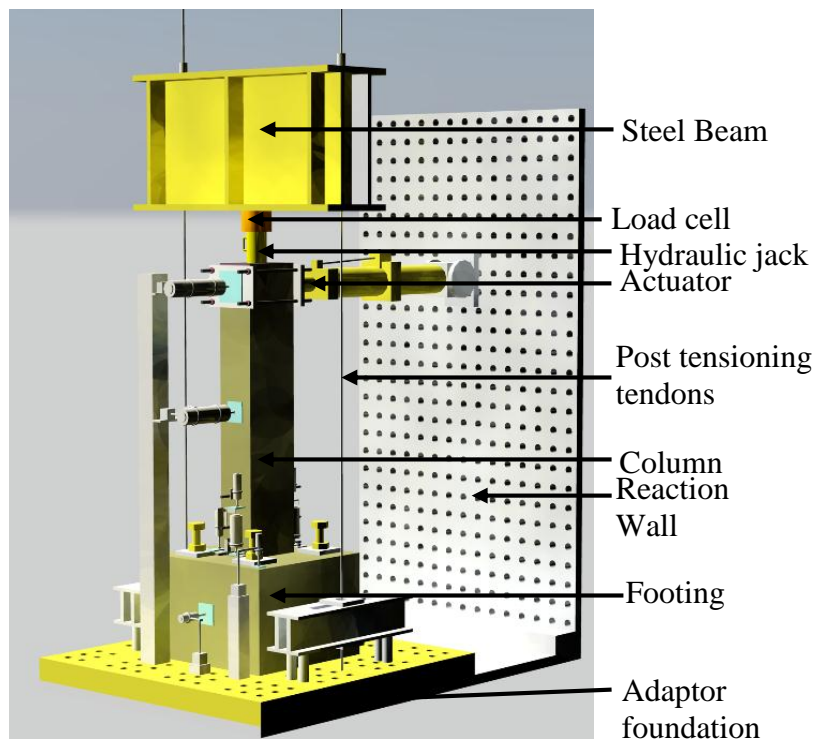**Figure 4.6:** Test Setup.

4.4.2 Test Setup

TML transducers, YFLA-5 strain-gauges, TML-CLC-50A load cell, the interior load cell and interior transducer of MTS actuator were the instrumentation equipment. The data of these instruments reached TML TDS 303 data logger through TML ASW-50B switch box.

4.4.2.1 LVDT's

One of the most important thing in the experimental studies are installing the measuring system. Therefore, LVDTs were used to estimate the column displacements during the test. The LVDT or Linear Variable Differential Transformer is a well established transducer design which has been used throughout many decades for the accurate measurement of displacement and within closed loops for the control of positioning. Six LVDTs were placed parallel to the column bottom up in 20 mm, 150 mm and 300 mm evaluate curvature values of the specimens. Two of six were CDP50 which have 50 mm gage length and rest of the LVDTs were CDP25 which have 25 mm gage length. For the lateral displacement of the column, a reference LVDTs which was SDP200 (200 mm gage length) were placed to tip of the column length and another one which was CDP100 (100 mm gage length) were placed to mid of the column length. Two LVDTs which were CDP5 (5 mm gage length) were placed on the footing for measuring the rotations and another LVDTs which was CDP10 were placed horizontally at the midpoint of the footing for measuring the possible footing displacements. The locations of the LVDTs are shown in Figure 4.7.
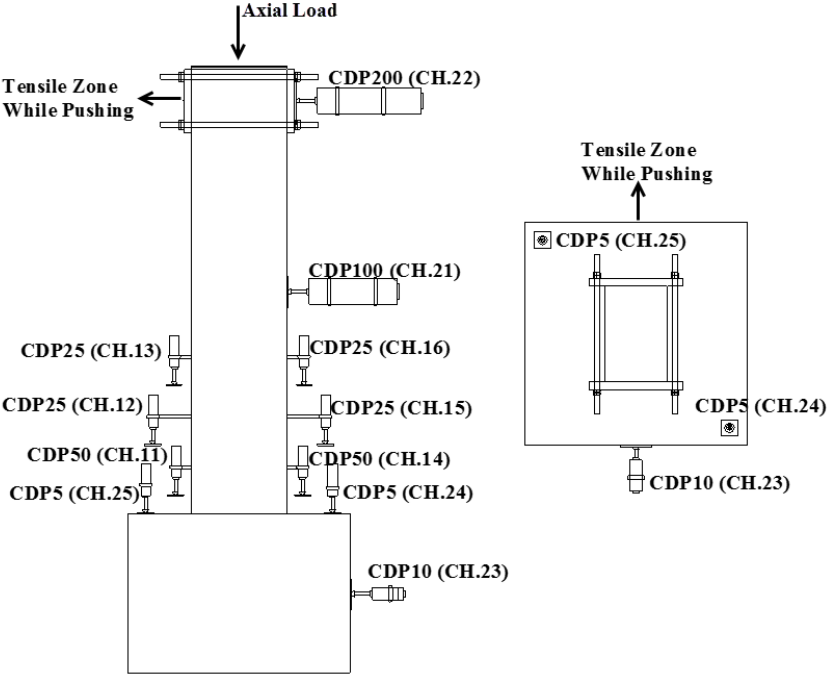

Figure 4.7: Locations of the LVDTs.

4.4.2.2 Strain-Gauges

Straingauges are using for monitoring the elongation and shortening of the longitudinal bars and transverse reinforcement. "A strain gauge (also strain gage) is a device used to measure the strain of an object. Invented by Edward E. Simmons and Arthur C. Ruge in 1938, the most co mmon type of strain gauge consists of an insulating flexible backing which supports a metallic foil pattern. The gauge is attached to the object by a suitable adhesive. As the object is deformed, the foil is deformed, causing its electrical resistance to change. This resistance change, usually measured using a wheatstone bridge, is related to the strain by the quantity known as the gauge factor." (URL-3). 16 strain-gauges were used for each of the specimens.

Before attach the strain-gauges, place which strain-gauge attach was clean with coarse and sharp corundum. Strain-gauges were glued to totally cleaned places on bars with a glue that including cyanoacrylat. After adhered the strain gauges, those were wrapped with the N-1 waterproof material and VM Tape for the humidity and other external factors. Notes and numbers were written on the cables for understand which strain-gauge was where. All strain-gauges were tied in bunches and were takeoff from nearest point on concrete.
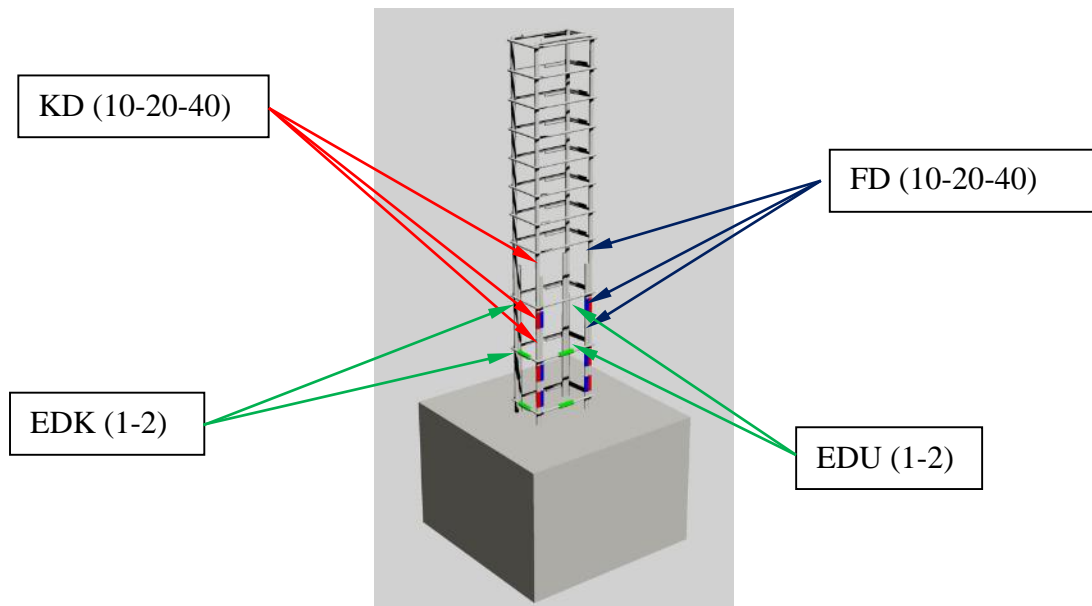

Figure 4.8: Strain-Gauge locations.

Table 4.2 : Strain-gauge location plans, names and factors.

Strain Gauge Name	Adhesion Distance (mm)	Gauge Factor	Attached Column				
			X26-REF2	X26-M	X47-M-CFRP1	X43-M-CFRP2	X44-M-CFRP3
KD40-4	400	2.10 ±%1	✗	✔	✔	✔	✔
KD20-4	200	2.10 ±%1	✗	✔	✔	✔	✔
KD10-4	100	2.10 ±%1	✗	✔	✔	✔	✔
FD40-4	400	2.10 ±%1	✗	✔	✔	✔	✔
FD20-4	200	2.10 ±%1	✗	✔	✔	✔	✔
FD10-4	100	2.10 ±%1	✗	✔	✔	✔	✔
KD40-3	400	2.10 ±%1	✔	✔	✔	✔	✔
KD20-3	200	2.10 ±%1	✔	✔	✔	✔	✔
KD10-3	100	2.10 ±%1	✔	✔	✔	✔	✔
FD40-3	400	2.10 ±%1	✔	✔	✔	✔	✔
FD20-3	200	2.10 ±%1	✔	✔	✔	✔	✔
FD10-3	100	2.10 ±%1	✔	✔	✔	✔	✔
EDU1	50	2.10 ±%1	✔	✔	✔	✔	✔
EDU2	250	2.10 ±%1	✔	✔	✔	✔	✔
EDK1	50	2.10 ±%1	✔	✔	✔	✔	✔
EDK2	250	2.10 ±%1	✔	✔	✔	✔	✔

Six strain-gauges were attached to both of tension and compression bars at 10 cm, 20 cm and 40 cm heights at both of starter bar and column bars(FD10, FD20, FD40, KD10, KD20, KD40). Two strain-gauges were attached to first and second short side of transverse bars(EDK1 and EDK2). Two strain-gauges were attached to first and second long side of transverse bars(EDU1 and EDU2). Strain-gauge location plans, names and factors shows on Table 4.2 and Figure 4.8.

4.5 Loading History

Loading history is the one of the most important thing in experimental studies and many loading histories have been proposed in the literature. A test may carried out under deformation control or force control within the elasctic or the inelastic range. Deformation controlled loading history method is applicable to components whose seismic response is controlled by a deformation parameter such as displacement, rotation or shear distortion. In this thesis, deformation controlled reversed cyclic loading history was chosen for all specimens for simulate the dynamic load effects of

earthquakes which were suggested by FEMA461. The deformation was controlled by using top displacement values of column. Suggested deformation controlled loading history of FEMA461 is given in Figure 4.9 where Δ_0 and Δ_m are the targeted smallest and targeted maximum deformation amplitude of the loading history. In this thesis modified version of FEMA461 which had used by Goksu (2012) was used and displacement have been controlled by drift ratios.
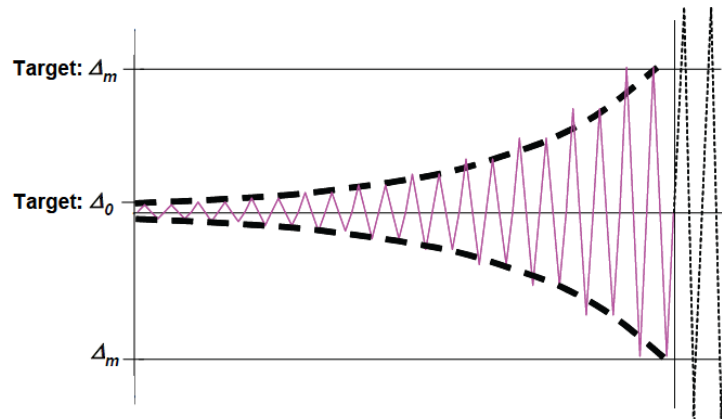

Figure 4.9: Sketch of deformation-controlled loading history.

Drift ratios(d/L) were calculated as the ratio of the lateral displacement of the top of the column(d) to column length(L). Loading history of the specimens are shown in Figure 4.10. The loading history was composed of excursions at certain drift ratios (±0.0010 (±1.2 mm), ±0.0025 (±3.00 mm), ±0.0050 (±6.00 mm), ±0.0075 (±9.00 mm), ±0.0100 (±12 mm), ±0.0150 (±18 mm), ±0.0200 (±24 mm), ±0.0250 (±30 mm), ±0.0300 (±36 mm), ±0.0350d (±42 mm), ±0.0400 (±48 mm), ±0.0450 (±54 mm), ±0.0500 (±60 mm), ±0.0600 (±72 mm), ±0.0700 (±84 mm), ±0.0800 (±96 mm)) for pulling and pushing cycles.
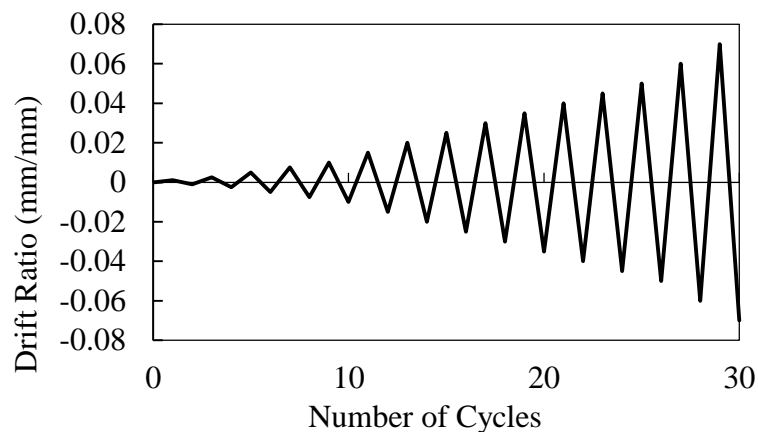

Figure 4.10: Loading history of the specimens.

5. SPECIMEN REHABILITATION/RETROFITTING

All the specimens except reference one were subjected to rehabilitation/retrofitting process. One specimen was rehabilitated while the rest of the specimens were both rehabilitated and retrofitted. Rehabilitation/retrofitting methods for each specimen is given in Table 5.1. This section contains rehabilitation / retrofitting process of the specimens.

Table 5.1 : Specimen rehabilitation/retrofitting types.

Specimen Name	Rehabilitation Type	Retrofitting Type
X26-REF2	-	-
X26-M	Repair Mortar	-
X47-M-CFRP1	Repair Mortar	1 Layer of CFRP
X43-M-CFRP2	Repair Mortar	2 Layer of CFRP
X44-M-CFRP3	Repair Mortar	3 Layer of CFRP

5.1 Measuring the Crack Widths on Specimens

Before any process on the specimens, all cracks measured with a crack measuring card from three different part of the specimens. Most of the corrosion damage and section lose were occured on the foundation, column joint section at the specimens. For this reason first part was 0-15 cm section of the column specimens for determine how much crack width occur cause of the corrosion lose. Second part was 15-60 cm and it shows the lap-splice area. And the last one shows the least corroded place. Crack measuring for 0-15 cm section is shown in Figure 5.1.

Figure 5.1 : Crack measuring of the specimen.

5.2 Cleaning of Cover Concrete and Corrosion Products

After the crack width measurement, two of the six specimens were taken as a reference and corroded concrete cover of the specimens were clean except reference. Hydraulic crusher and peen ha mmer were used for the cover concrete cleaning process. The weak concrete cover was removed until the longitudinal bars were exposed for avoiding premature cover spalling off.

Since generally the cover concrete is weak and deteriorated due to corrosion of internal reinforcing bars in case of sub-standard existing RC structures built with low quality concrete, the process of removing of concrete cover does not require a significant effort. When concrete cover cleaned, longitudinal and transverse bars were cleaned also by using metal brush. Cover concerete cleaned specimen is shown in Figure 5.2.
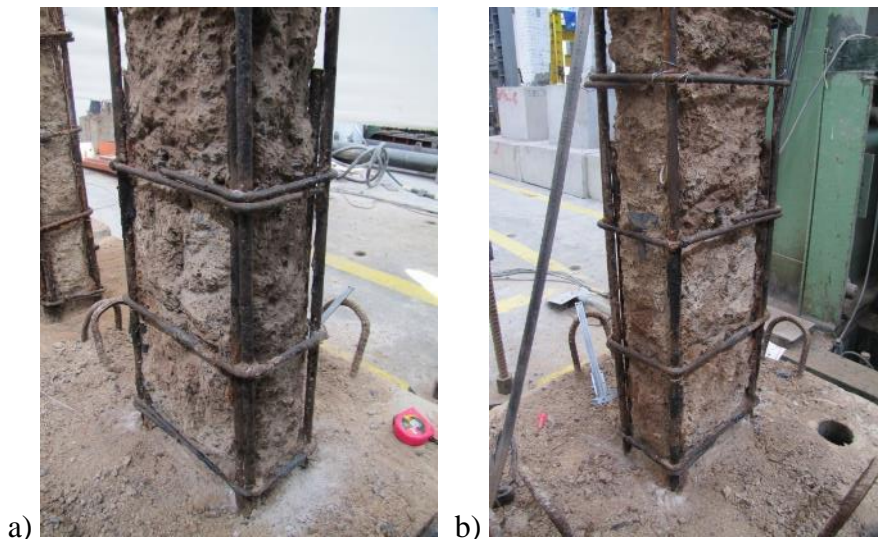

a)   b)

Figure 5.2 : Concrete cover cleaned specimen.

In the notations of the specimens, the first specimen identifier denotes the cross-section loss (X) of the reinforcing bars and the second identifier denotes the rehabilitation/retrofitting procedures which were used on specimens. The cross-section loss (X) of the reinforcing bars because of corrosion was determined by dividing the difference between initial and the existing cross-sectional area.

All bars diameters were measured again with caliper for every 1 cm and compared with the un-corroded bars cross sections. Marked bars is shown in Figure 5.3. The

existing cross-sectional area after corrosion was determined by dividing the bottommost 300 mm part of four longitudinal bars of each specimen into 10 mm long pieces, and averaging or taking the minimum diameters of each 10 mm long piece both in 0º and 90º directions after mechanical cleaning of the rust on reinforcing bars. The difference in determining the cross-sectional losses of reinforcing bars for specimens was due to different failure modes of the specimens. Minimum cross-section is taken into consideration for X47-M-CFRP1, X43-M-CFRP2 and X44-M-CFRP3 due to their failure mode were rupture of the starter bars, while average cross-section is consider for other specimens.
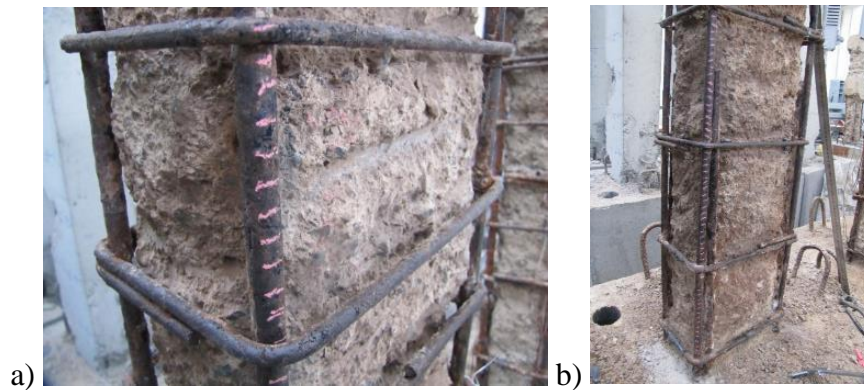

Figure 5.3 : Marked bars for measuring on specimens.

Peak and average section loses were determined for all specimens except X0-REF1-REF1 and these values is given in Table 5.2. It should be noted that reinforcement bar diameter values of X26-REF2 was measured in autopsy step after test performed. Average diameter of the un-corroded longitudinal and starter bar was 14.55 mm.

Table 5.2 : Diamaters and section loss of the reinforcement longitudinal bars.

Specimen Name	Bar #1 (mm)	Bar #2 (mm)	Bar #3 (mm)	Bar #4 (mm)	Average Section Loss %
X26-REF2	12.50	12.84	11.76	12.89	26%
X26-M	12.50	12.84	11.76	12.89	26%
X47-M-CFRP1	11.39	11.51	11.15	7.94	47%
X43-M-CFRP2	11.24	8.31	11.77	12.31	43%
X44-M-CFRP3	10.17	11.20	10.32	11.88	44%

5.3 Measuring the Crack Widths on Specimens

In previous part the concrete cover was cleaned mechanically. Steel reinforcement surfaces was cleaned from any concrete traces and rust of the corrosion products. After cleaning process reinforcement of the specimens were covered with a corrosion inhibitor material Masterseal 300T. This material prevents is an anti-corrosion coating and primer which is protect the reinforcement from corrosion. Applying of corrosion inhibitor material is shown in Figure 5.4.

Figure 5.4 : Specimens were covered with a corrosion inhibitor material.

After the corrosion inhibitor dried, specimens strengthened with EMACO S88 repair mortar with no gap around columns. Strengthening process of the specimens is shown step by step in Figure 5.5
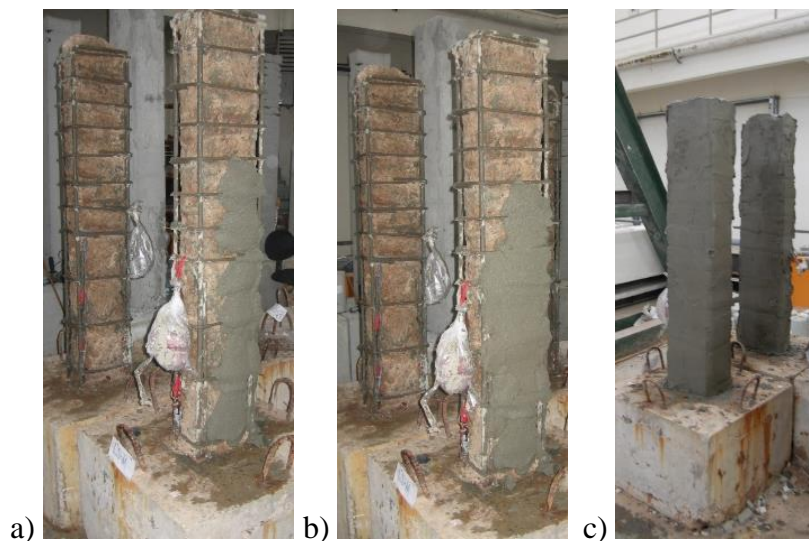

a)   b)   c)

Figure 5.5 : Rehabilitation process of the specimens with repair mortar.

As a final step for specimens which will retrofitted by carbon fiber reinforced polymer sheets, were wrapped around the specimen externally one, two and three times in transverse direction with 150 mm overlap at the end of the wrap to enhance the deformability and to avoid potential shear failure due to increased flexural strength. Retrofitting process of the specimens with CFRP is shown step by step in Figure 5.6. Other functions of CFRP sheets wrapped around the members in transverse direction were to contribute to the bond between the core concrete and repair mortar, and to contribute to prevention of buckling of internal steel. It should be noted that, all retrofit application was carried out within the thickness of the original concrete cover.

a)   b)   c)
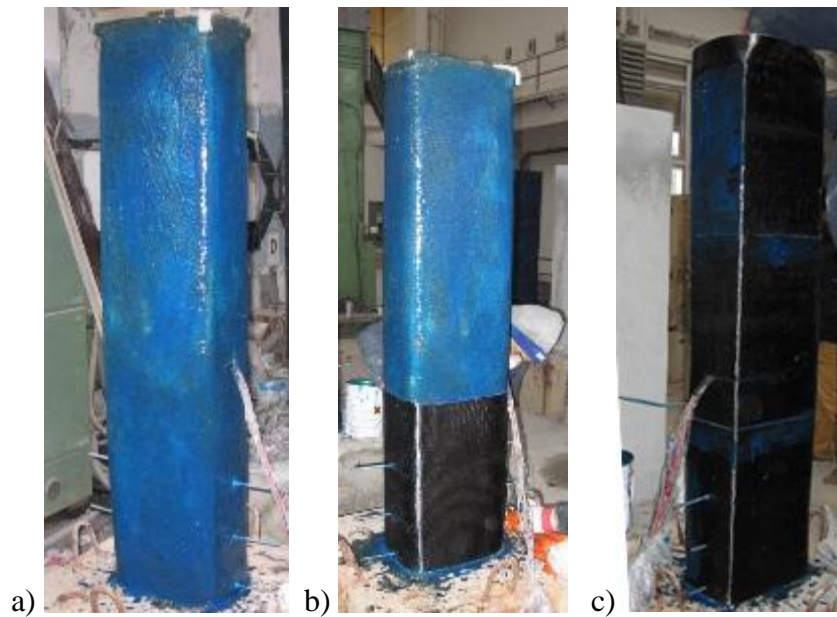
Figure 5.6 : Retrofitting process of the specimens.

The mechanical characteristics of the CFRP sheet, as given by Telateks Company, are presented in Table 5.3. In this table, t_f, w_f and E_f are the effective thickness, the effective width and the tensile elastic modulus of CFRP sheet. The compressive strengths of the cement based structural repair mortar, the epoxy adhesive mix used in wrapping CFRP sheets in transverse direction to the member surface were 50 and 60MPa (after 7 days of age), respectively.

Table 5.3 : Characteristics of CFRP sheet.

	E_f [N/ mm^2]	t_f [mm]	w_f [mm]	Ultimate strain
CFRP Sheet	245000	0.17	500	0.018

6. THEORICAL STUDY

Theorical predictions of X26-REF2 and X26-M were calculated by using method which proposed by Mander et al. while X-47-CFRP1, X-43-CFRP2 and X-44-CFRP3 were calculated by using Mander et al. after unconfined part of the section had calculated according to method suggested by A.İlki et al. for the CFRP strengthened beams. Diameter of bars were taken from Table 5.2. Then the section was modelled as given in Figure 6.1 for X26-REF2. Contrubition of cracked cover concrete of X26-REF2 was disregarded in calculations. Moment – curvature diagram for X26-REF2 was given in Figure 6.2.
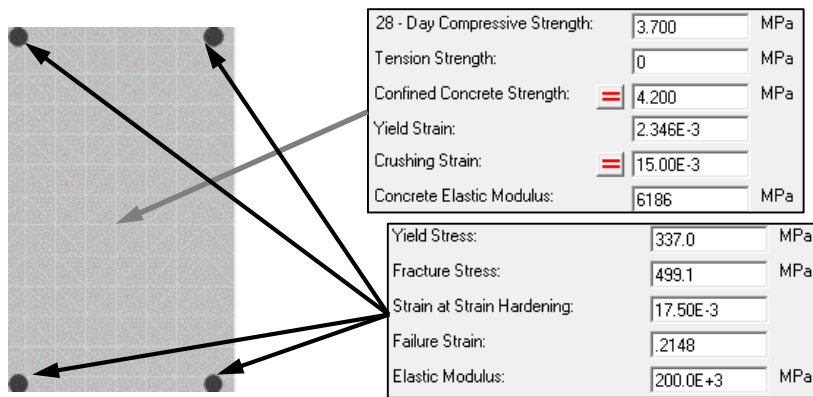
Figure 6.1 : Theorical section and material properties of X26-REF2 specimen.
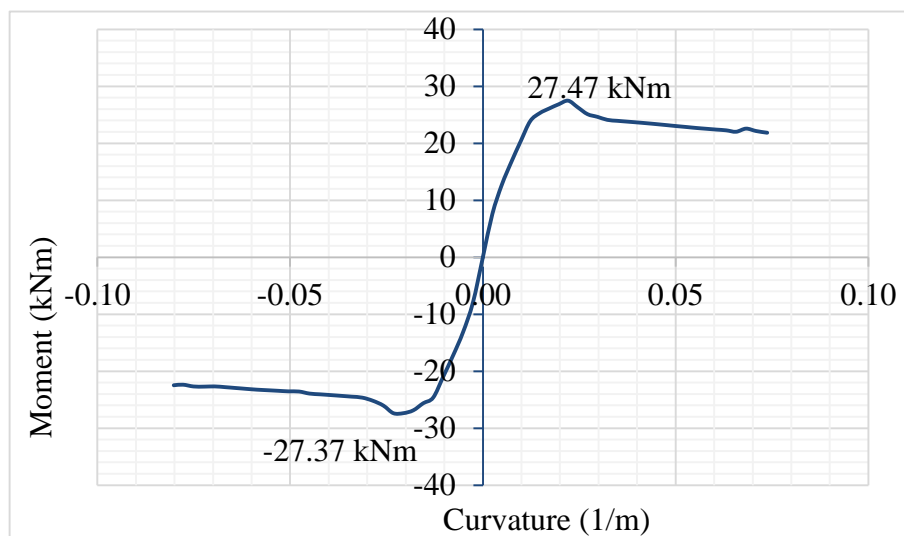
Figure 6.2 : Theorical Moment – Curvature Diagram of X26-REF2 specimen.

The section was modelled as given in Figure 6.3 for X26-M. Properties of unconfined concrete were taken from manufacturer firm of EMACO S88. Moment – curvature diagram for X26-M was given in Figure 6.4.
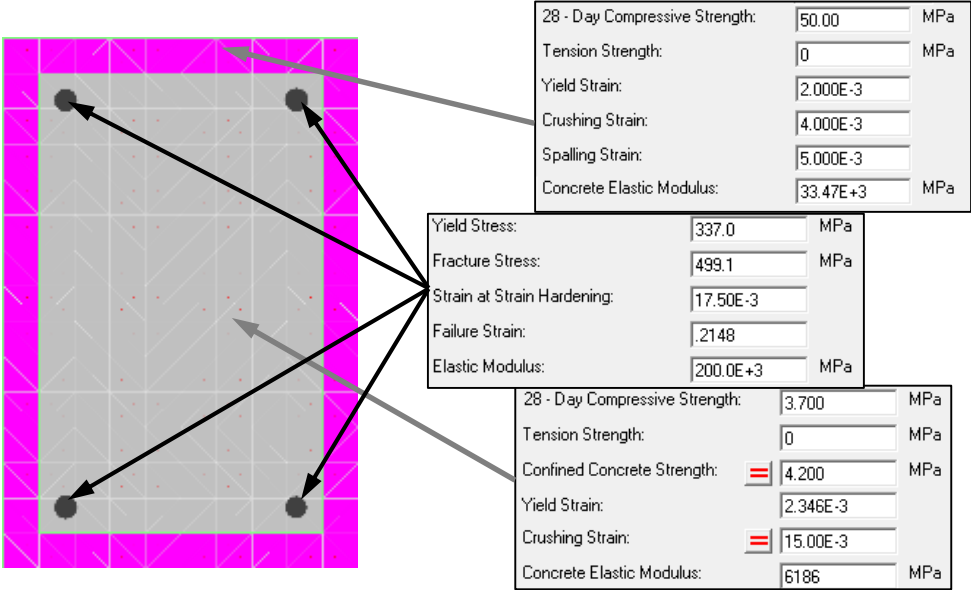

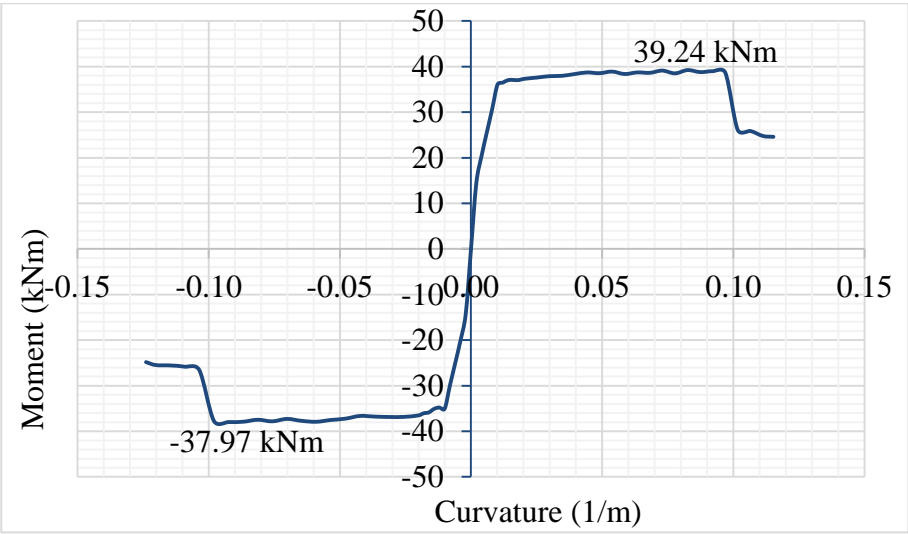**Figure 6.3 :** Theorical section and material properties of X26-M specimen.

Figure 6.4 : Theoretical Moment – Curvature Diagram of X26-M specimen.

For calculation of theorical moment capacity of X47-M-CFRP1, effect of confined concrete was calculated by using the method which proposed by Mander et al. and effect of unconfined and CFRP sheets together was calculated by using the method which proposed by A.İlki et al.. For X47-M-CFRP1, calculation steps of f'_{cc} and ε_{cc} according to method proposed by A.İlki are given in below.

$b = 200\,mm$

$h = 300\,mm$

$Wrap\ Layer\ No. = 1$

$t_{wrap} = 0.17\,mm$

$A_{frp} = 2\times(b+h)\times t_{wrap}\times w_{no} = 2\times(200+300)\times0.17\times1 = 170\,mm^2$

$A_{core} = 200\times300 = 60000\,mm^2$

$A_{core}^{confined} = (200-70)\times(300-70) = 29900\,mm^2\ (\textit{area is taken as outer unconfined area})$

$A_{core}^{unconfined} = 60000 - 29900 = 30100\,mm^2$

$$\rho_f = \frac{A_{frp}}{A_{uncore}} = \frac{170}{29900} = 0.004$$

$r_c = 33$

$$k_a = 1 - \left(\frac{(b-2\times r_c)^2 + (h-2\times r_c)^2}{3\times b\times h}\right) = 1 - \left(\frac{(200-2\times33)^2 + (300-2\times33)^2}{3\times200\times300}\right) = 0.596$$

$\varepsilon_{h,rup} = 0.85\times\varepsilon_{frp,ult} = 0.85\times0.018 = 0.015$

$E_{frp} = 245000\,MPa$

$$f_l' = \frac{k_a\times\rho_f\times\varepsilon_{h,rup}\times E_{frp}}{2} = \frac{0.596\times0.004\times0.015\times245000}{2} = 4.3434$$

$f_{co}' = 0.85\times f_{cd}^{unconf} = 42.5\,MPa$

$$\left[\frac{f_{cc}'}{f_{co}'}\right]_{CFRP} = \left[1 + 2.54\times\frac{f_l'}{f_{co}'}\right] = \left[1 + 2.54\times\frac{4.3434}{42.5}\right]$$

$f_{cc}' = 53.532$

$$\left[\frac{\varepsilon_{cc}}{\varepsilon_{co}}\right]_{CFRP} = \left[1 + \frac{h}{b}\times(LTF)\times19.27\times\left(\frac{f_l'}{f_{co}'}\right)^{0.53}\right]$$

$\varepsilon_{cc} = 0.00365$

Then cross-section of specimen X47-M-CFRP1 was modelled in XTRACT as given in Figure 6.5. Moment – curvature diagram for X47-M-CFRP1 was given in Figure 6.6.
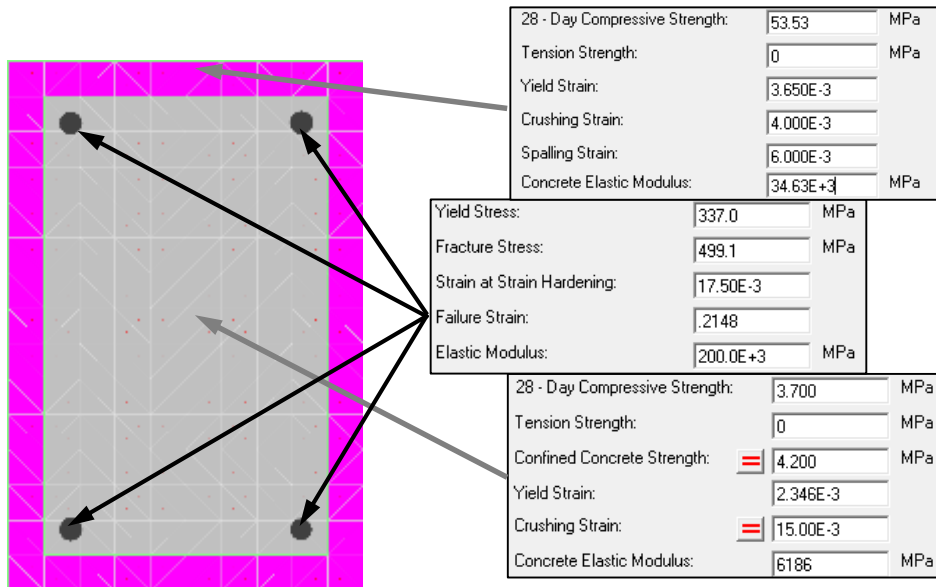
Figure 6.5 : Theorical section and material properties of X47-M-CFRP1 specimen.
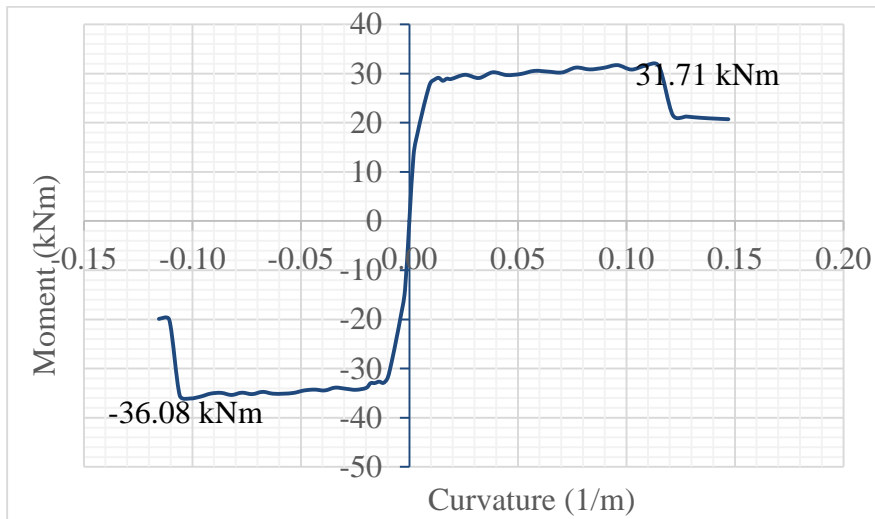

Figure 6.6 : Theoretical Moment – Curvature Diagram of X47-M-CFRP1 specimen.

For calculation of theorical moment capacity of X43-M-CFRP2, effect of confined concrete was calculated by using the method which proposed by Mander et al. and effect of unconfined and CFRP sheets together was calculated by using the method which proposed by A.İlki et al.. For X43-M-CFRP2, calculation steps of f'_{cc} and ε_{cc} according to method proposed by A.İlki are given in below.

$b = 200\,mm$

$h = 300\,mm$

$Wrap\,Layer\,No. = 2$

$t_{wrap} = 0.17\,mm$

$A_{frp} = 2 \times (b+h) \times t_{wrap} \times w_{no} = 2 \times (200+300) \times 0.17 \times 2 = 340\,mm^2$

$A_{core} = 200 \times 300 = 60000\,mm^2$

$$A_{core}^{confined} = (200 - 70) \times (300 - 70) = 29900 \, mm^2 \, (\text{area is taken as outer unconfined area})$$

$$A_{core}^{unconfined} = 60000 - 29900 = 30100 \, mm^2$$

$$\rho_f = \frac{A_{frp}}{A_{uncore}} = \frac{340}{29900} = 0.008$$

$$r_c = 33$$

$$k_a = 1 - \left(\frac{(b - 2 \times r_c)^2 + (h - 2 \times r_c)^2}{3 \times b \times h} \right) = 1 - \left(\frac{(200 - 2 \times 33)^2 + (300 - 2 \times 33)^2}{3 \times 200 \times 300} \right) = 0.596$$

$$\varepsilon_{h,rup} = 0.85 \times \varepsilon_{frp,ult} = 0.85 \times 0.018 = 0.015$$

$$E_{frp} = 245000 \, MPa$$

$$f_l^{'} = \frac{k_a \times \rho_f \times \varepsilon_{h,rup} \times E_{frp}}{2} = \frac{0.596 \times 0.004 \times 0.015 \times 245000}{2} = 8.6867$$

$$f_{co}^{'} = 0.85 \times f_{cd}^{unconf} = 42.5 \, MPa$$

$$\left[\frac{f_{cc}^{'}}{f_{co}^{'}} \right]_{CFRP} = \left[1 + 2.54 \times \frac{f_l^{'}}{f_{co}^{'}} \right] = \left[1 + 2.54 \times \frac{8.6867}{42.5} \right]$$

$$f_{cc}^{'} = 64.564$$

$$\left[\frac{\varepsilon_{cc}}{\varepsilon_{co}} \right]_{CFRP} = \left[1 + \frac{h}{b} \times (LTF) \times 19.27 \times \left(\frac{f_l^{'}}{f_{co}^{'}} \right)^{0.53} \right]$$

$$\varepsilon_{cc} = 0.00518$$

Then cross-section of specimen X43-M-CFRP2 was modelled in XTRACT as given in Figure 6.7. Moment − curvature diagram for X43-M-CFRP2 was given in Figure 6.8.
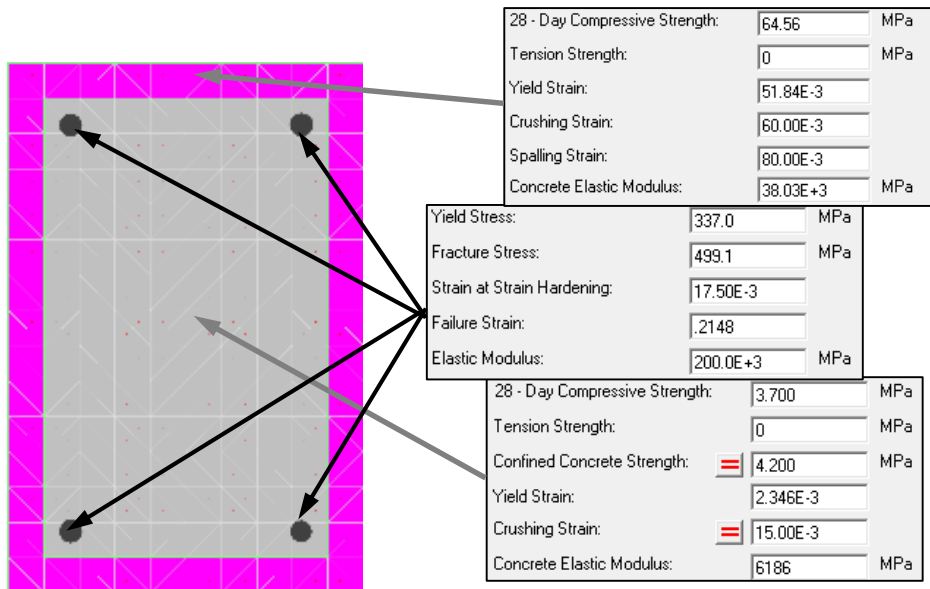
28 - Day Compressive Strength:	64.56	MPa
Tension Strength:	0	MPa
Yield Strain:	51.84E-3	
Crushing Strain:	60.00E-3	
Spalling Strain:	80.00E-3	
Concrete Elastic Modulus:	38.03E+3	MPa

Yield Stress:	337.0	MPa
Fracture Stress:	499.1	MPa
Strain at Strain Hardening:	17.50E-3	
Failure Strain:	.2148	
Elastic Modulus:	200.0E+3	MPa

28 - Day Compressive Strength:	3.700	MPa
Tension Strength:	0	MPa
Confined Concrete Strength:	= 4.200	MPa
Yield Strain:	2.346E-3	
Crushing Strain:	= 15.00E-3	
Concrete Elastic Modulus:	6186	MPa

Figure 6.7 : Theorical section and material properties of X47-M-CFRP2 specimen.
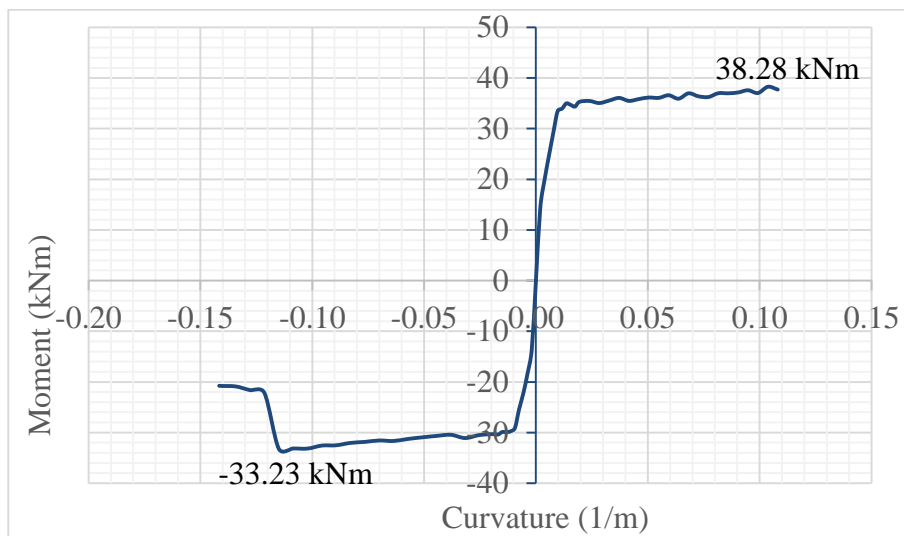
Figure 6.8 : Theoretical Moment − Curvature Diagram of X43-M-CFRP2 specimen.

For calculation of theorical moment capacity of X44-M-CFRP3, effect of confined concrete was calculated by using the method which proposed by Mander et al. and effect of unconfined and CFRP sheets together was calculated by using the method which proposed by A.İlki et al.. For X44-M-CFRP3, calculation steps of f'_{cc} and ε_{cc} according to method proposed by A.İlki are given in below.

$$b = 200\,mm$$
$$h = 300\,mm$$
$$Wrap\,Layer\,No. = 3$$
$$t_{wrap} = 0.17\,mm$$

$$A_{frp} = 2 \times (b+h) \times t_{wrap} \times w_{no} = 2 \times (200+300) \times 0.17 \times 3 = 510\,mm^2$$

$$A_{core} = 200 \times 300 = 60000 \, mm^2$$

$$A_{core}^{confined} = (200 - 70) \times (300 - 70) = 29900 \, mm^2 \ (area \ is \ taken \ as \ outer \ unconfined \ area)$$

$$A_{core}^{unconfined} = 60000 - 29900 = 30100 \, mm^2$$

$$\rho_f = \frac{A_{frp}}{A_{uncore}} = \frac{510}{29900} = 0.012$$

$$r_c = 33$$

$$k_a = 1 - \left(\frac{(b - 2 \times r_c)^2 + (h - 2 \times r_c)^2}{3 \times b \times h} \right) = 1 - \left(\frac{(200 - 2 \times 33)^2 + (300 - 2 \times 33)^2}{3 \times 200 \times 300} \right) = 0.596$$

$$\varepsilon_{h,rup} = 0.85 \times \varepsilon_{frp,ult} = 0.85 \times 0.018 = 0.015$$

$$E_{frp} = 245000 \, MPa$$

$$f_l' = \frac{k_a \times \rho_f \times \varepsilon_{h,rup} \times E_{frp}}{2} = \frac{0.596 \times 0.012 \times 0.015 \times 245000}{2} = 13.03$$

$$f_{co}' = 0.85 \times f_{cd}^{unconf} = 42.5 \, MPa$$

$$\left[\frac{f_{cc}'}{f_{co}'} \right]_{CFRP} = \left[1 + 2.54 \times \frac{f_l'}{f_{co}'} \right] = \left[1 + 2.54 \times \frac{13.03}{42.5} \right]$$

$$f_{cc}' = 75.59$$

$$\left[\frac{\varepsilon_{cc}}{\varepsilon_{co}} \right]_{CFRP} = \left[1 + \frac{h}{b} \times (LTF) \times 19.27 \times \left(\frac{f_l'}{f_{co}'} \right)^{0.53} \right]$$

$$\varepsilon_{cc} = 0.00638$$

Then cross-section of specimen X44-M-CFRP3 was modelled in XTRACT as given in Figure 6.9. Moment – curvature diagram for X44-M-CFRP3 was given in Figure 6.10.
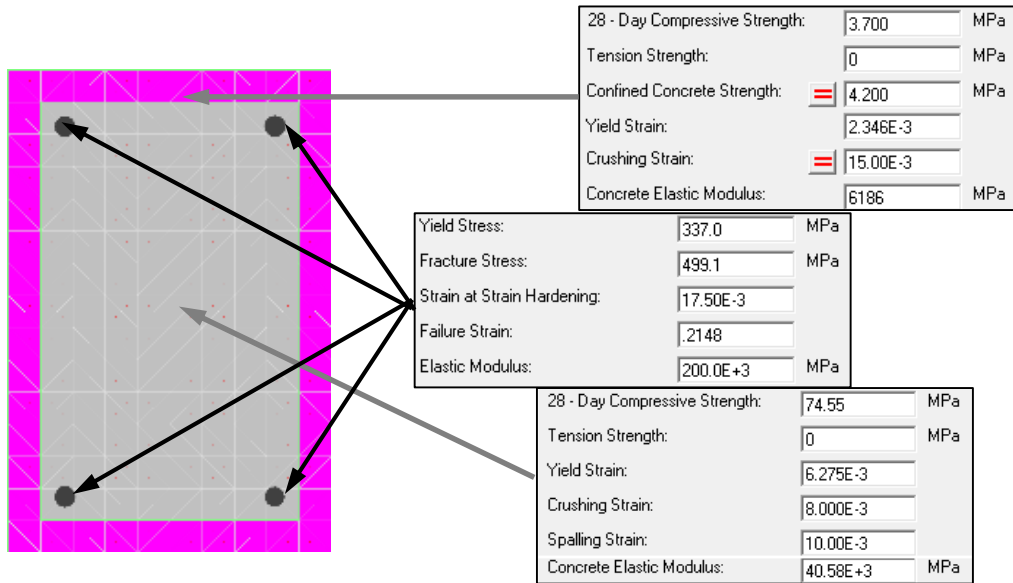
Figure 6.9 : Theorical section and material properties of X44-M-CFRP3 specimen.
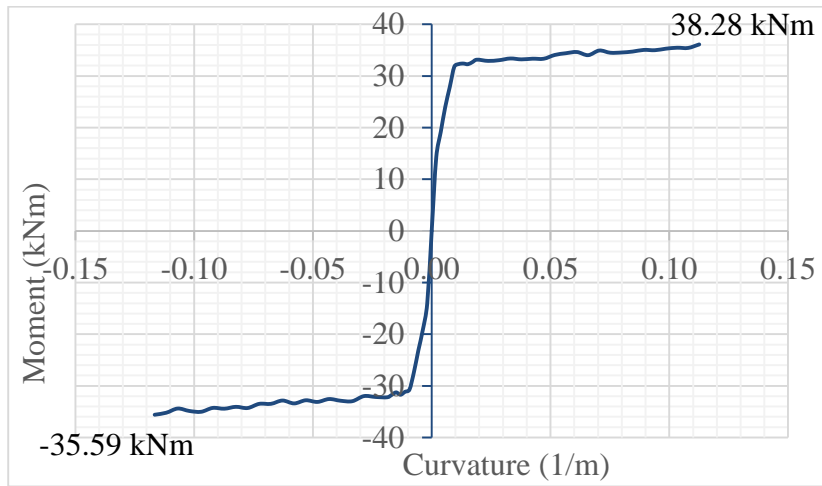
Figure 6.10 : Theoretical Moment – Curvature Diagram of X44-M-CFRP3 specimen.

Comparison of theoretical and experimental capacities of the specimens are given in Table 6.1.

Table 6.1 : Theoretical and experimental capacities of the specimens.

Specimen Name	Theoretical P (+) (kN)	Theoretical P (-) (kN)	Experimental P(+) (kN)	Experimental P(-) (kN)	Standart Deviation (kN)
X0-REF1					
X26-REF2	22.89	-22.81	26.71	-24.96	12%
X26-M	32.70	-31.64	31.23	-28.67	3%
X47-M-CFRP1	26.43	-30.07	25.62	-32.55	2%
X43-M-CFRP2	31.90	-27.69	33.21	-27.82	3%
X44-M-CFRP3	30.08	-29.66	30.18	-28.63	0%

7. TEST RESULTS

7.1 X0-REF1

Results of X0-REF1 specimen are taken from PhD. Thesis of Dr. Çağlar GÖKSU which had done before this thesis to compare with corroded specimen test results. X0-REF1 is the reference specimen which was not exposed to any accelerated corrosion process or rehabilitation application. Test was examined at 1.6.2007 within the doctoral studies of Dr. Çağlar GÖKSU (Goksu, 2012). Axial load of the specimen was 124 kN, and test was performed displacement-controlled like as done in this thesis.

No cracks were observed while loading to target displacements of ±1.2 mm (drift ratio 0.10%) and ±3 mm (drift ratio 0.25%). First flexural crack was observed at the interface of the column and footing during loading to target displacement of 6 mm (drift ratio 0.5%). The view of the specimen X0-REF1 after 0.50% drift ratio is shown in Figure 7.1.
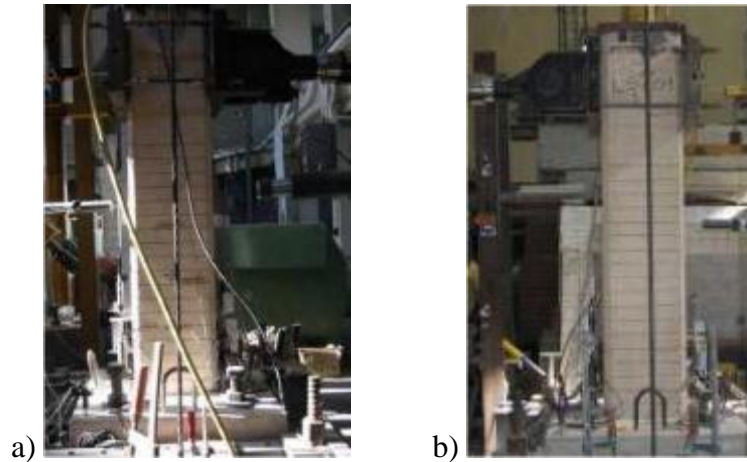
Figure 7.1 : a) North, and b) South view of the X0-REF1 specimen after -0.50% drift ratio. (Goksu, 2012)

Second flexural crack was observed 250 mm above the footing during loading to target displacement of 12 mm(drift ratio 1.00%). The view of the specimen X0-REF1 after -1.50% drift ratio is shown in Figure 7.2.
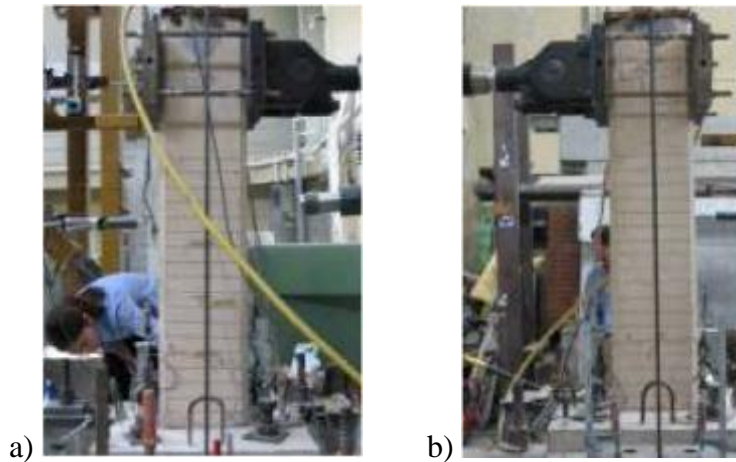
Figure 7.2 : a) North, and b) South view of the X0-REF1 specimen after -1.50% drift ratio (Goksu, 2012).

During loading to target displacement of 24 mm (drift ratio 2.00%), vertical cracks formed at the lap splice zone. Similar type of damages occurred at the opposite side while the column was subjected to pulling. The view of the specimen X0-REF1 after -2.50% drift ratio is shown in Figure 7.3.

Figure 7.3 : a) North, and b) South view of the LS-C0 specimen after -3.50% drift ratio (Goksu, 2012).

As the testing progressed, cracks generally accumulated 300 mm above the footing. The view of the specimen X0-REF1 specimen after -5.00% drift ratio is shown in Figure 7.4. Force-displacement relationship of the specimen X0-REF1 is presented in Figure 7.5. In this figure, *P* is applied lateral load and *P0* is the theoretical lateral load capacity of the specimen determined without considering the effect of corrosion. First flexural crack, first shear crack, first vertical crack, crushing of concrete cover, spalling of concrete cover, maximum strain on the starter bar and maximum strain on the longitudinal bar are marked on the figure. As seen from **Figure 7.5**, no strength loss

was observed. The decline is due to the horizontal component of the axial load. As the line of action of the axial load does not pass through the column base during the tests of all column specimens, to account P-o effects, the effect of axial load resolved to its horizontal and vertical components. Then, the horizontal components of the axial load subtracted from the force applied by the actuator and the net horizontal force obtained. This correction was done due to PEER (2004) Case 4.
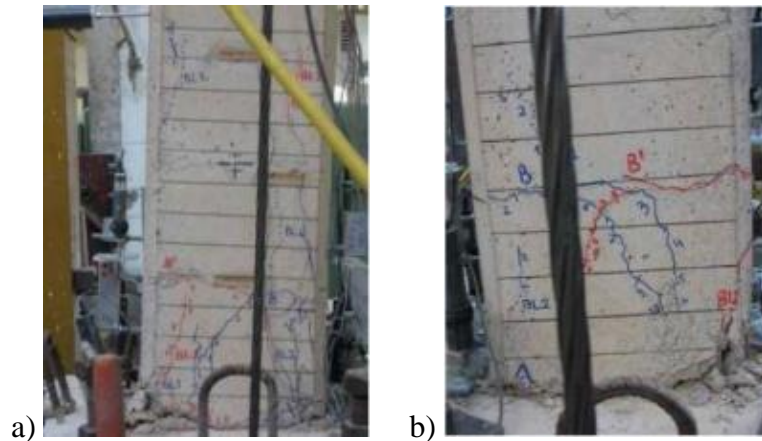
Figure 7.4 : a) North, and b) South view of the X0-REF1 specimen after -5.00% drift ratio (Goksu, 2012).

Summary of the seismic behavior of specimen X0-REF1 is shown in Table 7.1.
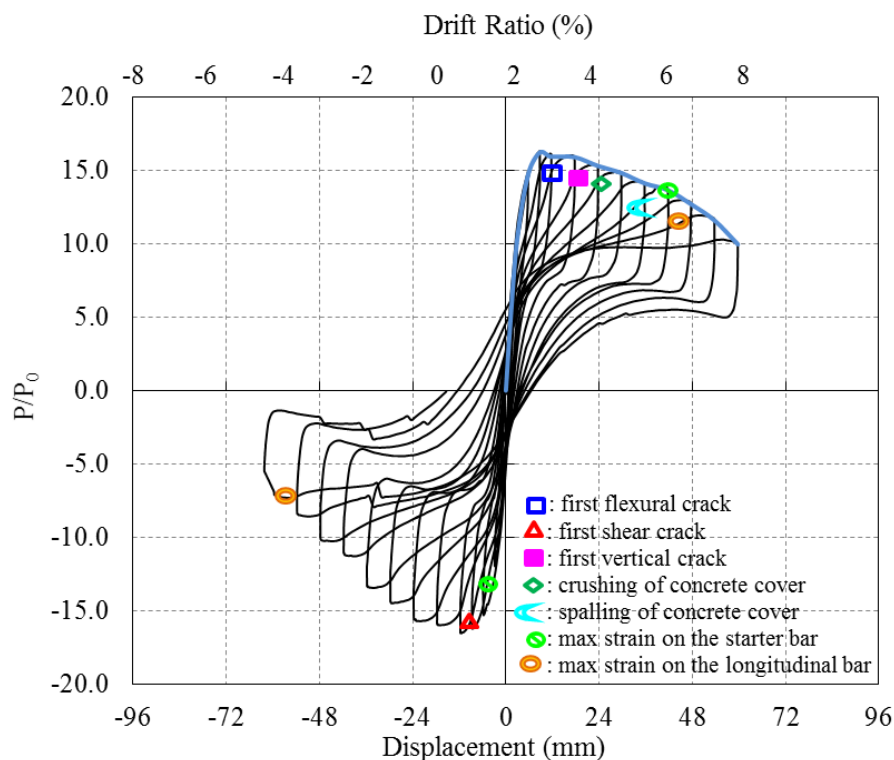
Figure 7.5 : Lateral load/Theoretical load capacity capacity versus displacement for X0-REF1 (Goksu, 2012).

For the observation of distribution of damages, moment-curvature relationships were obtained at different gauge lengths at the potential plastic hinge zones (Figure 7.6).

Table 7.1 : Summary of the seismic behavior of X0-REF1(Goksu, 2012).

Drift Ratio (%)	δ (mm/mm)	P (kN)	Observations
0.1	±1.2	4.67/-6.74	No crack was observed.
2.5	±3	10.3/-11.91	No crack was observed.
0.5	±6	14.7/-15.23	First flexural crack at column-footing interface was observed
0.75	±9	16.2/-16.17	
1	±12	15.9/-16.48	Flexural shear cracks were observed.
1.5	±18	15.9/-15.86	
2	±24	15.3/-15.46	Vertical cracks, indicating slip, formed at the interface of the column and footing and lap splice zone durin pulling and pushing cycles
2.5	±30	14.8/-14.36	Crushing started at the interface of the column and footing at the compression zone
3	±36	14.1/-13.31	
3.5	±42	13.6/-11.03	Concrete cover spalled at the north side of the column at the compressive zone. Concrete crushed at the south side of the column
4	±48	12.7/-10	
4.5	±54	11.6/-8.32	
5	±60	9.95/-6.82	Specimen underwent excessive deformation out of its axis and test was ended by decreasing axial load.
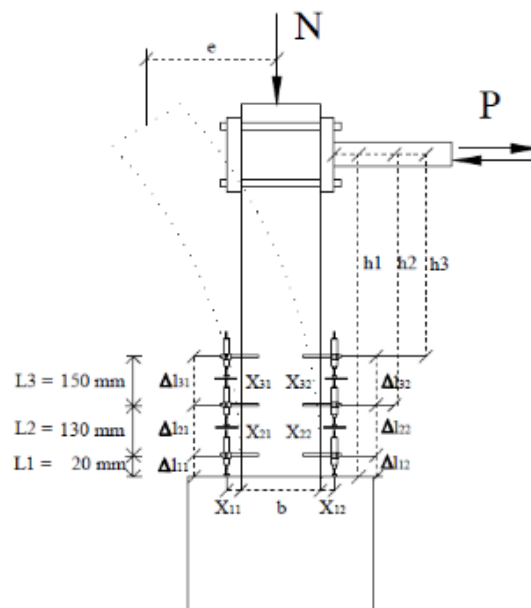
Figure 7.6 : Test setup with measurement system used in obtaining moment-curvature relationship (Goksu, 2012).

The calculation of the moment-curvature relationships are performed assuming that plane sections remain plain. Moment is calculated by using Eq. (7.1) taking into account the second-order effects. In the equation, P is the lateral load, H is the column height, N is the axial load, and e is the eccentricity due to horizontal displacement of the column, subjected to lateral load, P.

$$M = P.H + N.e \tag{7.1}$$

For the calculation of moment-curvature relationships, the average curvature values were obtained in 20 mm, 150 mm and 300 mm above the footing. Curvatures were calculated by dividing the obtained strains from the LVDTs to the distance between the LVDTs (Eq. (7.2)).

$$x = \frac{(\varepsilon_1 + \varepsilon_2)}{b + X_{11} + X_{12}} \tag{7.2}$$

Average experimental moment-curvature relationships obtained for critical sections of the specimen X0-REF1 are presented in Figure 7. For the calculation of moment-curvature relationships, the average curvature values obtained for the ranges of 0-20 mm, 20-150 mm and 150-300 mm heights above the footing were taken into account. As seen from Figure 7.7, the curvature values of the member measured in 20-150 mm and 150-300 mm height above the support are in the order of 5.10^{-5} (1/ mm), while the curvatures measured in 0-20 mm height are in the order of 3.10^{-3} (1/ mm). According to Figure 6.12, it is of interest to note that the damage is accumulated especially in 20 mm height of the member from top of the base.

a)

41
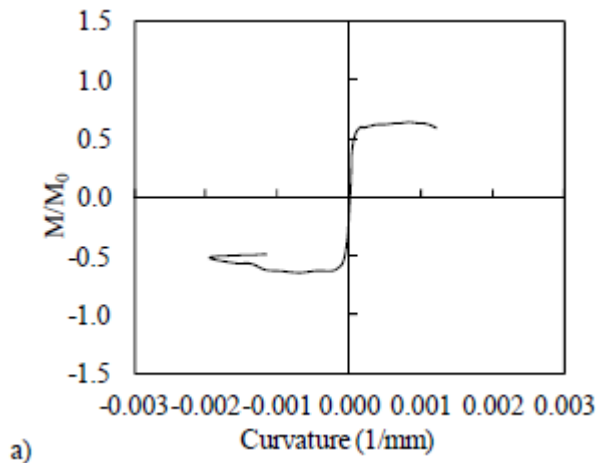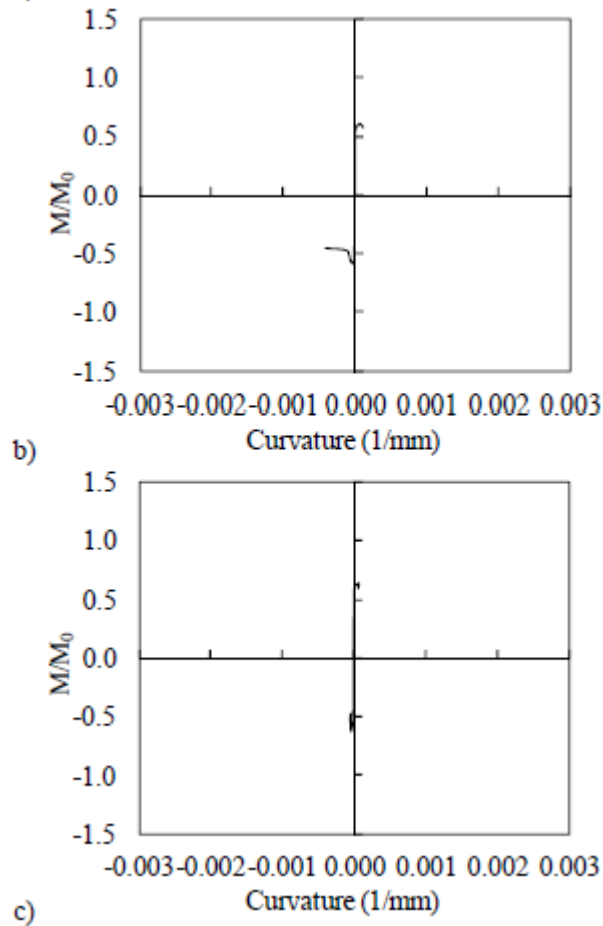
Figure 7.7 : Moment-curvature relationships obtained for a) 0-20 mm, b) 20-150 mm, c) 150-300 mm gauge lengths (Goksu, 2012).

According to the data from the straingauges on the starter bars of the X0-REF1, the maximum strain while pushing was 0.0008, measured from the straingauge at +200 mm above the footing for P=13.63 kN at 0.035 drift ratio; the maximum strain while pulling was -0.0004, measured from the straingauge at +100 mm above the footing when P=-11.91 kN at -0.0025 drift ratio. According to the data from the straingauges on the longitudinal bars of the X0-REF1, the maximum strain while pushing was 0.0003, measured from the straingauge at +400 mm above the footing when P=12.67 kN at 0.04 drift ratio; the maximum strain while pulling was -0.0008, measured from the straingauge at +200 mm above the footing when P=-6.82 kN at -0.05 drift ratio. Strain distribution of the starter bars and longitudinal bars of X0-REF1 while pushing and pulling are shown in Figure 7.8 and Figure 7.9, respectively. As seen from Figure 7.8 and Figure 7.9, the strain values did not reach yield strain.

42
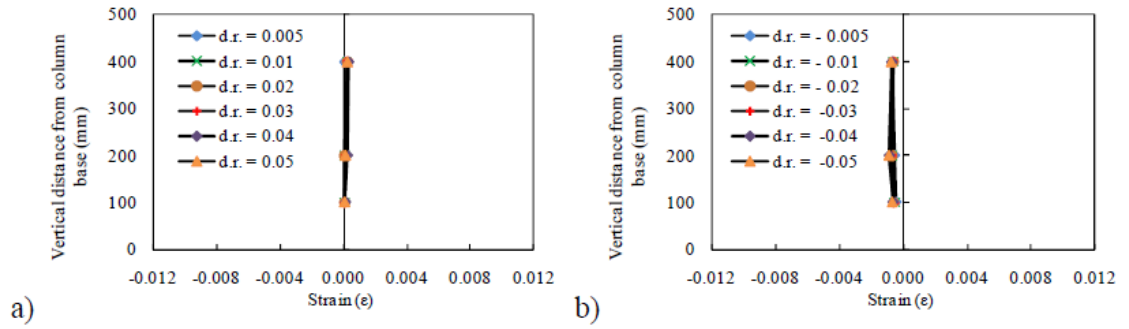
Figure 7.8 : Strain distribution of the starter bars of X0-REF1 a) while pushing, b) while pulling (Goksu, 2012).
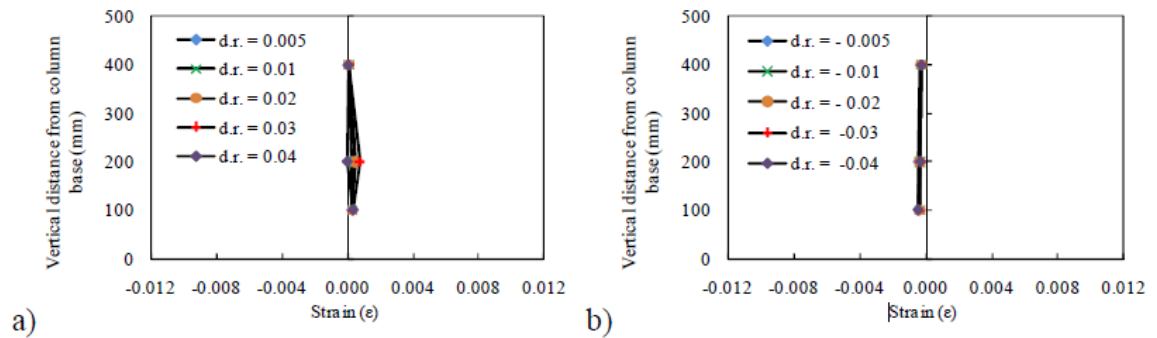
Figure 7.9 : Strain distribution of the longitudinal bars of X0-REF1 a) while pushing b) while pulling (Goksu, 2012).

7.2 X26-REF2

X26-REF2 was the reference specimen which was exposed to accelerated corrosion process and there was no rehabilitation/retrofitting application. Test was examined at 26.7.2011. Axial load of the specimen was 124 kN, and test was performed displacement-controlled.

No cracks were observed while loading to target displacements of ±3 mm (0.25% drift ratio), after ±3 mm (0.25% drift ratio) target displacement, some vertical cracks were observed. First flexural cracks was observed at both sides of the specimen (A-north, A-south) with 0.1 mm width during loading to target displacement ±6 mm (0.50% drift ratio). The view of the specimen X26-REF2 after -0.50% drift ratio is shown in Figure 7.10.
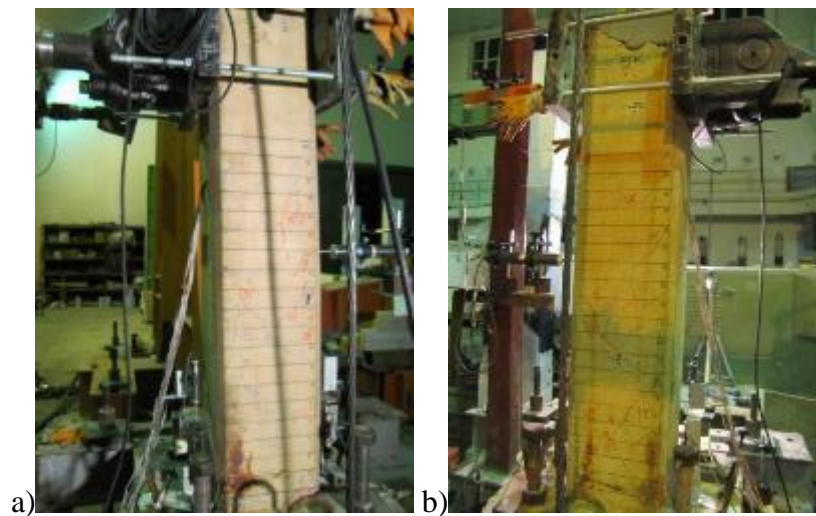
a)   b)
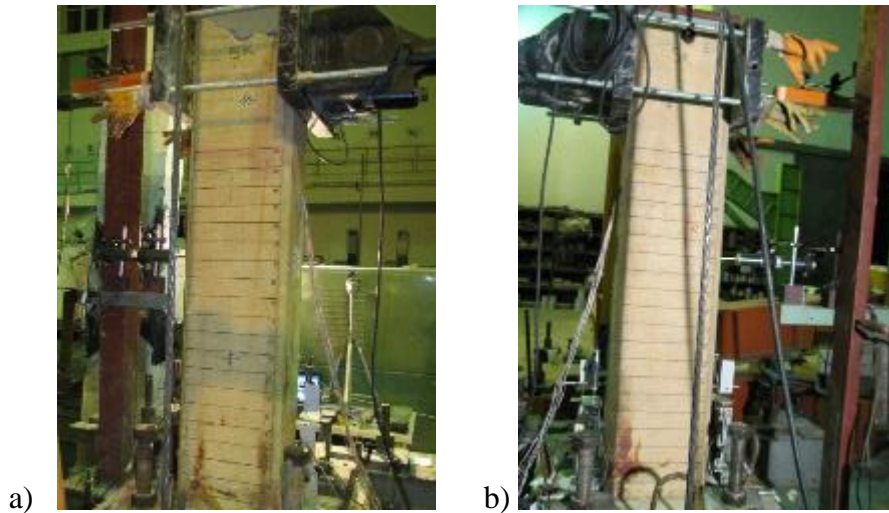
Figure 7.10 : a) North, and b) South view of the X26-REF2 specimen after target displacement ±6 mm (-0.50% drift ratio).

During loading to target displacement -9 mm (drift ratio -0.75%) second flexural crack was observed at interface of the column and footing. The view of the specimen X26-REF2 after target displacement -9 mm (drift ratio -0.75%) is shown in Figure 7.11.

a)   b)
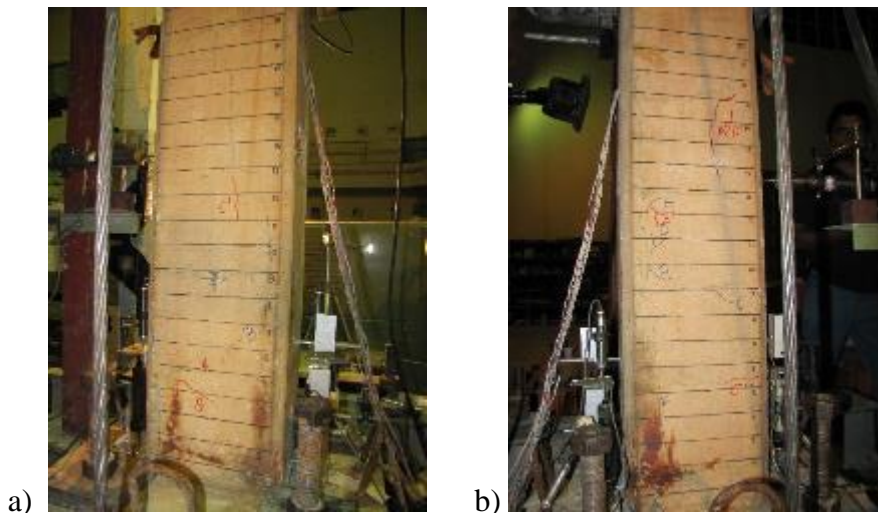
Figure 7.11 : a) North, and b) South view of the X26-REF2 specimen after target displacement -9 mm (-0.75% drift ratio).

Some cracks were occurred after acceleration corrosion process along the column transverse and longitidunal bars. These cracks was marked with green marker on the pictures. During loading to target displacement -12 mm (-1% drift ratio), size increasing of these cracks and propagation of existing cracks were observed. X26-REF2 after target displacement -12 mm (drift ratio -1%) is given in Figure 7.12.
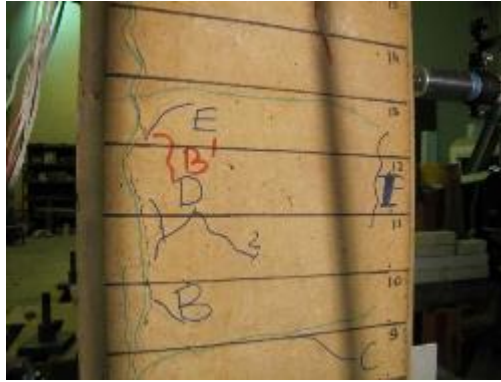
Figure 7.12 : Cracks because of transverse and longitudinal bars after target displacement -12 mm (-1% drift ratio).

During loading to target displacement of -18 mm (drift ratio -1.50%) flexural cracks (K-south, L-south, M-south, F-north, G-north, H-north, I-north, J-north, K-north, H'-south, I'-south, J'-south, K'-north), vertical cracks (N-south, O-south) and propagation of existing cracks (A-north, B-north, E-north, A-south, B-south, B'-south, E'-south, A'- north, D'-north, E'-north, H'-north, J'-north) were observed. X26-REF2 after target displacement -18 mm (drift ratio -1.5%) is given in Figure 7.13.

a)   b)

Figure 7.13 : a) North, and b) South view of X26-REF2 after target displacement -18 mm (-1.50 % mm drift ratio).

During loading to target displacement of -24 mm (drift ratio -2.00%) flexural cracks (K'-south(0.1 mm), P-south(0.1 mm), R-south(0.3 mm)), shear cracks (L-north(0.7 mm), M-north(0.1 mm), N-north(0.4 mm), vertical cracks (N-south, O-south) and propagation of existing cracks (A-north(0.3 mm to 0.6 mm), B-north(0.2 mm to 0.5 mm), C-north(0.1 mm to 0.3 mm), D-north(0.1 mm to 0.2 mm), A-south(0.7 mm to

0.8 mm), I-south(0.1 mm to 0.2 mm), M-south(0.1 mm to 0.2 mm), O-south(0.1 mm to 0.3 mm), I'north(0.1 mm to 0.2 mm), K'north(0.3 mm to 0.4 mm), I'south(0.4 mm to 0.5 mm), E'-south(1.4 mm to 2.1 mm), A'-south(0.1 mm to 0.2 mm), B'-south(0.2 mm to 1.2 mm)) were observed. X26-REF2 after target displacement -24 mm (drift ratio -2%) is given in Figure 7.14.

a)   b)
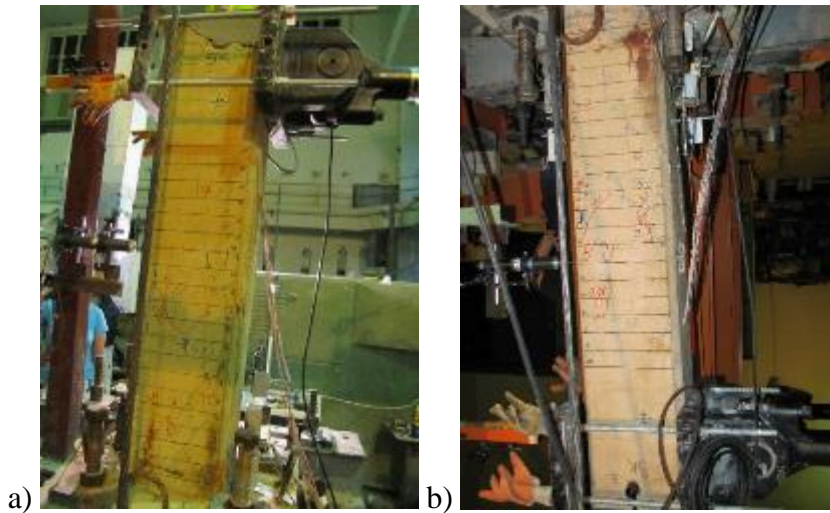
Figure 7.14 : a) North, and b) South view of X26-REF2 after -2.00 % mm drift ratio.

During loading to target displacement of -30 mm (drift ratio -2.50%) flexural cracks (O-north(0.2 mm), P-north(0.1 mm)), shear cracks (L'-south(0.2 mm)), vertical cracks (S-south(0.2 mm)), crushing on cracks (D'-north, B'-south, D'-south, E'-south, I'-south) and propagation of existing cracks (B-north(0.5 mm to 0.6 mm), G-north(0.1 mm to 0.2 mm), H-north(0.2 mm to 0.3 mm), J-north(0.2 mm to 0.3 mm), K-north(0.7 mm to 0.8 mm), L-north(0.7 mm to 5 mm), M-north(0.1 mm to 0.5 mm), N-north(0.4 mm to 2.3 mm), A-south(0.8 mm to 1.1 mm), B-south(0.1 mm to 5.5 mm), D-south(0.1 mm to 0.3 mm), E-south(0.1 mm to 0.4 mm), I-south(0.2 mm to 9 mm), K-south(0.1 mm to 0.3 mm), M-south(0.2 mm to 0.8 mm), O-south(0.3 mm to 5 mm), G'north(0.1 mm to 0.5 mm), F'south(0.1 mm to 0.6 mm), J'-south(0.1 mm to 0.3 mm)) were observed. X26-REF2 after target displacement -30 mm (drift ratio -2.5%) is given in Figure 7.15.
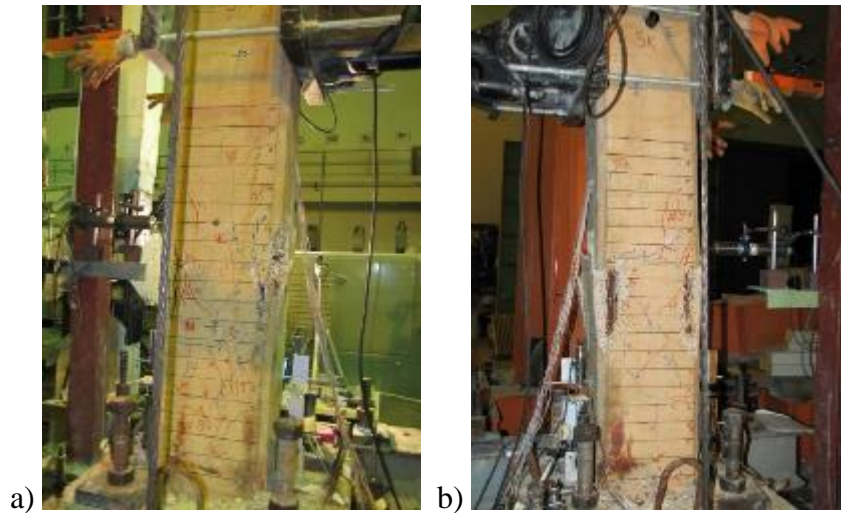
Figure 7.15 : a) North, and b) South view of X26-REF2 after -2.50 % mm drift ratio.

During loading to target displacement of -36 mm (drift ratio -3.00%), longitudinal bars of the specimen were buckled due to excessive axial load. North, and south view of X26-REF2 after experiment end was given in Figure 7.16.
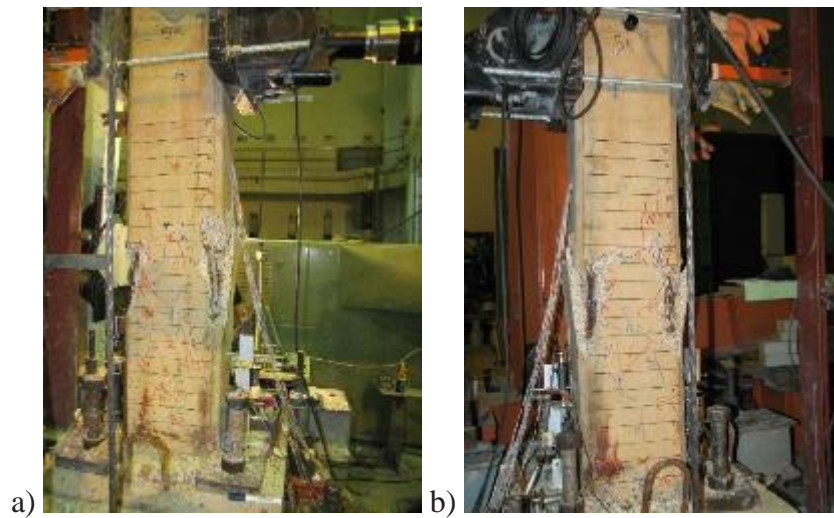
Figure 7.16 : a) North, and b) South view of X26-REF2 after experiment finished.

Summary of the seismic behavior of specimen X26-REF2 is shown in Table 7.2.

Table 7.2 : Summary of the seismic behavior of X26-REF2.

Drift Ratio (%)	δ (mm/mm)	P (kN)	Observations
0.1	±1.2	5.70/-5.20	No crack was observed.
2.5	±3	12.20/-10.80	Some little vertical cracks observed.
0.5	±6	18.9/-15.7	Small diagonal crack at South side
0.75	±9	23.0/-20.5	Flexural shear cracks were observed.
1	±12	24.9/-24.2	
1.5	±18	26.5/-27.10	
2	±24	27.70/-24.40	Vertical cracks, shear cracks formed at the interface of the column and footing and lap splice zone during pulling and pushing cycles
2.5	±30	22.2/-17.0	Buckling of longitidunal bars started. Concrete cover crushed.
3	±36	10.1/-13.31	Test ended.

Force-displacement relationship of X26-REF2 is presented in Figure 7.17. In this figure, P is applied lateral load and P_0 is the theoretical lateral load capacity of the specimen determined without considering the effect of corrosion. First flexural crack, first shear crack, first vertical crack, yielding of starter bar, crushing of concrete cover, spalling of concrete cover, fracture of starter bar, maximum strain on the starter bar and maximum strain on the longitudinal bar are marked on the figure. As seen from Figure 7.17, strength loss was observed.
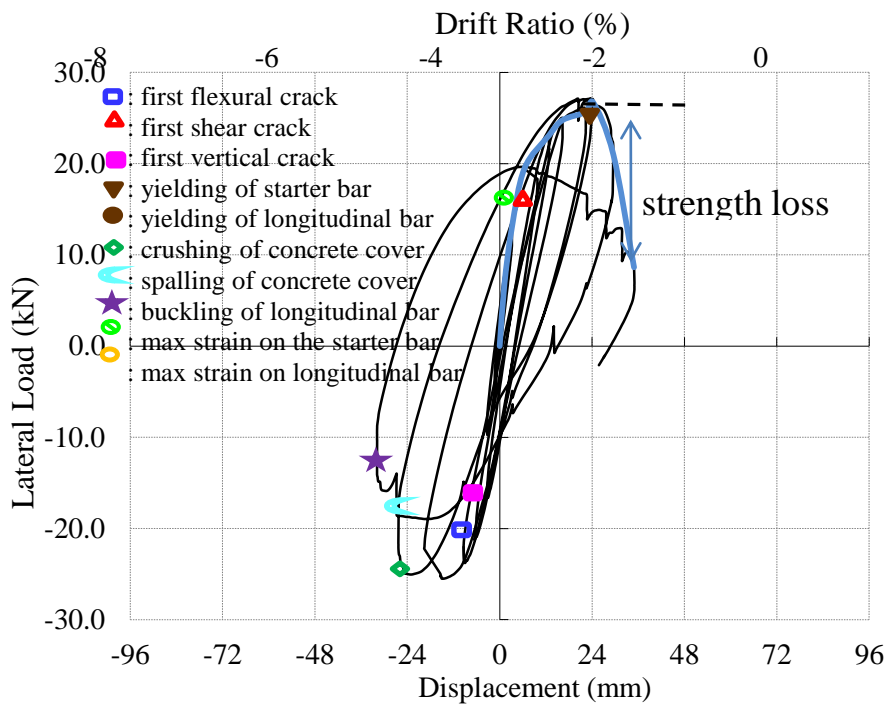
Figure 7.17 : Lateral load versus displacement for X26-REF2.

Average experimental moment-curvature relationships obtained for critical sections of X26-REF2 are presented in Figure 7.18. For the calculation of moment-curvature relationships, the average curvature values which were obtained for the ranges of 0-20 mm, 20-150 mm and 150-300 mm heights above the footing were taken into account. As seen from Figure 7.18, the curvature values of the member measured in 20-150 mm and 150-300 mm height above the support are in the order of 5.10-5 (1/ mm), while the curvatures measured in 0-20 mm height are in the order of 3.10-3 (1/ mm). According to Figure 7.18, it is of interest to note that the damage is accumulated especially in 20 mm height of the member from top of the base according to the moment-curvature relationships.

a)

b)

c)
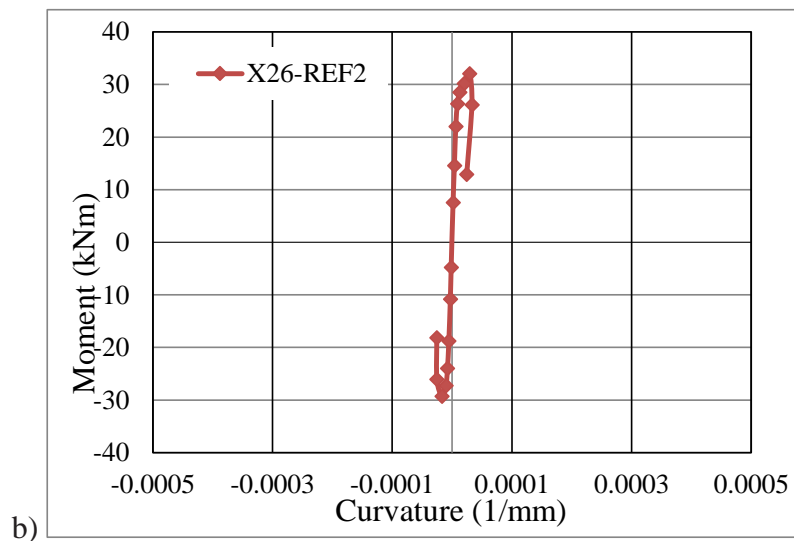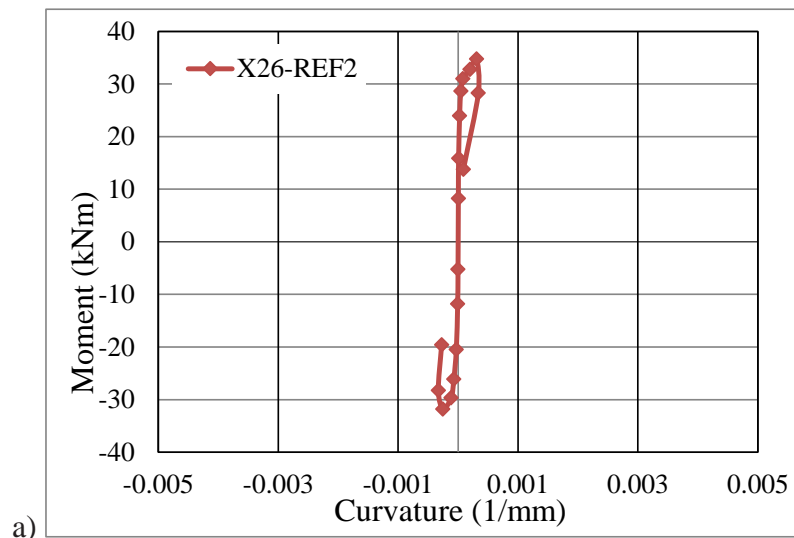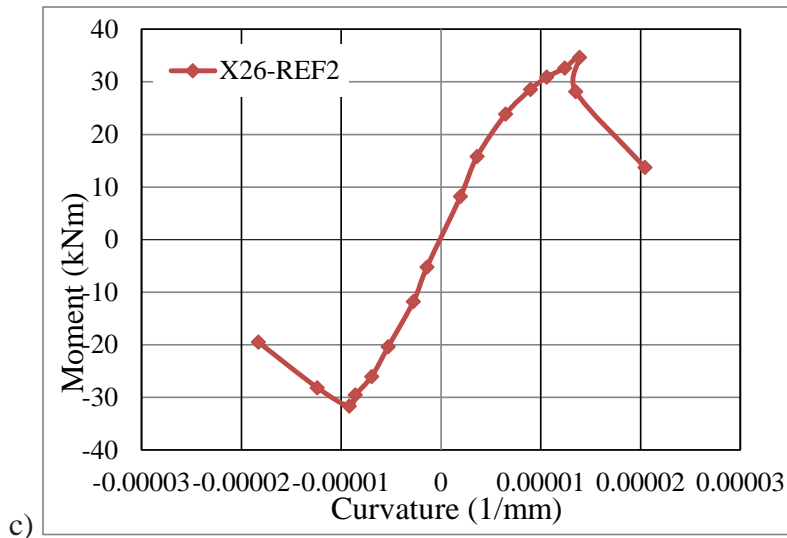
Figure 7.18 : Moment-curvature relationships obtained for a) 20 mm, b) 150 mm, c) 300 mm gauge lengths.

According to the data from the straingauges on the starter bars, the maximum strain while pushing was 0.00184, measured from the straingauge at +100 mm above the footing when P=28.5 kN at 0.02 drift ratio; the maximum strain while pulling was -0.00158, measured from the straingauge at +100 mm above the footing when P=-15.54 kN at -0.02 drift ratio; the maximum strain while pushing was 0.00235, measured from the straingauge at +200 mm above the footing when P=20.08 kN at 0.03 drift ratio; the maximum strain while pulling was -0.00129, measured from the straingauge at +200 mm above the footing when P=-0.77 kN at -0.025 drift ratio. According to the data from the straingauges on the longitudinal bars of the X26-REF2, the maximum strain while pushing was 0.0005, measured from the straingauge at +100 mm above the footing when P=12.69 kN at 0.03 drift ratio; the maximum strain while pulling was -0.00116, measured from the straingauge at +100 mm above the footing when P=-26.95 kN at -0.02 drift ratio. Strain distribution of the starter bars and longitudinal bars of X26-REF2 while pushing and pulling are shown in Figure 7.19 and Figure 7.20. As seen from Figure 7.19 and Figure 7.20, the strain values of starter bars reach yield strain while pushing.
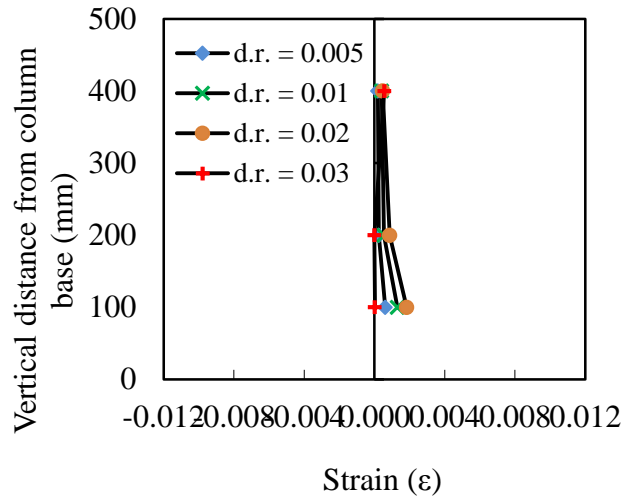
a)
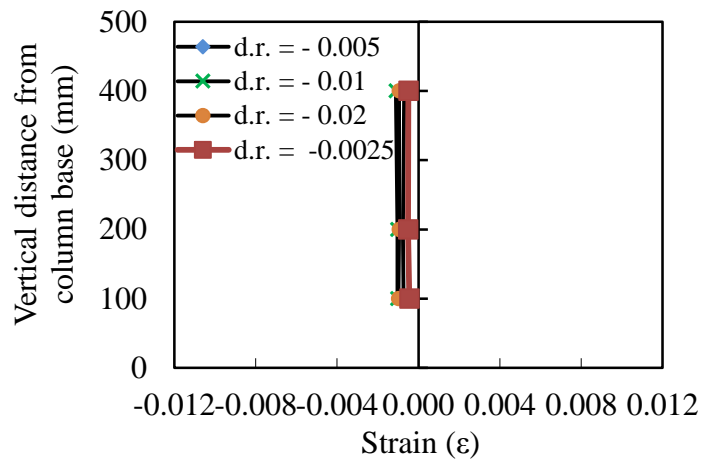
b)

Figure 7.19 : Strain distribution of the starter bars of X26-REF2 a) while pushing, b) while pulling.
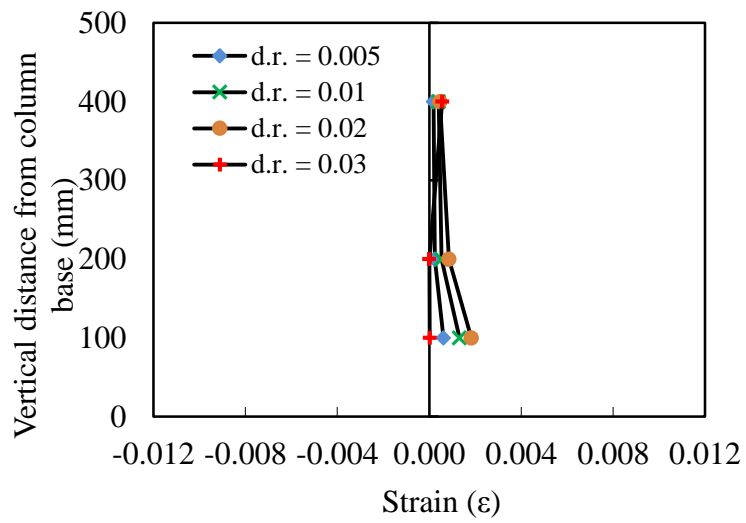
a)
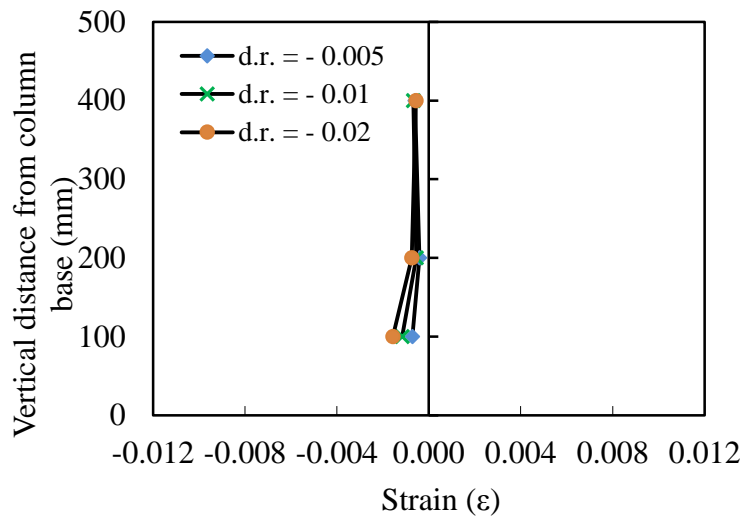
b)

Figure 7.20 : Strain distribution of the longitudinal bars of X26-REF2 a) while pushing, b) while pulling.

7.3 X26-M

X26-M is the rehabilitated specimen which was rehabilitated after exposed to accelerated corrosion process. Test was examined at 6.2.2012. Axial load of the specimen was 124 kN, and test was performed displacement-controlled. After rehabilitation process some vertical and horizontal shrinkage cracks were occurred on the surface of the specimen.These cracks marked with green marker on the concrete surface. The view of the specimen X26-M before the starting of test was shown in Figure 7.21.

Figure 7.21 : The view of the specimen X26-M before the starting of test

No cracks were observed while loading to target displacements of ±3 mm (0.25% drift ratio), at target displacement -3 mm (-0.25% drift ratio), first flexural cracks (A'-south, 0.15 mm) was observed. First cracks at interface of the column and footing was observed while during loading to target displacement 6 mm (0.5% drift ratio).

During the loading cycle for target displacement ±9 mm (drift ratio ±0.75%) vertical cracks (A-north, 0.3 mm, B'-south, 0.5 mm) observed on concrete surface of longitudinal bars and second flexural crack(B-north, 0.1 mm, C'-south, 0.9 mm) was observed at interface of the column and footing. The view of the specimen X26-M after target displacement -9 mm (drift ratio -0.75%) is shown in Figure 7.22.
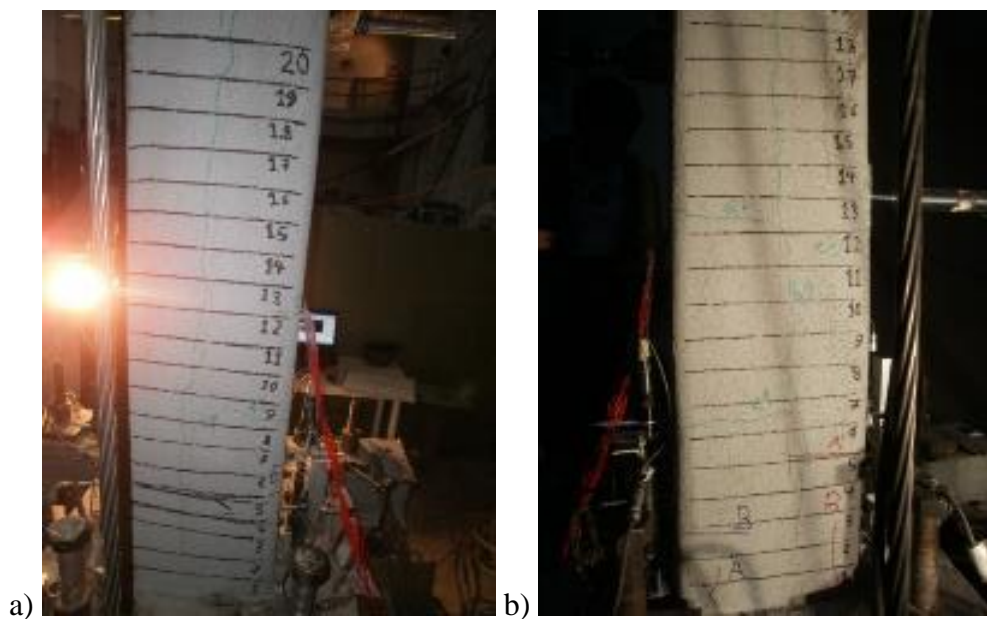
Figure 7.22 : a) North, and b) South view of X26-M after -0.75 % mm drift ratio.

During the loading cycle for target displacement ±12 mm (drift ratio ±1%) vertical cracks (A'-north (0.05 mm), A-south (0.3 mm), B-south(0.05 mm)) and propagation of existing cracks (A-north (0.3 mm to 0.7 mm), B-north(0.1 mm to 0.15 mm), A'-south (0.1 mm to 0.05 mm), B'-south (0.5 mm to 0.85 mm), C'-south (0.9 mm to 0.7 mm)) was observed. The view of the specimen X26-M after target displacement -12 mm (drift ratio -1%) is shown in Figure 7.23.
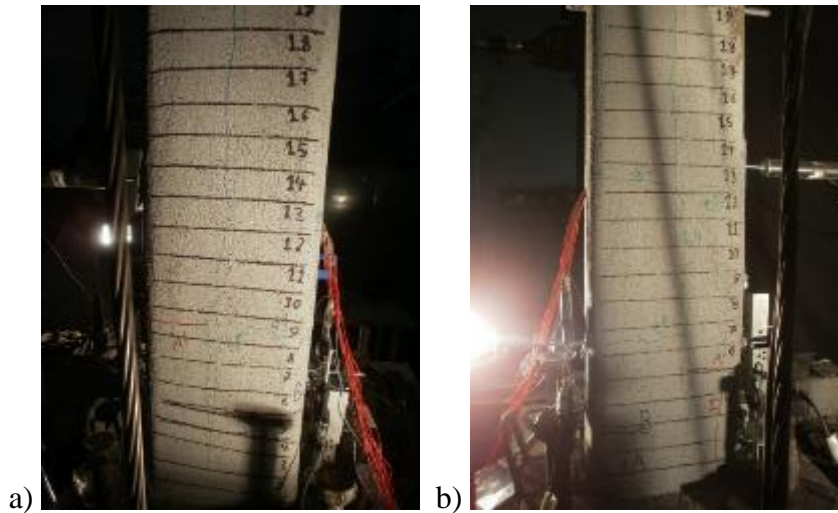
Figure 7.23 : a) North, and b) South view of X26-M after -1.00 % mm drift ratio.

During the loading cycle for target displacement ±18 mm (drift ratio ±1.5%) any new cracks was not occurred on concrete surface and propagation of existing cracks A-north (0.7 mm to 2.7 mm), A-south (0.3 mm to 0.2 mm), A'-north (0.05 mm to 0.1 mm), B'-south (0.85 mm to 1.50 mm), C'-south (0.7 mm to 0.6 mm)) was observed. The view of the specimen X26-M after target displacement -12 mm (drift ratio -1.5%) is shown in Figure 7.24.
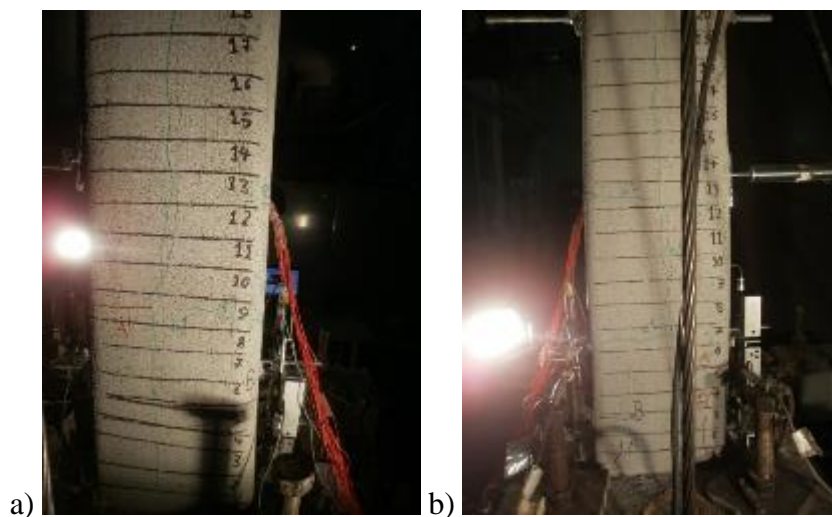
Figure 7.24 : a) North, and b) South view of X26-M after -1.50 % mm drift ratio.

During the loading cycle for target displacement ±24 mm (drift ratio ±2%),first shear cracks C-south (0.6 mm), vertical cracks B'-north (0.25 mm), D'-south (0.9 mm), E'-south (0.2 mm), crushing on concrete surface crack (C'-south) and propagation of

existing cracks A-north (2.7 mm to 6 mm), B-north (0.15 mm to 0.05 mm), A-south (0.2 mm to 0.7 mm), B-south (0.05 mm to 0.1 mm), A'-north (0.1 mm to 0.2 mm), B'-south (1.50 mm to 1.60 mm)) was observed. The view of the specimen X26-M after target displacement -12 mm (drift ratio -2%) is shown in Figure 7.25.

a)   b)
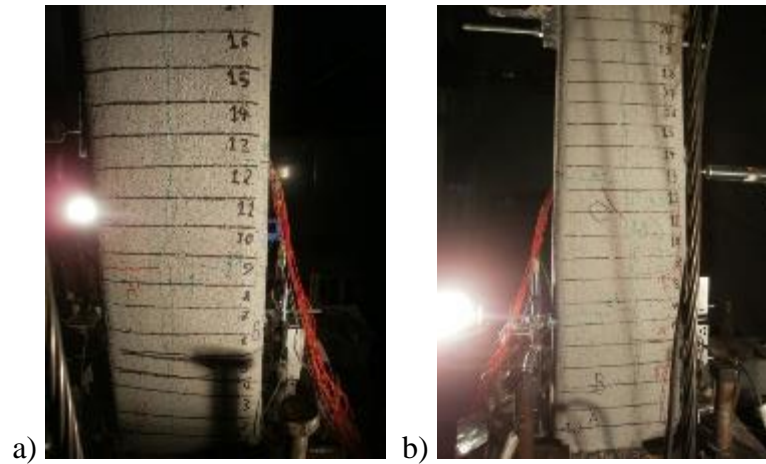
Figure 7.25 : a) North, and b) South view of X26-M after -2.00 % mm drift ratio.

During the loading cycle for target displacement ±48 mm (drift ratio ±4%), propagation of existing cracks A-north (13 mm), B-north (0.4 mm), C-north (0.5 mm), A-south (5.4 mm), B-south(0.5 mm), C-south(0.35 mm), B'-north (1.50 mm) , A'-south (0.1 mm), B'-south (1.6 mm), C'-south (13 mm), D'-south (1.4 mm), E'-south (0.1 mm) was observed. The view of the specimen X26-M after target displacement -12 mm (drift ratio -4%) is shown in Figure 7.26.

a)   b)

Figure 7.26 : a) North, and b) South view of X26-M after -4.00 % mm drift ratio.

After target displacement ±54 mm some cracks on the concrete surface was started to crushing and spalling, it contunied until target displacement -84 mm, after target

displacement ±84 mm test was ended due to fallen load capacity. The view of the specimen X26-M after test ended is shown in Figure 7.27.

a)   b)
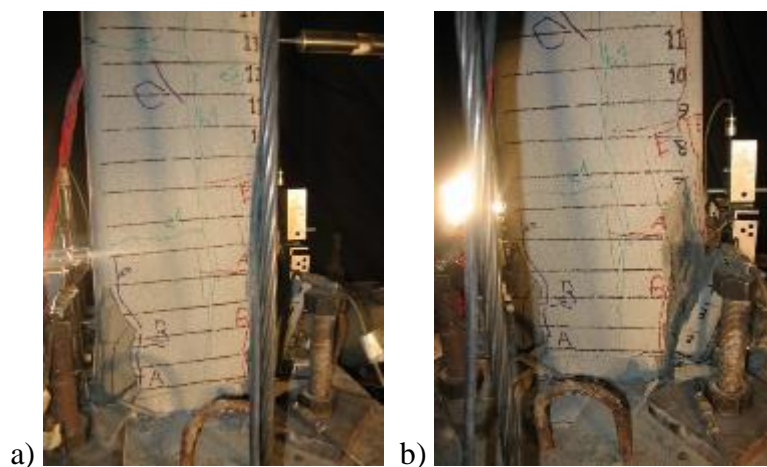
Figure 7.27 : a) North, and b) South view of X26-M after the test finished.

Summary of the seismic behavior of specimen X26-M is shown in Table 7.3.

Table 7.3 : Summary of the seismic behavior of X26-M.

Drift Ratio (%)	δ (mm/mm)	P (kN)	Observations
0.1	±1.2	8.00/-9.30	No crack was observed.
2.5	±3	16.20/-16.90	First flexural cracks was observed.
0.5	±6	24.90/-25.50	First flexural crack at column-footing interface was observed
0.75	±9	30.3/-29.2	
1	±12	31.7/-30.0	Flexural shear cracks were observed.
1.5	±18	33.4/-31.1	
2	±24	33.0/-26.6	Crushing started at the interface of the column and footing at the compression zone
2.5	±30	29.7/-24.0	Crushing started at the interface of the column and footing at the compression zone
3	±36	25.3/-22.5	
3.5	±42	24/-22	Concrete cover spalled at the south side of the column at the tension zone
4	±48	23.0/-19.5	
4.5	±54	22.1/-18	Concrete cover spalled at the north side of the column at the compressive zone. Concrete crushed at the south side of the column
5	±60	21.5/-17.1	
6	±72	19.5/-16.8	
7	±84	14.6/-14.0	Specimen underwent excessive deformation out of its axis and test was ended by decreasing axial load.

Force-displacement relationship of X26-M is presented in Figure 7.28. First flexural crack, first shear crack, first vertical crack, yielding of starter bar, crushing of concrete cover, spalling of concrete cover, fracture of starter bar, maximum strain on the starter bar and maximum strain on the longitudinal bar are marked on the figure. As seen from Figure 7.28, strength loss was observed.
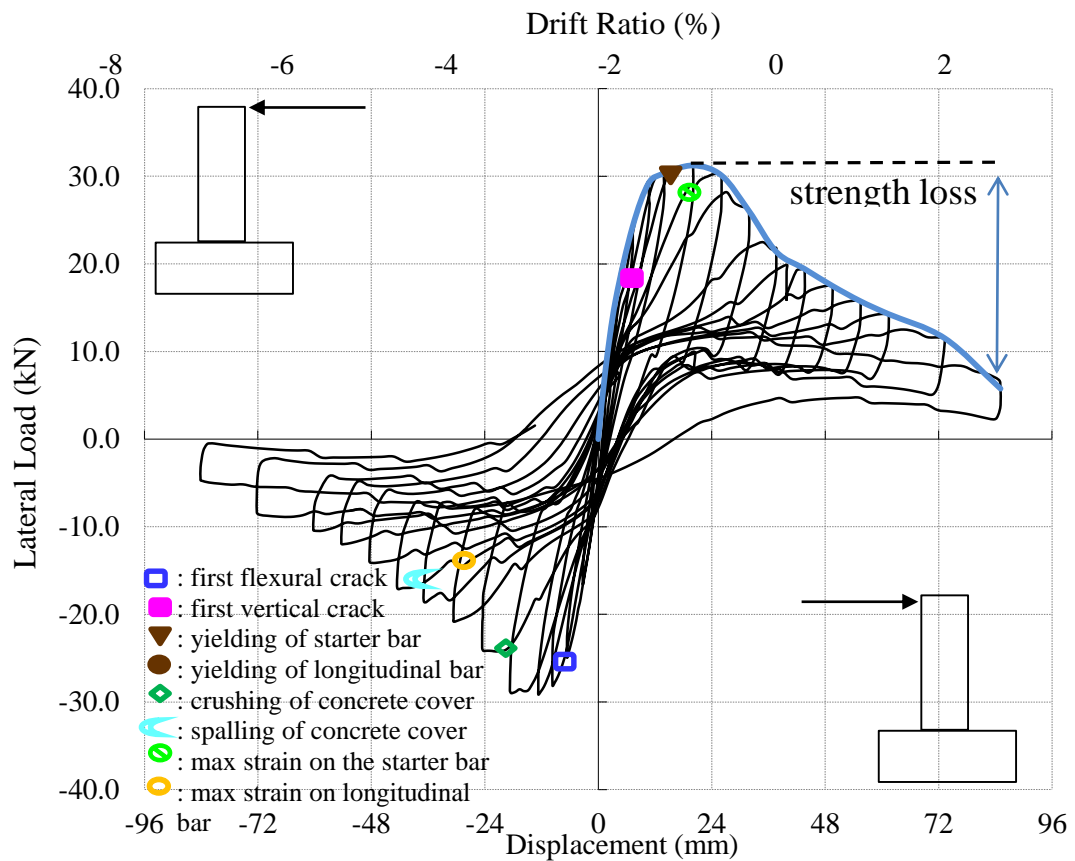
Figure 7.28 : Lateral load versus displacement for X26-M.

Average experimental moment-curvature relationships obtained for critical sections of X26-M are presented in Figure 7.28. For the calculation of moment-curvature relationships, the average curvature values which were obtained for the ranges of 0-20 mm, 20-150 mm and 150-300 mm heights above the footing were taken into account. As seen from Figure 7.28, the curvature values of the member measured in 20-150 mm and 150-300 mm height above the support are in the order of 5.10-5 (1/ mm), while the curvatures measured in 0-20 mm height are in the order of 3.10-3 (1/ mm). According to Figure 7.28, it is of interest to note that the damage is accumulated especially in 20 mm height of the member from top of the base according to the moment-curvature relationships.
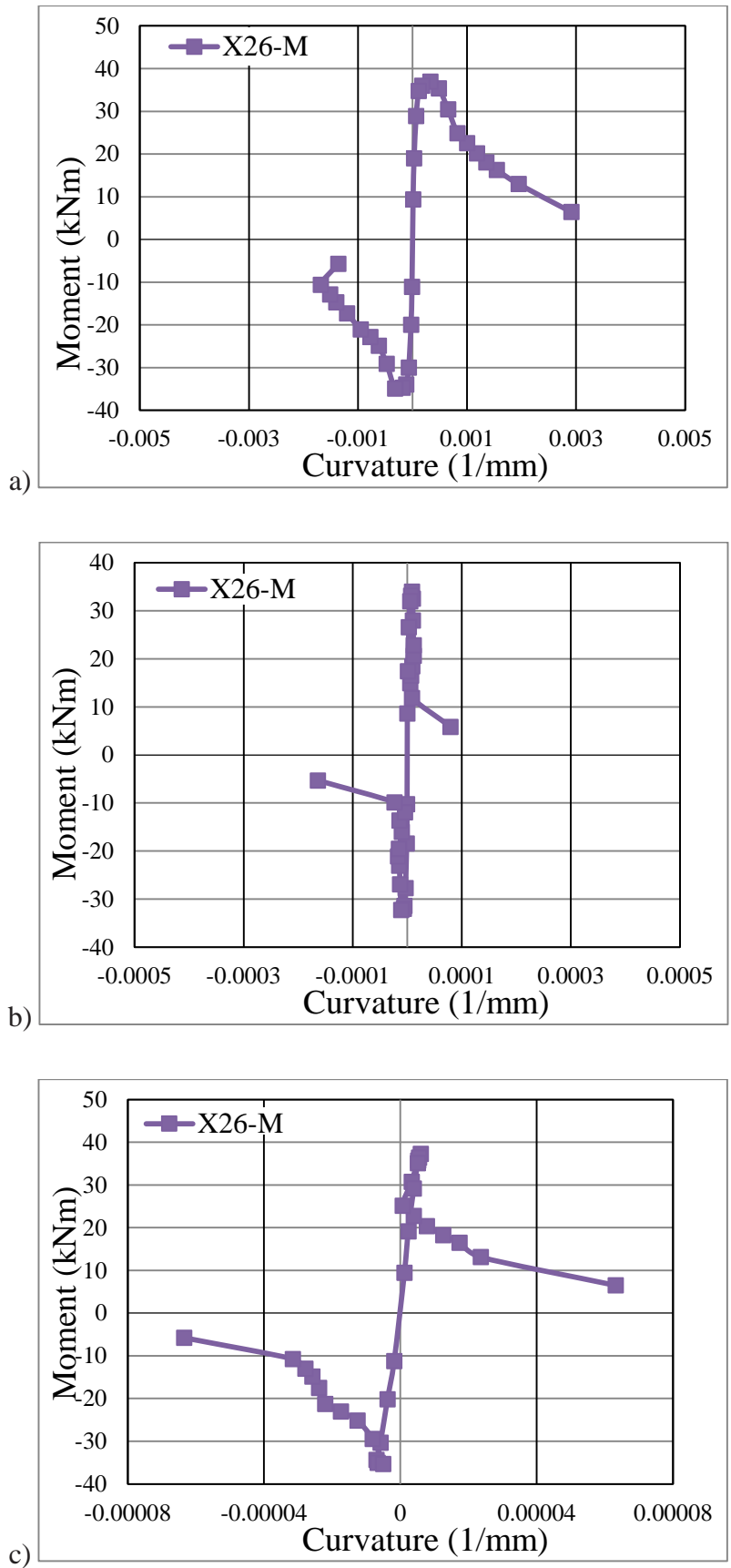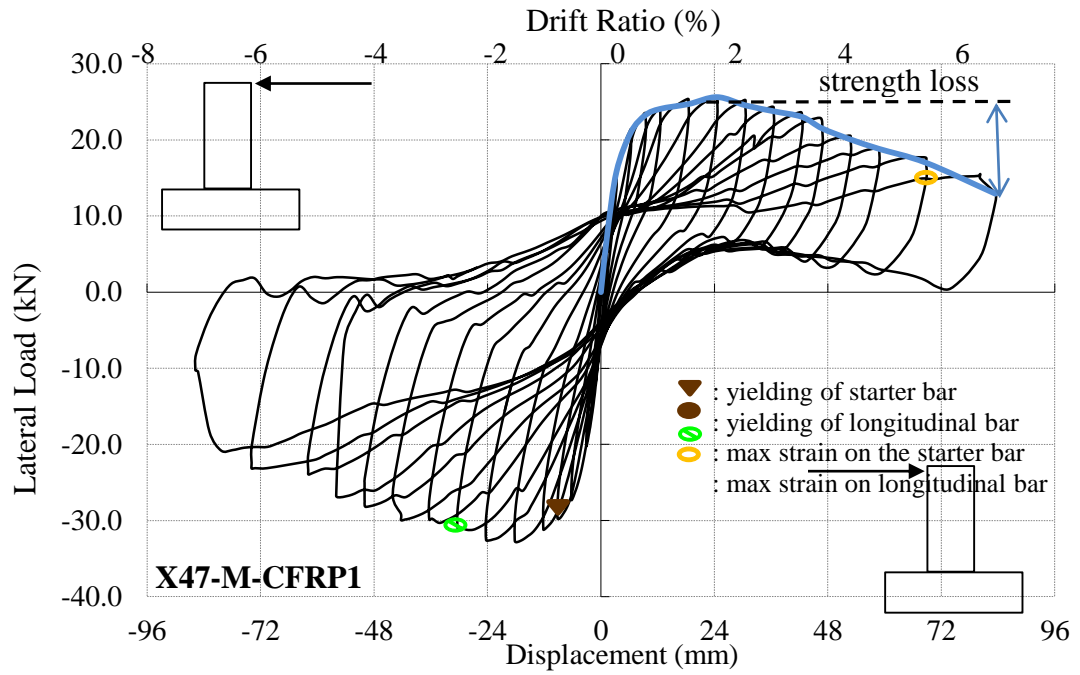
Figure 7.29 : Moment-curvature relationships obtained for a) 20 mm, b) 150 mm, c) 300 mm gauge lengths.

According to the data from the straingauges on the starter bars, the maximum strain while pushing was 0.00182, measured from the straingauge at +100 mm above the footing when P=32.14 kN at 0.02 drift ratio; the maximum strain while pulling was − 0.00095, measured from the straingauge at +100 mm above the footing when P=-- 30.14 kN at -0.01 drift ratio; the maximum strain while pushing was 0.00297, measured from the straingauge at +200 mm above the footing when P=33.46 kN at 0.015 drift ratio; the maximum strain while pulling was -0.00155, measured from the straingauge at +200 mm above the footing when P=-28.33 kN at -0.01 drift ratio. According to the data from the straingauges on the longitudinal bars of the X26-M, the maximum strain while pushing was 0.00069, measured from the straingauge at +100 mm above the footing when P=-6.45 kN at -0.07 drift ratio; the maximum strain while pulling was -0.00028, measured from the straingauge at +100 mm above the footing when P=-16.72 kN at -0.0025 drift ratio; the maximum strain while pushing was 0.00046, measured from the straingauge at +200 mm above the footing when P=31.79 kN at 0.01 drift ratio; the maximum strain while pulling was -0.00034, measured from the straingauge at +200 mm above the footing when P=-23.12 kN at -0.005 drift ratio. Strain distribution of the starter bars and longitudinal bars of X26-M while pushing and pulling are shown in Figure 7.30 and Figure 7.31. As seen from Figure 7. 30 and Figure 7.31, the strain values of starter bars reach yield strain while pushing.
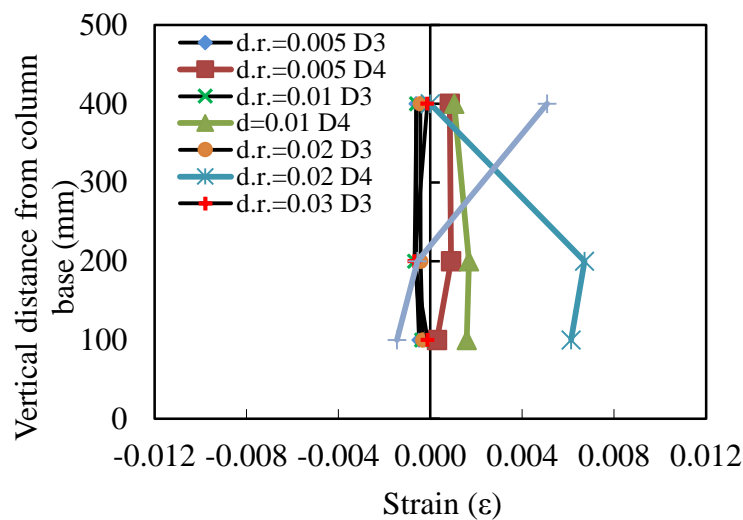
a)
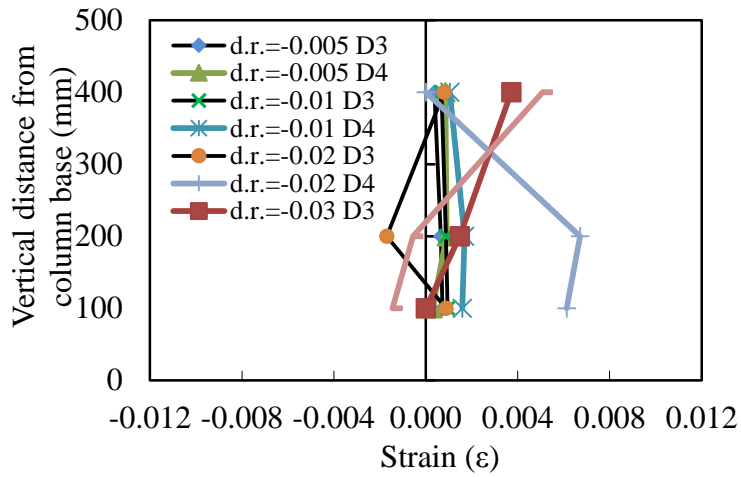
b)

Figure 7.30 : Strain distribution of the starter bars of X26-M a) while pushing, b) while pulling.
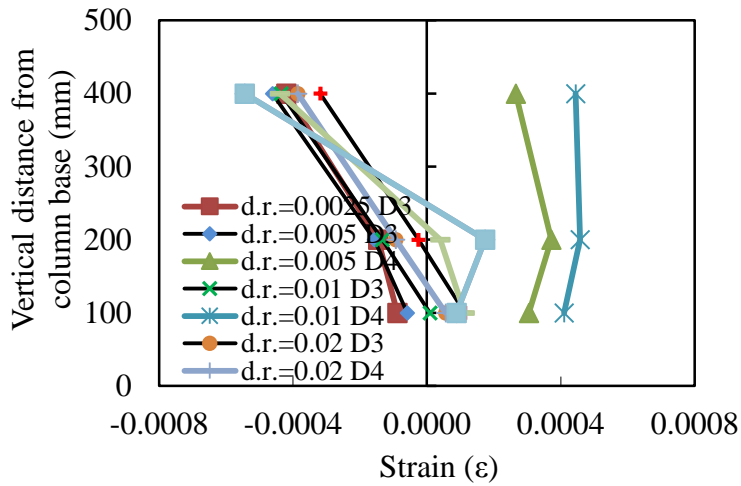
a)
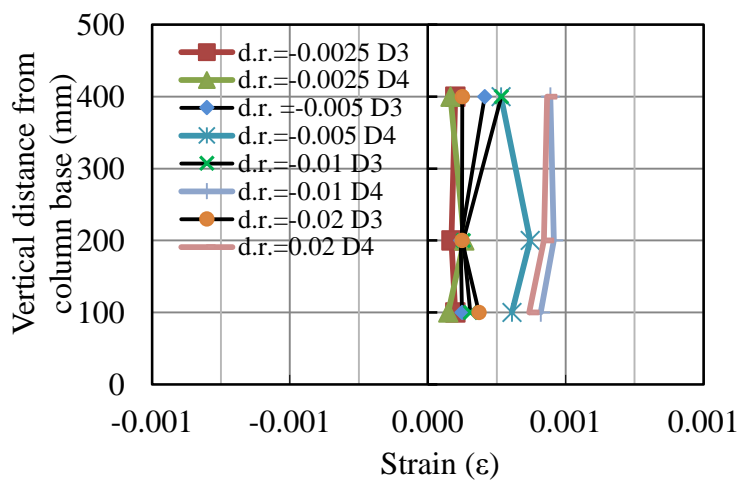
b)

Figure 7.31 : Strain distribution of the longitudinal bars of X26-M a) while pushing, b) while pulling.

7.4 X47-M-CFRP1

X47-M-CFRP1 is the both rehabilitated/retrofitted specimen which was rehabilitated after exposed to accelerated corrosion process, then the specimen was retrofitted with 1-layer CFRP. Test was examined at 22.3.2012. Axial load of the specimen was 124 kN, and test was performed displacement-controlled. The view of the specimen X47-M-CFRP1 before the starting of test was shown in Figure 7.32.

Figure 7.32 : The view of the specimen X47-M-CFRP1

There were no observed crack on the surface of the specimen X47-M-CFRP1 during the experiment. Wrapping of the specimen X47-M-CFRP1 prevent the cracks on the surface but all damage was accumulated at the base of the specimen. This type of damage may be quite disadvantageous since the distribution of plastic deformations through the potential plastic hinge length is prevented.

First flexural crack was observed at interface of the column and footing, during loading to target displacement 3 mm(drift ratio 0.25%). During the loading to target displacement -54 mm(drift ratio -4.00%) tearing at the CFRP was observed at +10 mm height due to the crushing of the wrapped concrete. During the loading to target displacement 84 mm(drift ratio 7%) one of the starter bar was ruptured.

Summary of the seismic behavior of specimen X47-M-CFRP1 is shown in Table 7.4.

Table 7.4 : Summary of the seismic behavior of X47-M-CFRP1.

Drift Ratio (%)	δ (mm/mm)	P (kN)	Observations
0.1	±1.2	7.80/-12.20	No crack was observed.
2.5	±3	16.10/-20.50	First flexural crack at column-footing interface was observed.
0.5	±6	21.7/-27.6	
0.75	±9	24.2/-30.7	
1	±12	25.4/-32.5	
1.5	±18	26.8/-34.5	
2	±24	28.5/-35.3	
2.5	±30	28.7/-34.5	
3	±36	28.4/-33.8	
3.5	±42	27.8/-34.2	
4	±48	26.9/-33.0	
4.5	±54	26.0/-33.5	Separation of CFRP at the interface of the column and footing at the compression zone.
5	±60	25.3/-30.2	
6	±72	25.2/-30.9	
7	±84	23.0/-19.9	Starter bar ruptured.

Force-displacement relationship of X47-M-CFRP1 is presented in Figure 7.33. Yielding of starter bar, yielding of longitudinal bar, fracture of starter bar, maximum strain on the starter bar and maximum strain on the longitudinal bar are marked on the figure. As seen from Figure 7.33, strength loss was observed.

Average experimental moment-curvature relationships obtained for critical sections of X47-M-CFRP1 are presented in Figure 7.34. For the calculation of moment-curvature relationships, the average curvature values which were obtained for the ranges of 0-20 mm, 20-150 mm and 150-300 mm heights above the footing were taken into account. As seen from Figure 7.34, the curvature values of the member measured in 20-150 mm and 150-300 mm height above the support are in the order of 5.10^{-5} (1/ mm), while the curvatures measured in 0-20 mm height are in the order of 3.10^{-3} (1/ mm). According to Figure 7.34, it is of interest to note that the damage is accumulated especially in 20 mm height of the member from top of the base according to the moment-curvature relationships.

Figure 7.33 : Lateral load versus displacement for X47-M-CFRP1.

a)

b)

c)
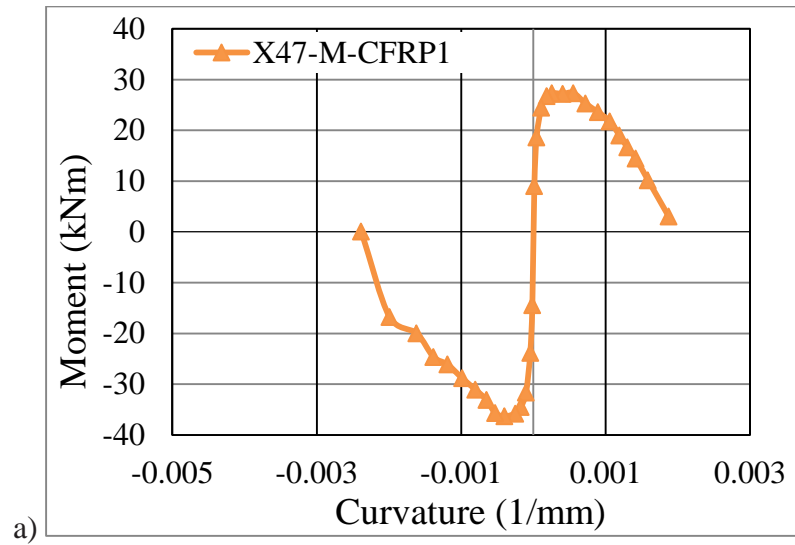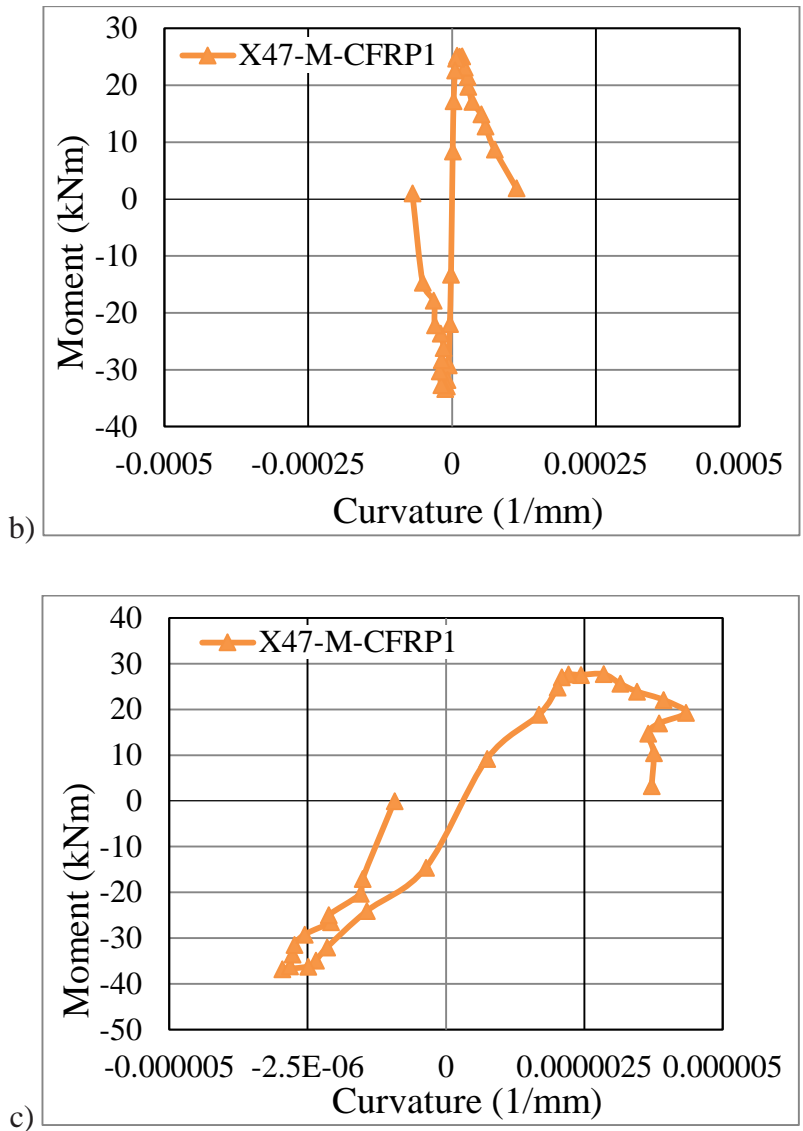
Figure 7.34 : Moment-curvature relationships obtained for a) 20 mm, b) 150 mm, c) 300 mm gauge lengths.

According to the data from the straingauges on the starter bars, the maximum strain while pushing was -0.0011781, measured from the straingauge at +100 mm above the footing when P=25.41 kN at 0.01 drift ratio; the maximum strain while pulling was 0.0027305, measured from the straingauge at +100 mm above the footing when P=-34.57 kN at -0.015 drift ratio; the maximum strain while pushing was -0.0007924, measured from the straingauge at +200 mm above the footing when P=7.78 kN at 0.001 drift ratio; the maximum strain while pulling was 0.0058362, measured from the straingauge at +200 mm above the footing when P=-34.58 kN at -0.025 drift ratio. According to the data from the straingauges on the longitudinal bars of the X47-M-CFRP1, the maximum strain while pushing was -0.0002333, measured from the

64

straingauge at +100 mm above the footing when P=22.92 kN at 0.07 drift ratio; the maximum strain while pulling was 0.0000867, measured from the straingauge at +100 mm above the footing when P=-32.45 kN at -0.01 drift ratio; the maximum strain while pushing was -0.0001457, measured from the straingauge at +200 mm above the footing when P=22.92 kN at 0.07 drift ratio; the maximum strain while pulling was 0.0000867, measured from the straingauge at +200 mm above the footing when P=21.71 kN at 0.005 drift ratio. Strain distribution of the starter bars and longitudinal bars of X47-M-CFRP1 while pushing and pulling are shown in Figure 7.35 and Figure 7.36. As seen from Figure 7. 35 and Figure 7.36, the strain values of starter bars reach yield strain while pushing.

a)

b)
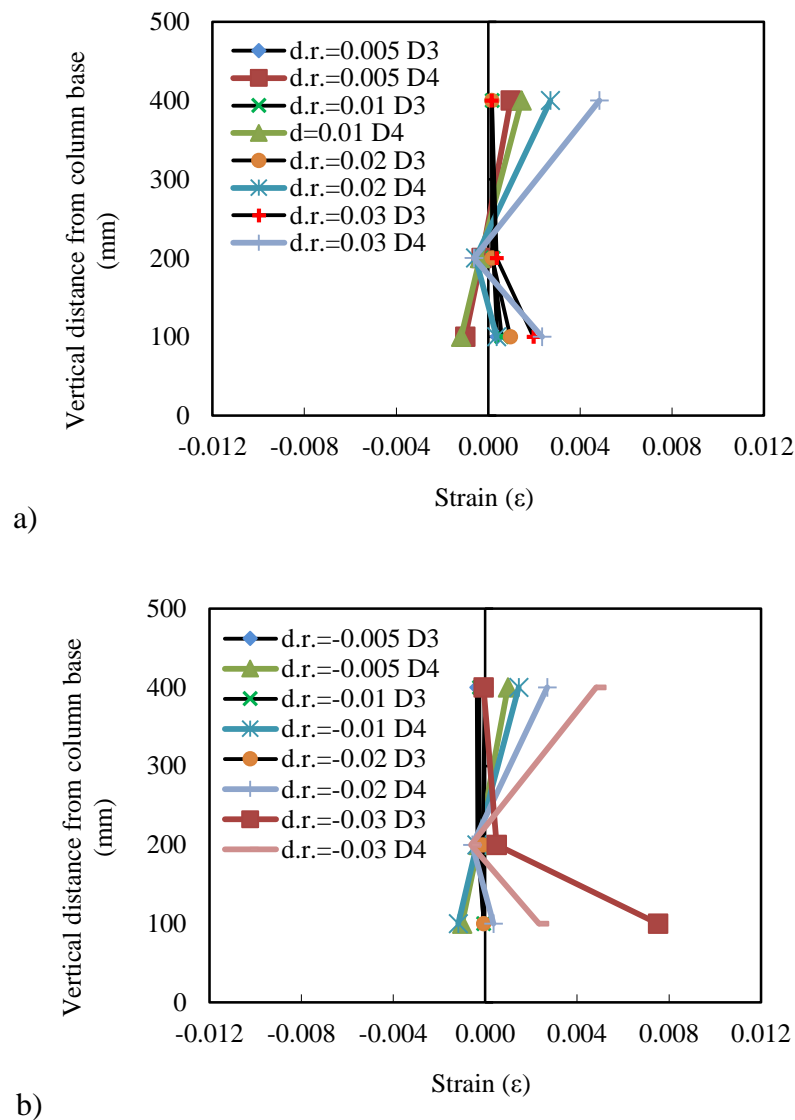
Figure 7.35 : Strain distribution of the starter bars of X47-M-CFRP1 a) while pushing, b) while pulling.
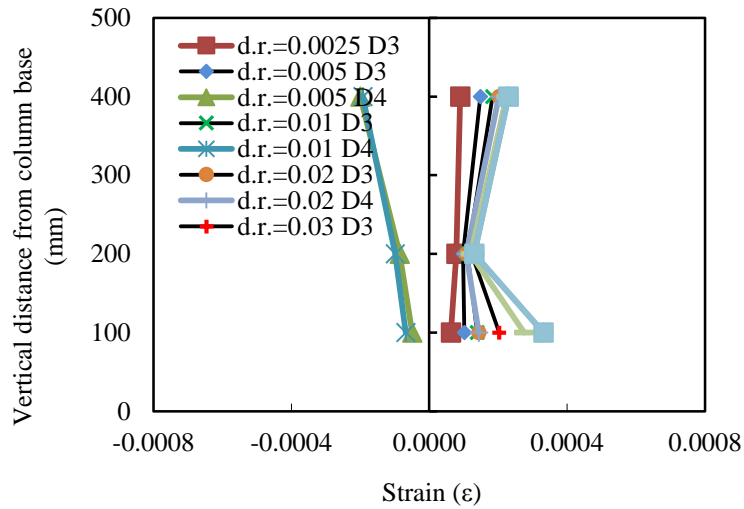
a)
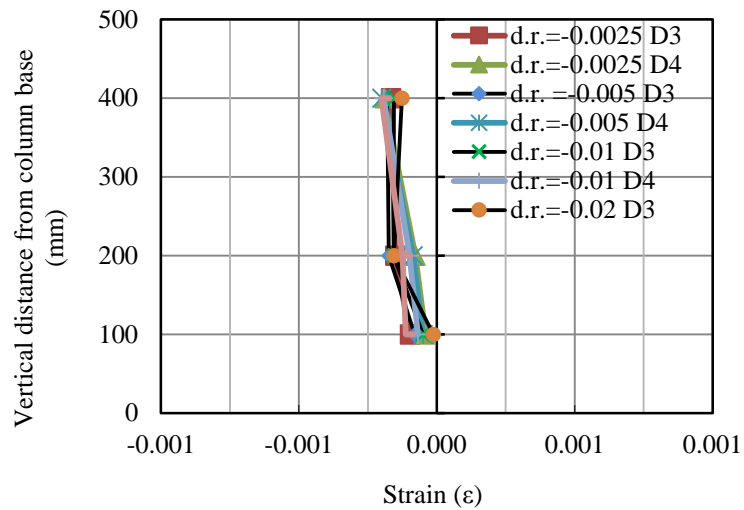
b)

Figure 7.36 : Strain distribution of the longitudinal bars of X47-M-CFRP1 a) while pushing, b) while pulling.

7.5 X43-M-CFRP2

X43-M-CFRP2 is the both rehabilitated/retrofitted specimen which was rehabilitated after exposed to accelerated corrosion process, then the specimen was retrofitted with 2-layer CFRP. Test was examined at 15.2.2012. Axial load of the specimen was 124 kN, and test was performed displacement-controlled. The view of the specimen X43-M-CFRP2 before the starting of test was shown in Figure 7.37.

Figure 7.37 : The view of the specimen X43-M-CFRP2 before the starting of test

There were no observed crack on the surface of the specimen X43-M-CFRP2 during the experiment. Wrapping of the specimen X43-M-CFRP2 prevent the cracks on the surface but all damage was accumulated at the base of the specimen. This type of damage may be quite disadvantageous since the distribution of plastic deformations through the potential plastic hinge length is prevented.

First flexural crack was observed at interface of the column and footing, during loading to target displacement -3 mm(drift ratio -0.25%). During the loading to target displacement 48 mm(drift ratio 3.50%) one of the starter bar was ruptured. Summary of the seismic behavior of specimen X43-M-CFRP2 is shown in Table 7.5.

Force-displacement relationship of X43-M-CFRP2 is presented in Figure 7.38. Yielding of starter bar, yielding of longitudinal bar, maximum strain on the starter bar and maximum strain on the longitudinal bar are marked on the figure. As seen from Figure 7.38, strength loss was observed.

Table 7.5 : Summary of the seismic behavior of X43-M-CFRP2.

Drift Ratio (%)	δ (mm/mm)	P (kN)	Observations
0.1	±1.2	12.6/-9.8	No crack was observed.
2.5	±3	21.9/-18.1	First flexural crack at column-footing interface was observed.
0.5	±6	29.3/-24.6	
0.75	±9	32.4/-26.9	
1	±12	33.6/-27.5	
1.5	±18	35.4/-29.6	
2	±24	35.5/-30.1	
2.5	±30	34.5/-31.3	
3	±36	33.5/-30.8	
3.5	±42	34.6/-30.0	
4	±48	32.7/-20.0	Starter bar of the specimen was ruptured.
4.5	±54	32.5/-18.5	Separation of CFRP at the interface of the column and footing at the compression zone.
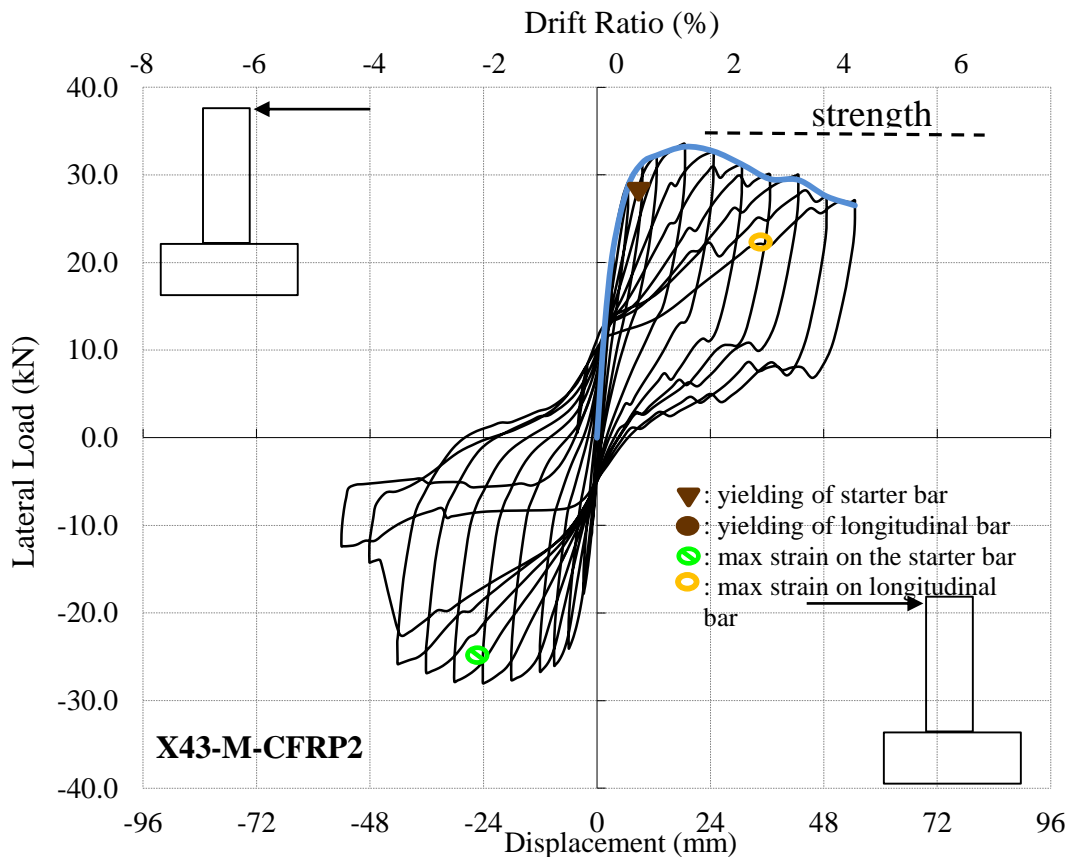
Figure 7.38 : Lateral load versus displacement for X43-M-CFRP2.

Average experimental moment-curvature relationships obtained for critical sections of X43-M-CFRP2 are presented in Figure 7.39. For the calculation of moment-curvature

relationships, the average curvature values which were obtained for the ranges of 0-20 mm, 20-150 mm and 150-300 mm heights above the footing were taken into account. As seen from Figure 7.39, the curvature values of the member measured in 20-150 mm and 150-300 mm height above the support are in the order of 5.10-5 (1/ mm), while the curvatures measured in 0-20 mm height are in the order of 3.10-3 (1/ mm). According to Figure 7.39, it is of interest to note that the damage is accumulated especially in 20 mm height of the member from top of the base according to the moment-curvature relationships.

a)

b)
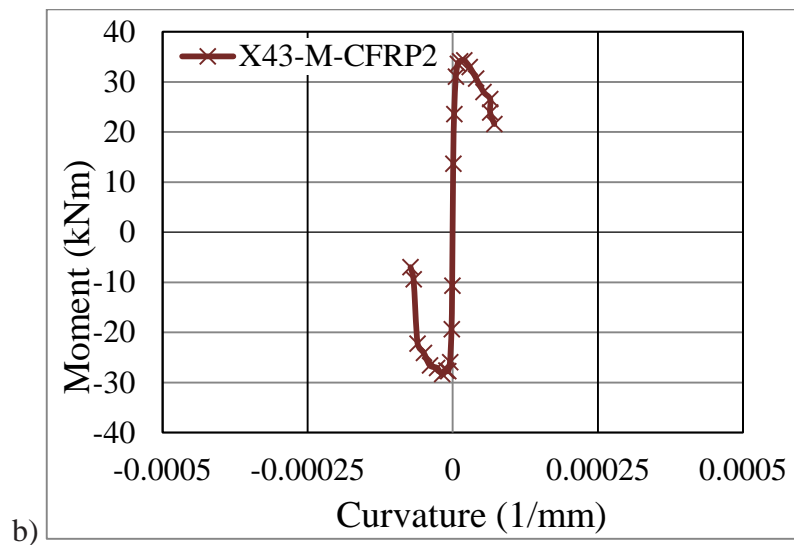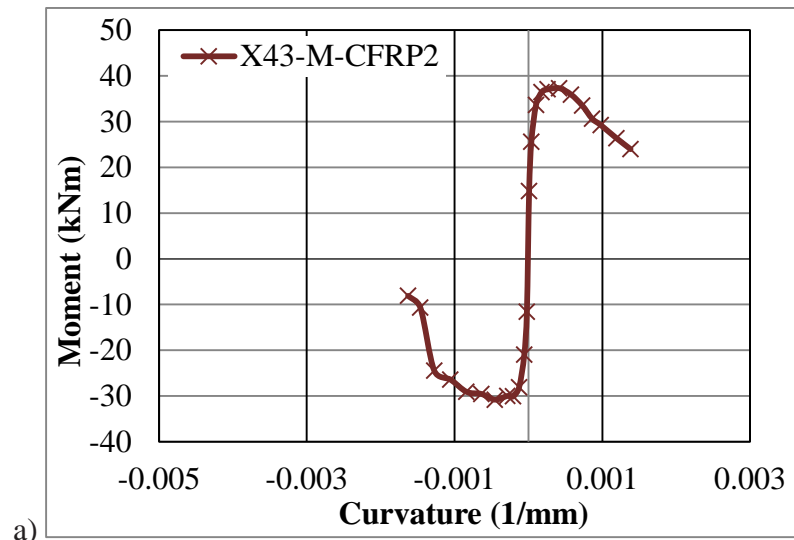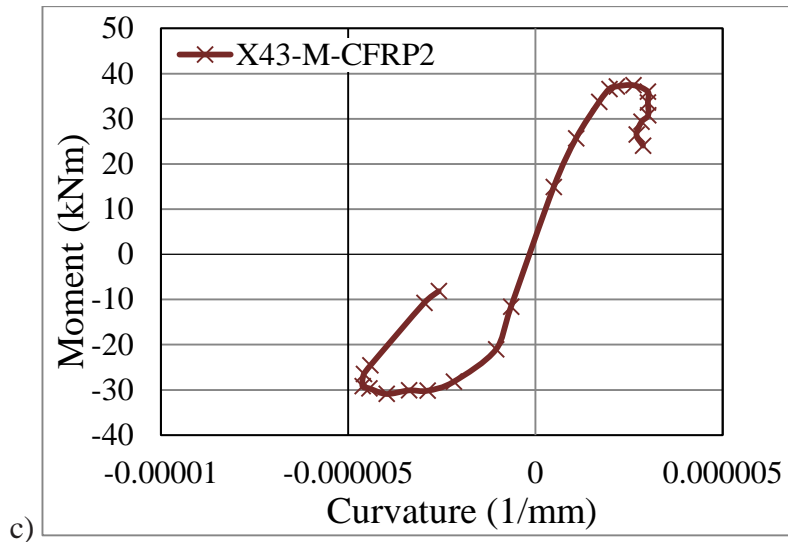
Figure 7.39 : Moment-curvature relationships obtained for a) 20 mm, b) 150 mm, c) 300 mm gauge lengths.

According to the data from the straingauges on the starter bars, the maximum strain while pushing was -0.0005258, measured from the straingauge at +100 mm above the footing when P=18.3 kN at 0.04 drift ratio; the maximum strain while pulling was 0.00079614, measured from the straingauge at +100 mm above the footing when P=-30.97 kN at -0.03 drift ratio; the maximum strain while pushing was -0.000288832, measured from the straingauge at +200 mm above the footing when P=22.04 kN at 0.0025 drift ratio; the maximum strain while pulling was 0.003811283, measured from the straingauge at +200 mm above the footing when P=-5.46 kN at -0.045 drift ratio. According to the data from the straingauges on t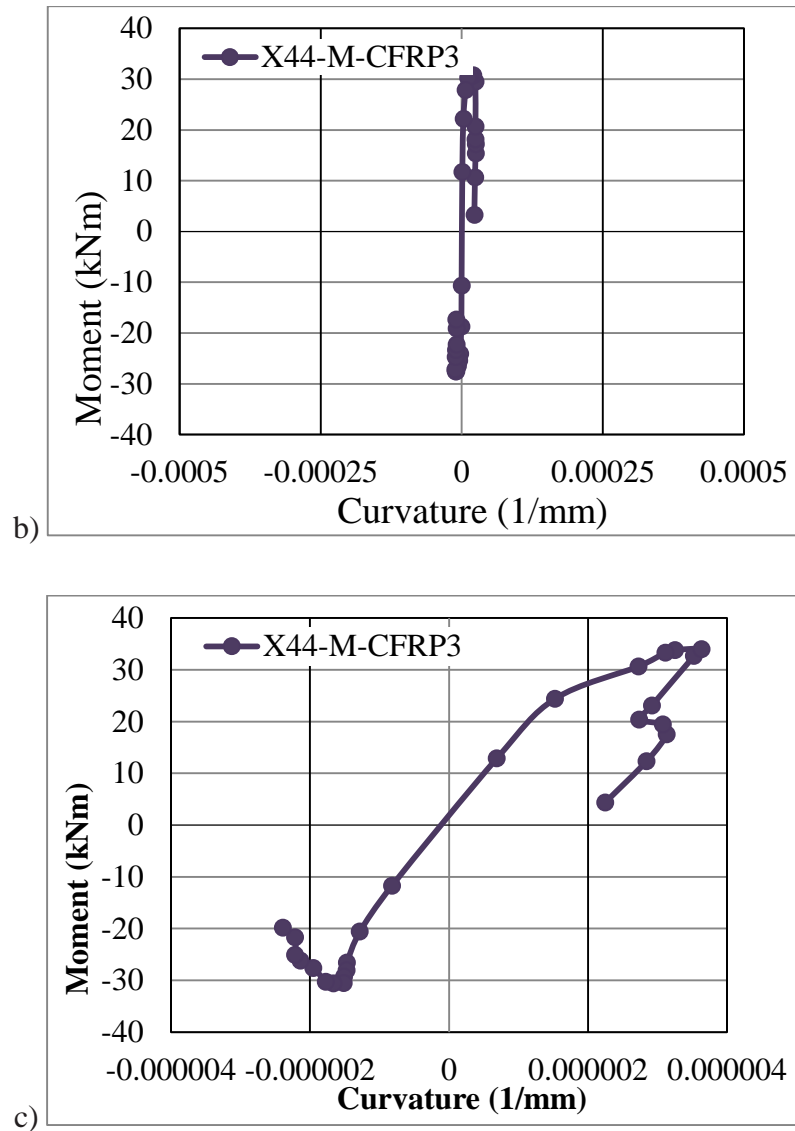he longitudinal bars of the X43-M-CFRP2, the maximum strain while pushing was -0.0001830, measured from the straingauge at +100 mm above the footing when P=20.69 kN at 0.045 drift ratio; the maximum strain while pulling was 0.00007818, measured from the straingauge at +100 mm above the footing when P=-26.95 kN at -0.0075 drift ratio; the maximum strain while pushing was -0.000088, measured from the straingauge at +200 mm above the footing when P=21.38 kN at 0.0025 drift ratio; the maximum strain while pulling was 0.0001553867, measured from the straingauge at +200 mm above the footing when P=-29.61 kN at -0.015 drift ratio. Strain distribution of the starter bars and longitudinal bars of X43-M-CFRP2 while pushing and pulling are shown in Figure 7.40 and Figure 7.41. As seen from Figure 7. 40 and Figure 7.41 the strain values of starter bars reach yield strain while pushing.

70
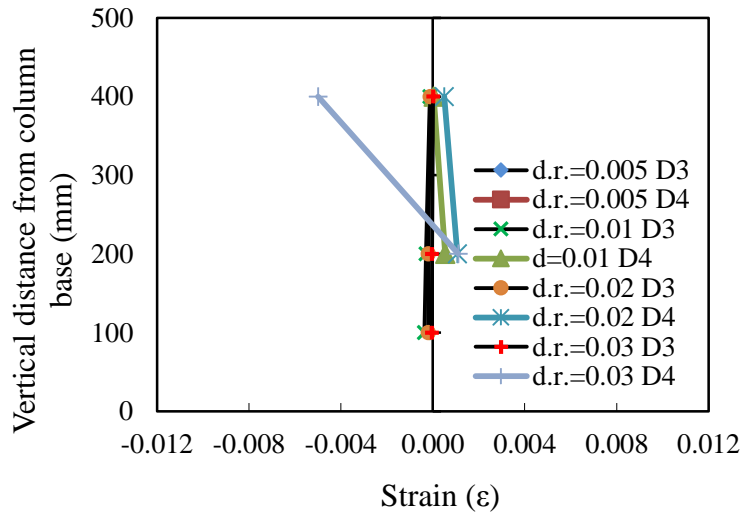
a)
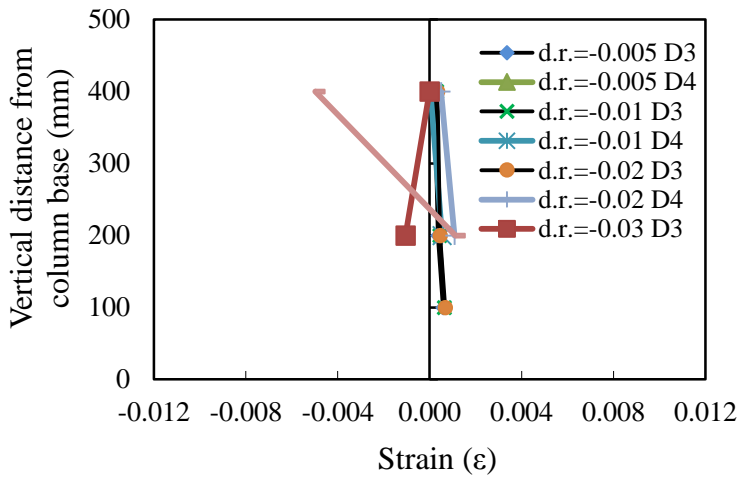
b)

Figure 7.40 : Strain distribution of the starter bars of X47-M-CFRP1 a) while pushing, b) while pulling.

a)

71

b)
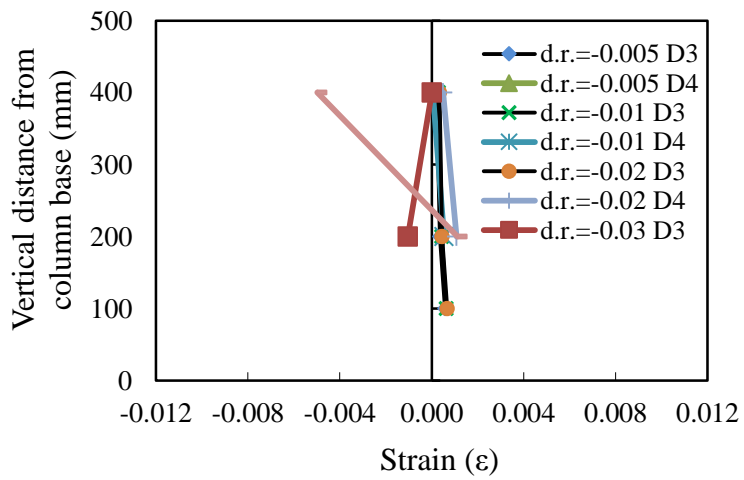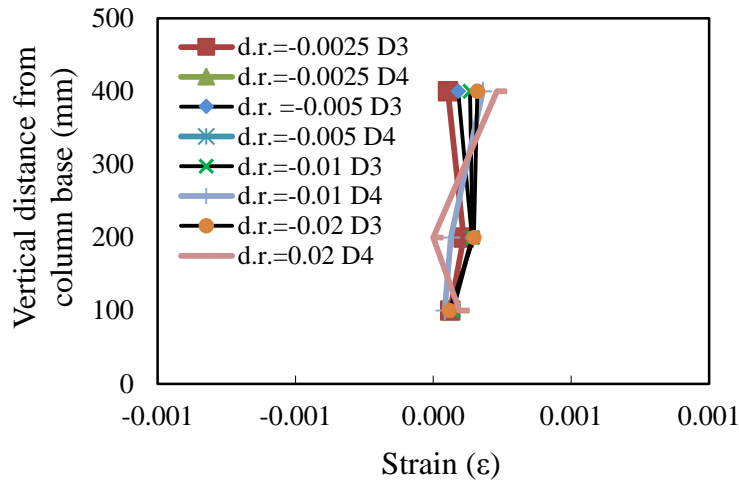
Figure 7.41 : Strain distribution of the longitudinal bars of X47-M-CFRP1 a) while pushing, b) while pulling.

7.6 X44-M-CFRP3

X44-M-CFRP3 is the both rehabilitated/retrofitted specimen which was rehabilitated after exposed to accelerated corrosion process, then the specimen was retrofitted with 3-layer CFRP. Test was examined at 1.3.2012. Axial load of the specimen was 124 kN, and test was performed displacement-controlled. The view of the specimen X44-M-CFRP3 before the starting of test was shown in Figure 7.42.

Figure 7.42 : The view of the specimen X44-M-CFRP3 before the starting of test.

There were no observed crack on the surface of the specimen X44-M-CFRP3 during the experiment. Wrapping of the specimen X44-M-CFRP3 prevent the cracks on the surface but all damage was accumulated at the base of the specimen. This type of damage may be quite disadvantageous since the distribution of plastic deformations through the potential plastic hinge length is prevented.

First flexural crack was observed at interface of the column and footing, during loading to target displacement 3 mm(drift ratio 0.25%). All the damages was observed at interface of the column and footing. During the loading to target displacement 30 mm(drift ratio 2.50%) one of the starter bar was ruptured and load was get down a little bit. During the loading to target displacement 60 mm(drift ratio 5.00%) second starter bar was ruptured too. At this point, cracks at the interface of the column and footing was measured as 2 cm. Summary of the seismic behavior of specimen X44-M-CFRP3 is shown in Table 7.6.

Table 7.6 : Summary of the seismic behavior of X44-M-CFRP3.

Drift Ratio (%)	δ (mm/mm)	P (kN)	Observations
0.1	±1.2	10.90/-9.90	No crack was observed.
2.5	±3	20.80/-17.60	First flexural crack at column-footing interface was observed.
0.5	±6	26.6/-23.2	
0.75	±9	29.4/-25.1	
1	±12	30.6/-26.8	
1.5	±18	32.3/-29.2	
2	±24	32.5/-30.8	
2.5	±30	26.4/-32.4	First starter bar was ruptured.
3	±36	25.4/-32	
3.5	±42	26.1/-31.1	
4	±48	25.9/-31.6	
4.5	±54	22.3/-30.1	Separation of CFRP at the interface of the column and footing at the compression zone.
5	±60	17.3/-30.4	Second starter bar was ruptured. Due to downed load P, experiment was over.

Force-displacement relationship of X44-M-CFRP3 is presented in Figure 7.43. Yielding of starter bar, yielding of longitudinal bar, maximum strain on the starter bar and maximum strain on the longitudinal bar are marked on the figure. As seen from Figure 7.43, strength loss was observed.
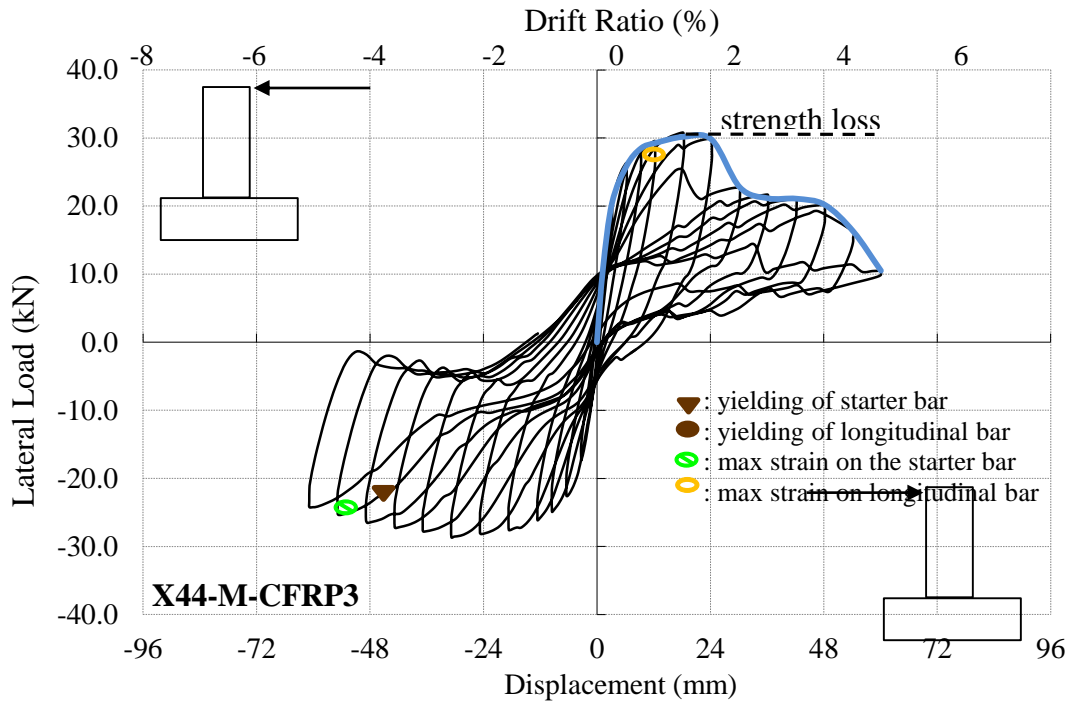
Figure 7.43 : Lateral load versus displacement for X44-M-CFRP3.

Average experimental moment-curvature relationships obtained for critical sections of X44-M-CFRP3 are presented in Figure 7.44. For the calculation of moment-curvature relationships, the average curvature values which were obtained for the ranges of 0-20 mm, 20-150 mm and 150-300 mm heights above the footing were taken into account. As seen from Figure 7.44, the curvature values of the member measured in 20-150 mm and 150-300 mm height above the support are in the order of 5.10-5 (1/ mm), while the curvatures measured in 0-20 mm height are in the order of 3.10-3 (1/ mm).

a)

b)

c)
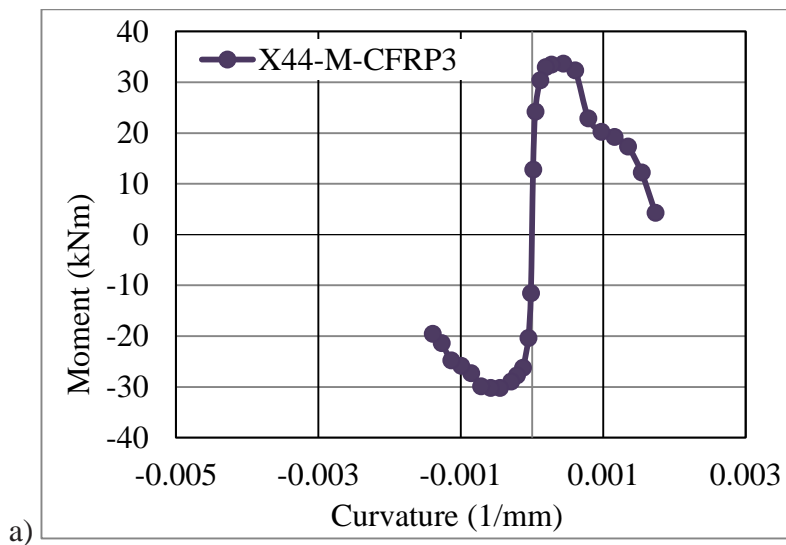
Figure 7.44 : Moment-curvature relationships obtained for a) 20 mm, b) 150 mm, c) 300 mm gauge lengths.

According to the data from the straingauges on the starter bars, the maximum strain while pushing was -0.0005258, measured from the straingauge at +100 mm above the footing when P=18.3 kN at 0.04 drift ratio; the maximum strain while pulling was 0.00079614, measured from the straingauge at +100 mm above the footing when P=-30.97 kN at -0.03 drift ratio; the maximum strain while pushing was -0.000288832, measured from the straingauge at +200 mm above the footing when P=22.04 kN at 0.0025 drift ratio; the maximum strain while pulling was 0.003811283, measured from the straingauge at +200 mm above the footing when P=-5.46 kN at -0.045 drift ratio. According to the data from the straingauges on the longitudinal bars of the X43-M-CFRP2, the maximum strain while pushing was -0.0001830, measured from the

straingauge at +100 mm above the footing when P=20.69 kN at 0.045 drift ratio; the maximum strain while pulling was 0.00007818, measured from the straingauge at +100 mm above the footing when P=-26.95 kN at -0.0075 drift ratio; the maximum strain while pushing was -0.000088, measured from the straingauge at +200 mm above the footing when P=21.38 kN at 0.0025 drift ratio; the maximum strain while pulling was 0.0001553867, measured from the straingauge at +200 mm above the footing when P=-29.61 kN at -0.015 drift ratio. Strain distribution of the starter bars and longitudinal bars of X43-M-CFRP2 while pushing and pulling are shown in Figure 7.45 and Figure 7.46. As seen from Figure 7.45 and Figure 7.46, the strain values of starter bars reach yield strain while pushing.

a)

b)
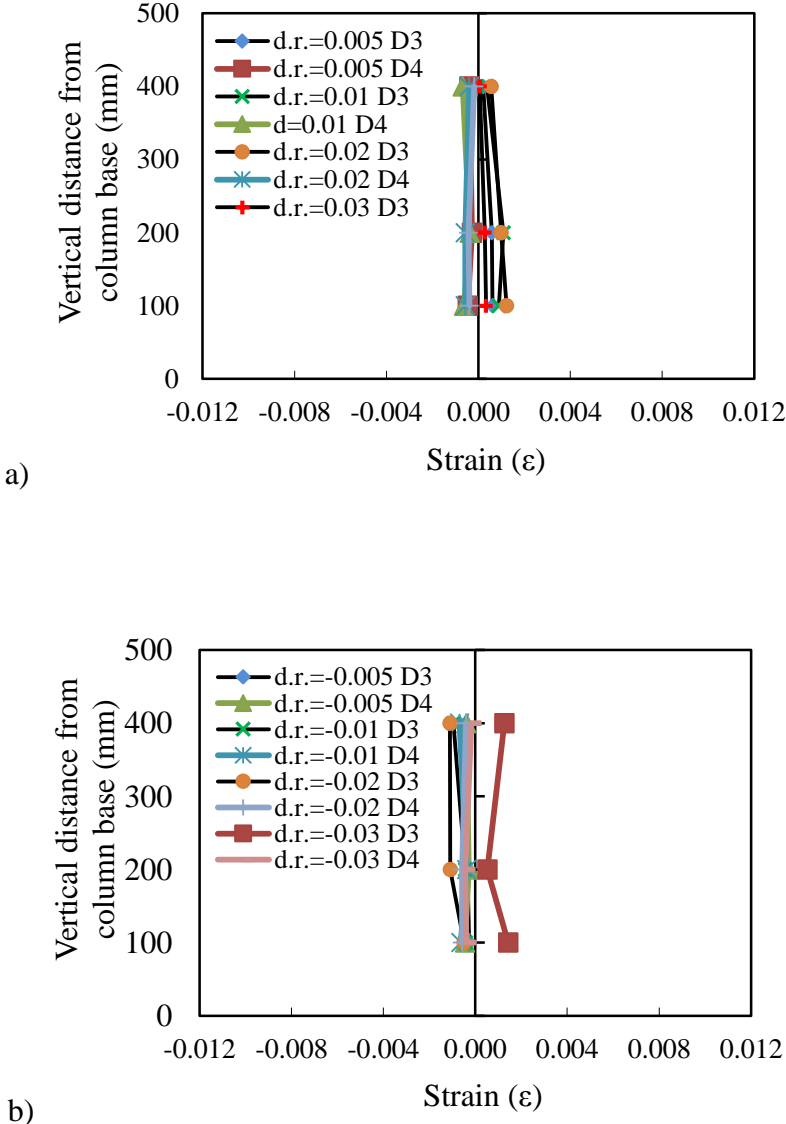
Figure 7.45 : Strain distribution of the starter bars of X47-M-CFRP1 a) while pushing, b) while pulling.

a)

b)
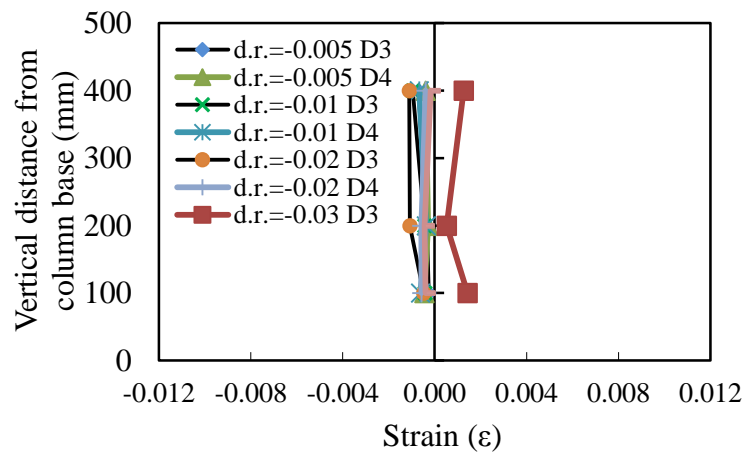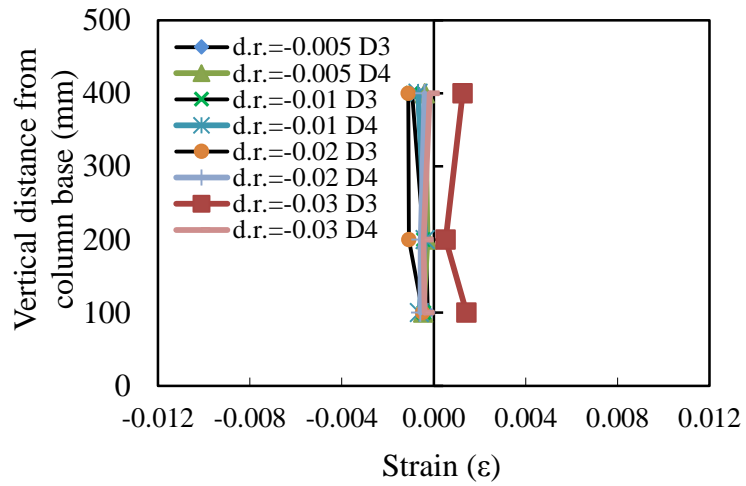
Figure 7.46 : Strain distribution of the longitudinal bars of X47-M-CFRP1 a) while pushing, b) while pulling.

8. OVERALL EVALUATION OF TEST RESULTS

The test results are outlined through hysteretic load-displacement loops, envelopes of these relationships, moment curvature diagrams, energy dissipation capacities and damage mechanisms. The hysteretic lateral load displacement relationships and their envelopes are presented in Figure 8.1 and Figure 8.2, respectively. The second order effect is taken into consideration for the lateral load-drift ratio relationships of the column specimens in Figure 8.2.
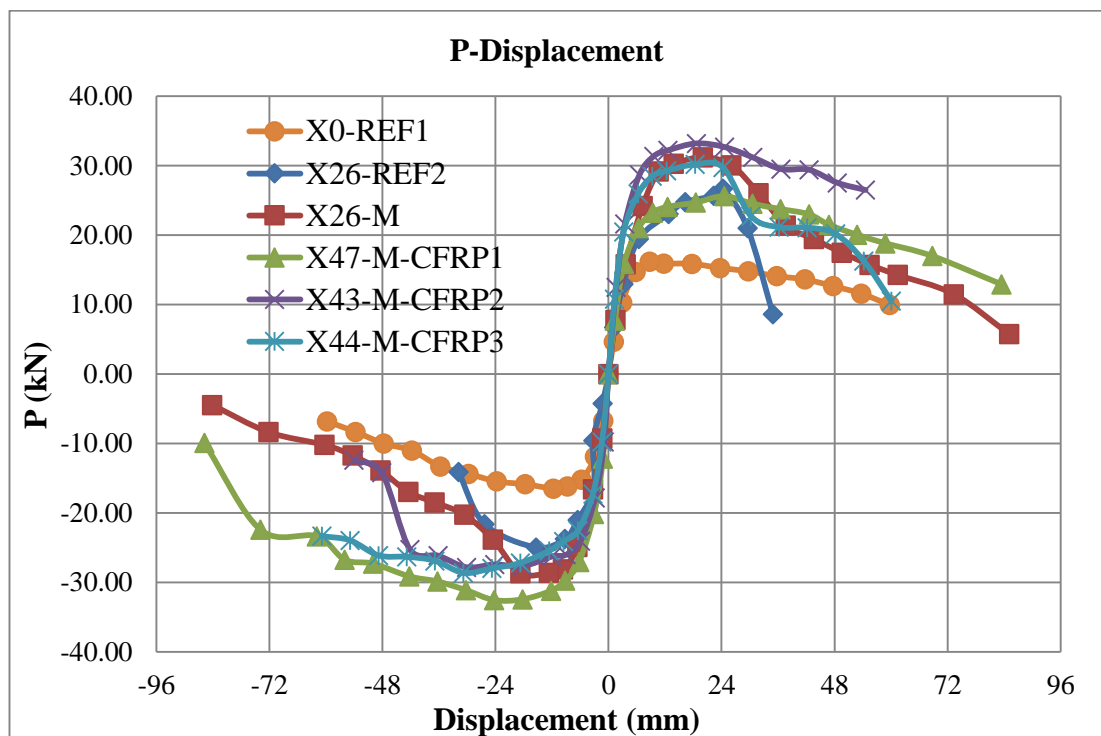
Figure 8.1 : The envelopes of lateral load-drift ratios for the specimens without consideration of the second order effect.

As seen in Figure 8.1 and Figure 8.2, the strength of the specimen X0-REF1 is the lowest among the other specimens. The reference specimen, X0-REF1, without corrosion could not reach its theoretical flexural capacity. This, together with information on yielding of longitudinal bars(strain-distribution graphs) point out that slip dominated the overall behavior of the specimen X0-REF1 due to substandard construction and detailing (low concrete compressive strength, plain reinforcing bars

and insufficient lap-splice length). The specimens with corroded reinforcing bars reached their theoretical capacity, which was determined by considering the cross-sectional areas of the corroded reinforcing bars, which are less than the theoretical capacity calculated considering the uncorroded reinforcing bar cross-sectional areas. The strength of the specimen X26-REF2 is higher than that of X0-REF1 due to corrosion. The corrosion products increased the friction between reinforcing bar and concrete leading to an enhancement in bond characteristics in case of plain reinforcing bars and this caused more efficient utilization of longitudinal reinforcement. However, since the specimens were constructed with extremely low quality concrete and inadequate spacing of transverse reinforcing bars, this increase in strength caused buckling of the longitudinal reinforcing bars causing a sudden significant strength loss upon exceeding the drift ratio of 2%.
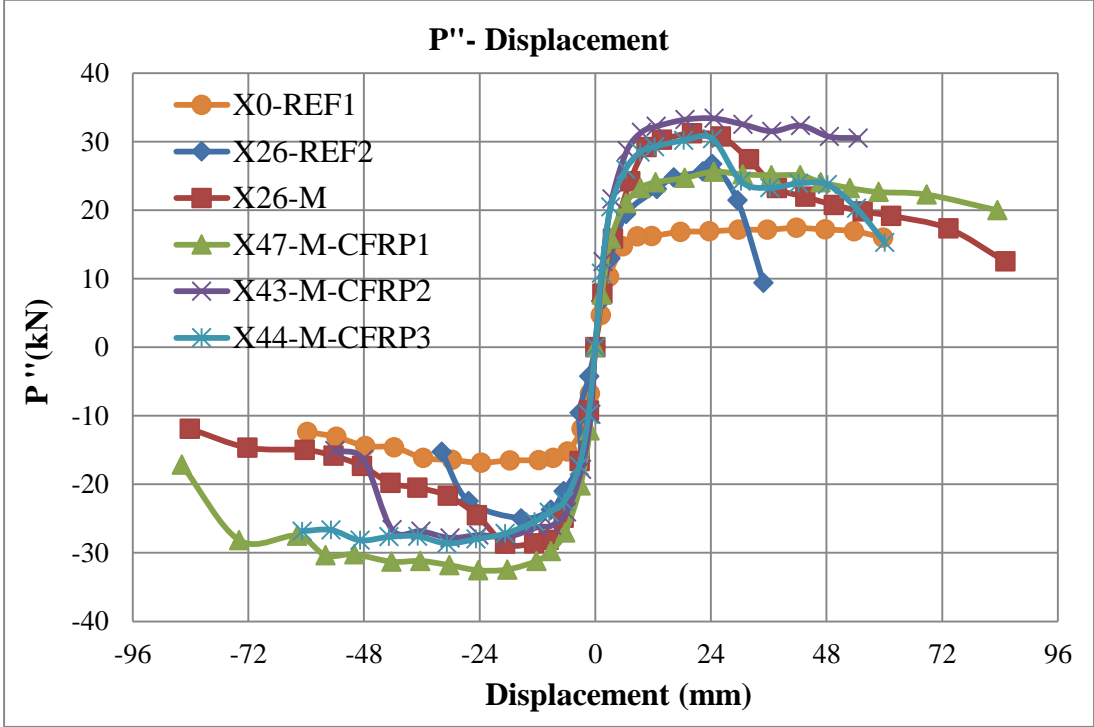
Figure 8.2 : The envelopes of lateral load-drift ratios for the specimens with consideration of the second order effect.

The rehabilitated specimen, X26-M, performed better in terms of strength with respect to X0-REF1 due to prevention of slip of reinforcing bars and usage of high strength structural repair mortar for the concrete cover. Although, the rust products on the surface of the reinforcing bars were cleaned by mechanical cleaning after removal of concrete cover (before application of structural repair mortar), the roughness of the

80

surface of the plain reinforcing bars was still effective for increasing the bond between concrete and reinforcement. The rehabilitated specimen, X26-M, also performed better in terms of displacement capacity with respect to X26-REF2. As the specimens were subjected to high axial load during testing, concrete cover of the specimen X26-REF2 crushed and eventually spalled before starter reinforcing bars reached yield stress due to extremely low compressive strength of concrete. However, the starter reinforcing bars of the rehabilitated specimen, X26-M, yielded before concrete cover crushed resulting from high compressive strength of concrete cover due to high strength of the structural repair mortar. Consequently, the rehabilitated specimen, X26-M behaved in a remarkably ductile manner.

The retrofitted specimens, X47-M-CFRP1, X43-M-CFRP2 and X44-M-CFRP3 experienced an enhancement in terms of strength due to external confinement provided by the CFRP sheets, regardless of the significant cross-section loss of reinforcing bars due to corrosion. The confinement, which was provided by CFRP sheets, improved the bond resistance of the lap-spliced reinforcing bars, retarded the damage of the concrete as well as buckling of reinforcing bars. It should be noted that there was no evidence of concrete distress like crushing or spalling during the autopsy after the test. However, wrapping with CFRP sheets decreased the ductility after two number of layers and also CFRP sheets prevent the cracks on the surface but all damage was accumulated at the interface of the column and footing. This type of damage may be quite disadvantageous since the distribution of plastic deformations through the potential plastic hinge length is prevented. Also when the number of wrapping layers increase, the neutral axis of the column section slide to crushed concrete side, and it cause to longer reinforcement strain. As a result of this starter bars of these specimens were ruptured. Neutral axis of the specimens at maximum moment load is given in Table 8.1 and Figure 8.3 with ruptured bars.

Table 8.1 : Neutral axis of the specimens at maximum moment load (Distance from middle of the column section)

	X0-REF1	X26-REF2	X26-M	X47-M-CFRP1	X43-M-CFRP2	X44-M-CFRP3
Neutral Axis (mm)	-31.7	-37.95	114.5	119.7	124.5	126.9
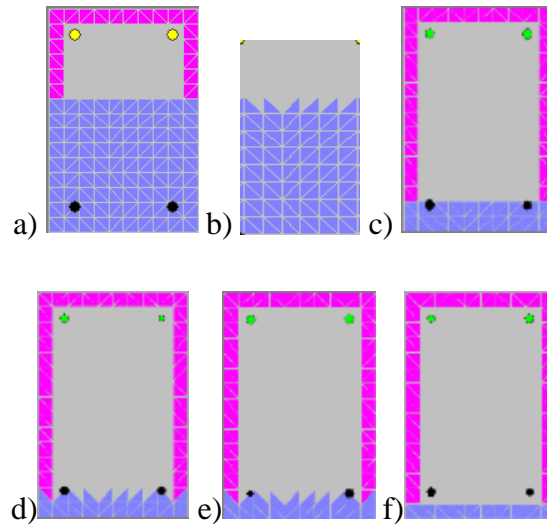
Figure 8.3 : Neutral axis and section of specimens at maximum moment load (a) X0-REF1, b) X26-REF2, c) X26-M, d) X47-M-CFRP1, e)X43-M-CFRP2, f)X44-M-CFRP3.

Energy dissipation capacities of the specimens, calculated as the area enclosed by the hysteresis loops is presented in Figure 8.4. As seen in the Figure 8.5, the energy dissipation capacity of the reference specimen, X0-REF1, is the lowest due to slip induced pinching. The energy dissipation capacity of the specimen X26-REF2 is higher than that of the specimens X0-REF1 and X26-M until 2% drift ratio, however the sudden failure of concrete and buckling of longitudinal bars at around 2% drift ratio prevented higher energy dissipation. Retrofitted specimens, X47-M-CFRP1, achieved the maximum hysteretic energy dissipation capacity due to wide hysteresis loops then followed by X43-M-CFRP2 and X44-M-CFRP3.
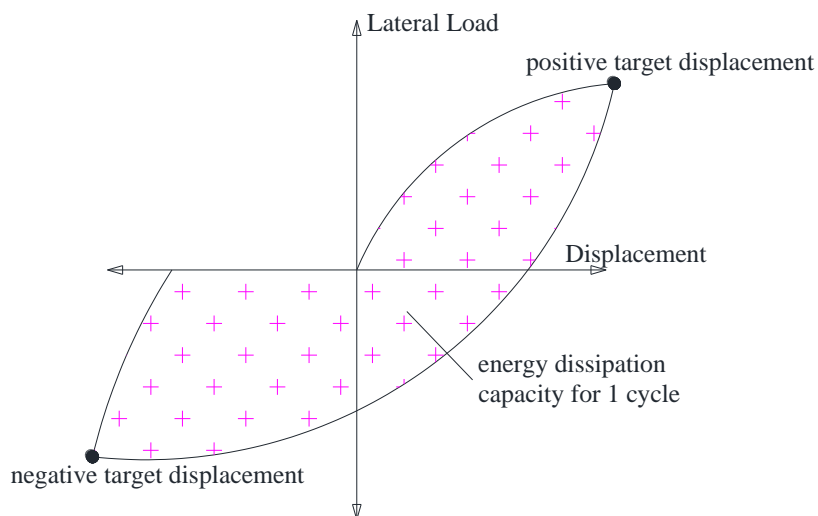
Figure 8.4 : Calculation of energy dissipation capacity.
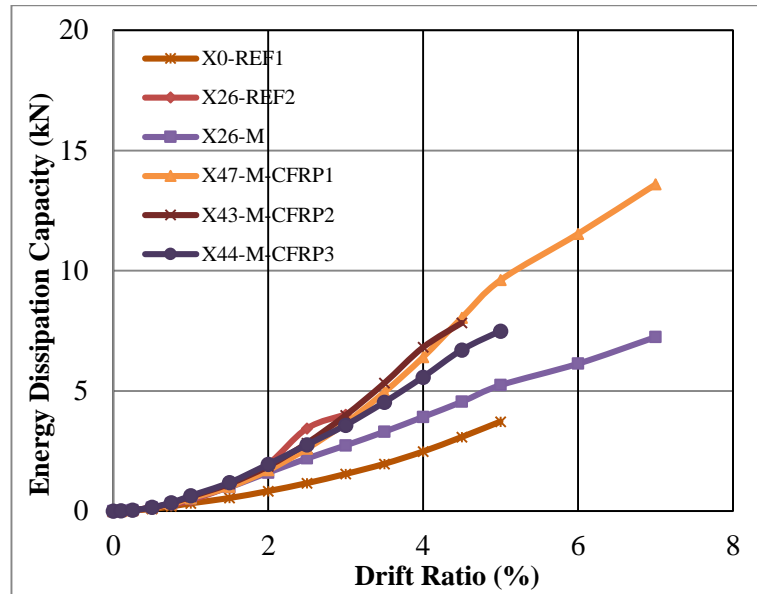
Figure 8.5 : Energy dissipation capacity of the specimens.

According to both energy dissipation capacities and autopsy pictures of the specimens, it can be said that X47-M-CFRP1 could not achieved the maximum hysteretic loads on Figure 8.1 and Figure 8.2 positive side due to local corrosion damage on the starter bars of this specimen.

The variation of ratios of residual plastic displacements (δres) to the displacements at which unloading began (δun) with respect to drift ratios are presented in Figure 8.6. As seen in this figure, δres/δun ratios for the specimen X26-REF2 are remarkably higher with respect to the specimen without corrosion, X0-REF1, and the specimens, which were rehabilitated/retrofitted, X26-M, X47-M-CFRP1, X43-M-CFRP2 and X44-M-CFRP3. It is also important to note that X44-M-CFRP3 has higher δres/δun ratio due to X26-REF2 until drift ratio 2% but, 2.5% drift ratio one of the starter bar of X44-M-CFRP3 ruptured and it prevented to residiual displacement at the end of the cycle. Relatively smaller (δres/δun) ratios obtained for X0-REF1 is attributed to the slip dominated behavior, whereas smaller residual displacements exhibited by the rehabilitated and retrofitted specimens can be explained through retarding of damage due to the contribution of repair mortar and CFRP confinement, respectively.
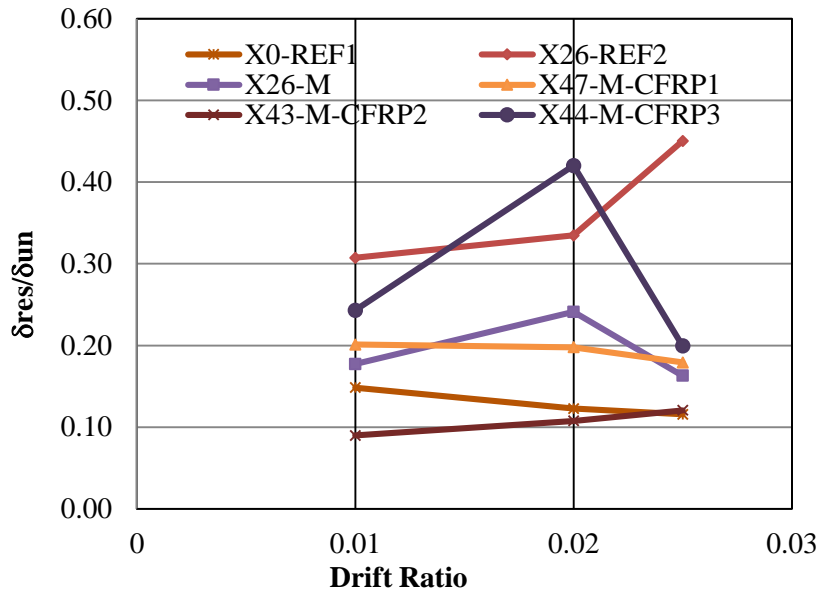
Figure 8.6 : The variation of residual displacement for the specimens.

a)

b)
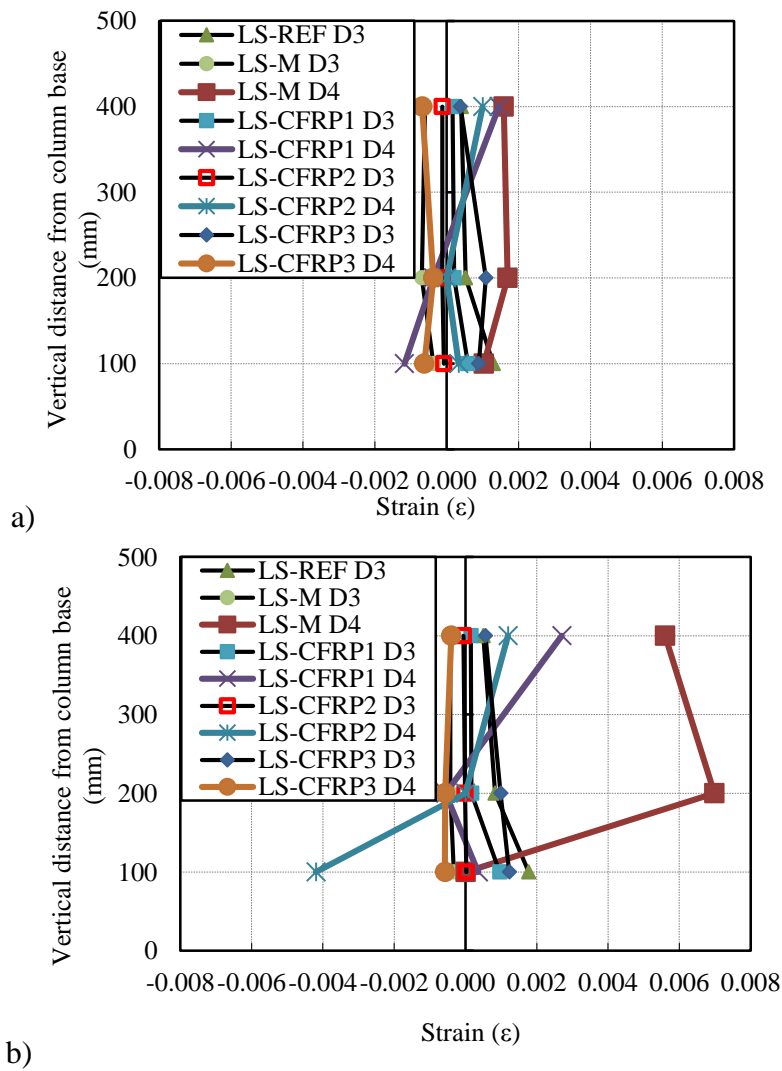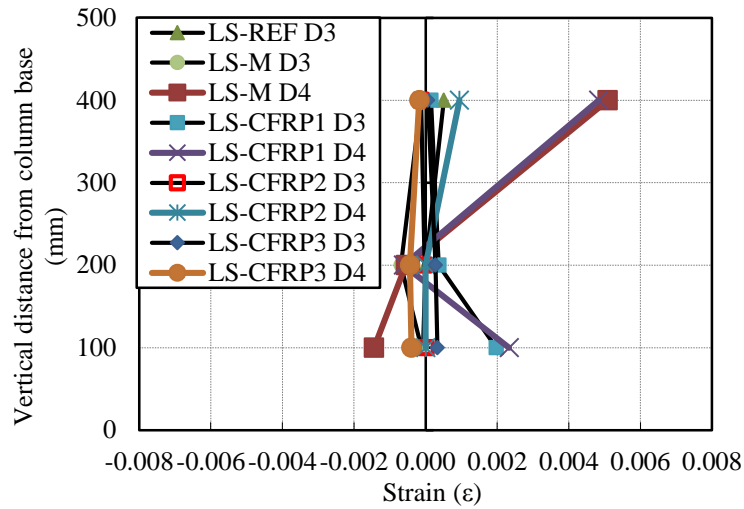
c)
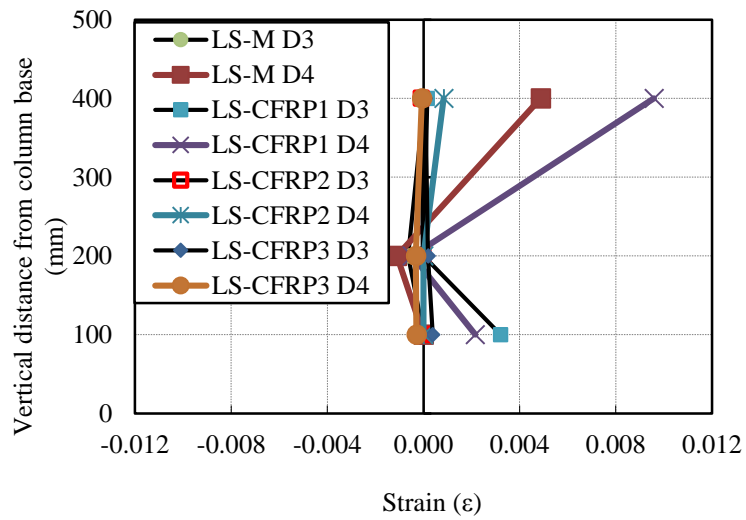
d)
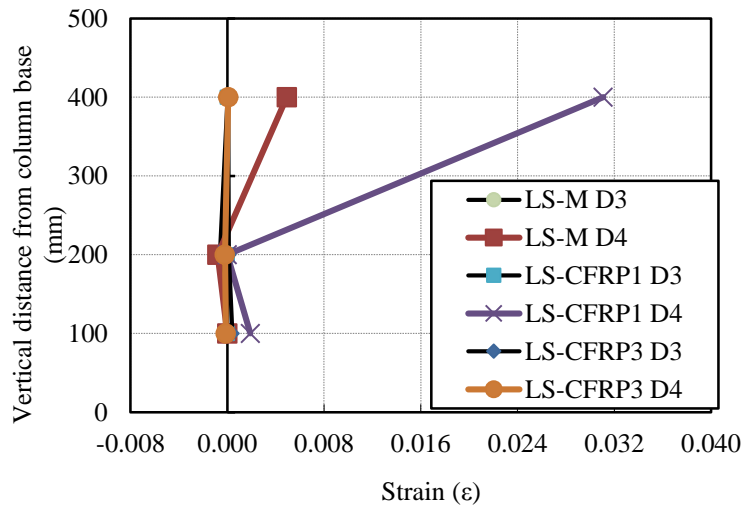
e)

Figure 8.7 : Strain distribution of starter reinforcement at a) 1%, b) 2%, c) 3% d)%4 e)%5 drift ratios.

The displacement ductility factor $\mu\delta$ is defined as the ratio between the ultimate displacement, δu and maximum displacement, δmax. The ultimate displacement is defined as the displacement corresponding to the displacement at which the applied load dropped to 85% of the maximum load. If the displacement ductility factors are compared which is given in Table 8.2, it can seen that the best displacement ductility is calculated in X0-REF1 and worst one is calculated in X26-REF2. Higher displacement ductility factors show that specimen can achieve higher displacement without a decrease in their strenght. However, ultimate displacement value for X0-REF1 is taken as 41.7 which is failure displacement of that specimen because 85% load drop of maximum load was not observed in test.

Table 8.2 : Displacement ductiliy of the specimens.

Specimens	Pmax (kN)	δmax (mm)	0.85×Pmax (kN)	δu (mm)	μδ
X0-REF1	16.29	8.66	13.85	41.7	4.82
X26-REF2	27.13	23.66	23.06	27.64	1.17
X26-M	31.23	20.05	26.54	31.15	1.55
X47-M-CFRP1	25.7	24.36	21.84	45.84	1.88
X43-M-CFRP2	33.56	18.54	28.53	45.45	2.45
X44-M-CFRP3	30.81	18.16	26.19	27.33	1.5

9. CONCLUSIONS AND RECOMMENDATIONS

Corrosion is a widespread problem of the existing buildings especially in Turkey which have built with substandard quality. A particular problem like as corrosion that there is no uniform results on experiments, it is needed to do tests for two or more specimens. However, it is too hard to achieve these experiments due to high costs and attribute of this study is considered as master degree thesis. For this reason, based on the results of limited number of reversed cyclic lateral loading tests on substandard RC columns with corroded plain reinforcing bars and extremely low strength concrete, the following conclusions/observations can be listed,

- The substandard columns built with extremely low quality concrete and plain reinforcing bars cannot reach their theoretical flexural capacity due to loss of bond between concrete and reinforcement. For this reason, the strength and displacement capacity of such columns are remarkably limited (X0-REF1).

- A certain level of corrosion causes increase of friction between the bars and concrete leading to better bond and enhanced strength. On the other hand, since the substandard columns were built with extremely low quality concrete and stirrups with large spacing between them, increased load resistance caused buckling of the longitudinal bars with a remarkable negative impact on drift capacity (X26-REF2).

- Rehabilitation of corrosion damaged column with repair mortar enhanced the strength of the damaged column significantly, whereas ductility was only slightly improved with respect to corrosion damaged column (X26-M with respect to X26-REF2).

- Rehabilitation and retrofitting using CFRP sheets enhanced both strength and ductility of the corrosion damaged column significantly up to a limit(X47-M-CFRP1 negative side with respect to X26-M).

- However, wrapping of substandard RC columns with corroded plain reinforcing bars and extremely low strength concrete with more than two layer of CRFP reduced ductility due to corroded reinforcement bar sections and elongation request of bars while equalizing the section stability(X26-M-REF2 with respect to others, X47-M-CFRP1 with respect to X43-M-CFRP2 and X44-M-CFRP3). It should be noted that

before any CFRP application, elongations of bars and statement of concrete should calculate carefully otherwise retrofitting with CFRP could also reduce both strength and ductility of substandard columns with corroded reinforcement due to rupture risk of corroded bars.

- Even CFRP increases both strength and ductility, local corrosion damages on the reinforcements can affect end reduce the behavior of specimen (X47-M-CFRP1 positive side).

Consequently, the presented rehabilitation/retrofitting technique is promising even for corrosion damaged substandard columns built with extremely low quality concrete. Considering the huge corrosion problem in Turkey for existing old structures which were built without complying the seismic codes, these findings are valuable for enhancing the seismic performance of these buildings. For further development, studies on different retrofit techniques utilizing different affordable materials and techniques can be carried out.

REFERENCES

ACI-222R (2001). Protection of metals in concrete against corrosion, *American Concrete Institute*, Detroit, USA.

ACI-318 (2011). Building Code Requirements for Structural Concrete and Commentary, *American Concrete Institute*, Detroit, USA.

ASTM-G15–04 (2004). Standard terminology relating to corrosion and corrosion testing, *The American Society for Testing and Materials*, Pennsylvania.

ASTM-G46–94 (1994). Standard guide for examination and evaluation of pitting corrosion, *The American Society for Testing and Materials*, Pennsylvania.

Bousias, S.N., Spathis, L.A., Triantafillou, T.C. and Fardis, M.N. (2002). "Seismic Retrofitting of Corrosion-Damaged RC Columns", 12th European Conference on Earthquake Engineering.

Demirtaş, B. (2008). Korozyonun Betonarme Kolonların Deprem Performansına Etkisi. İstanbul: Yüksek Lisans Tezi.

FEMA, (2007). Interim Testing Protocols for Determining the Seismic Performance Characteristics of Structural and Nonstructural Components, *Federal Emergency Management Agency*, Washington D.C..

Gedikli, Ü. (2004). Molibdenin sulu ortamdaki korozyonuna ph ve sülfürün etkisinin araştırılması, Yüksek Lisans Tezi, Ankara Üniversitesi Fen Bilimleri Enstitüsü, Ankara.

Gulikers, J. (2005). Theoretical considerations on the supposed linear relationship between concrete resistivity and corrosion rate of steel reinforcement. Materials and Corrosion, 56, No.6.

Göksu, Ç. (2012). The Effect of Corrosion on Reinforced Concrete Columns in regard of Seismic Performance, PhD. Thesis, Istanbul Technical University, Istanbul, Turkey.

İlki, A., Peker, Ö., Karamük, E., Demir, C., & Kumbasar, N. (2008). FRP Retrofit of Low and Medium Strength Circular and Rectangular Reinforced Concrete Columns. Journal of Materials In Civil Engineering © Asce, 169-188.

Lee, C. (1998). Accelerated Corosion and Repair of Reinforced Concrete Columns Using CFRP Sheets, Toronto, Canada. Master Degree Thesis.

Lee H., Kage T., Noguchi T., Tomosawa F. (2003). "An Experimental Study On The Retrofitting Effects of Reinforced Concrete Columns Damaged by Rebar Corrosion Strengthened with Carbon Fiber Sheets", Cement and Concrete Research 33 563-570.

Maaddawy, T.E. (2008). "Behavior Of Corrosion-Damaged RC Columns Wrapped With FRP Under Combined Flexural And Axial Loading", UAE University.

Mander J. B., Priestley M. J. N., Park R. (1988). "Theoretical Stress-Strain Model For Confined Concrete", ASCE Journal of Structural Engineering 114(8) 1804-1826.

Pantazopoulou S. J., Bonacci J. F., Sheikh S., Thomas M. D. A. and Hearn N. (2001). "Repair of corrosion damaged columns with FRP wraps", ASCE Journal of Composites for Construction 5(1) 3-11.

Sezen, H., and Moehle, J.P. (2004). Shear Strength Model for Lightly Reinforced Concrete Columns, *ASCE Journal of Structural Engineering,* Vol. **130**, no.11, pp. 1692-1703

Soudki K., El-Salakawy E., Craig B. (2007) ."Behavior of CFRP strengthened reinforced concrete beams in corrosive environment", ASCE Journal of Composites for Construction 11(3) 291-298.

Tastani, S., & Pantazopoulou, S. (2004). Experimental evaluation of FRP jackets in upgrading RC corroded columns with substandard detailing. Engineering Structures, 26, 817-829.

TS500 (2000). Requirements for design and construction of reinforced concrete structures, *Turkish Standards Institute*, Ankara, Turkey.

Wang C.Y., Shih, C.C., Hong S.C., and Hwang, W.C. (2004). Rehabilitation of Cracked and Corroded Reinforced Concrete Beams with Fiber-Reinforced Plastic Patches. *Journal of Composites for Construction*,Vol. 8, no. 3.

XTRACT 3.0.8 (2007). Cross-sectional structural analysis of components.

Url-1 <http://www.cement.org, >, date retrieved 25.12.2012.

Url-2 <http://www.corrosionclinic.com, >, date retrieved 18.12.2012.

Url-3 <http://www.lvdt.co.uk, >, date retrieved 14.12.2012.

APPENDICES

APPENDIX A: Reinforcing cage of specimens.
APPENDIX B: The views of specimens.
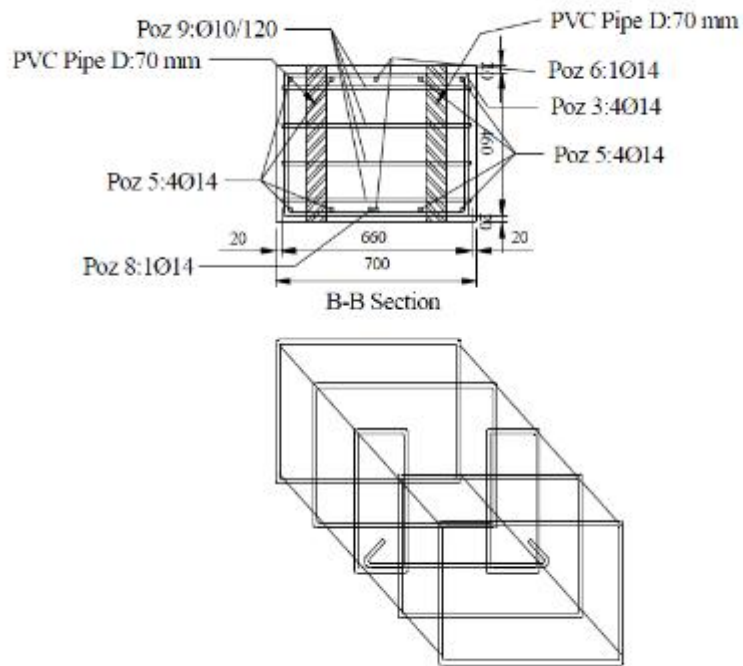
Figure A.1 : Reinforcing cage of the first type specimens (south side).
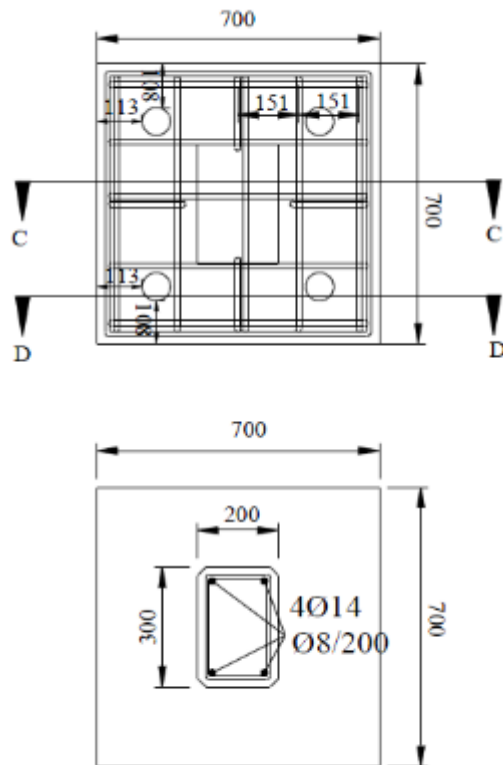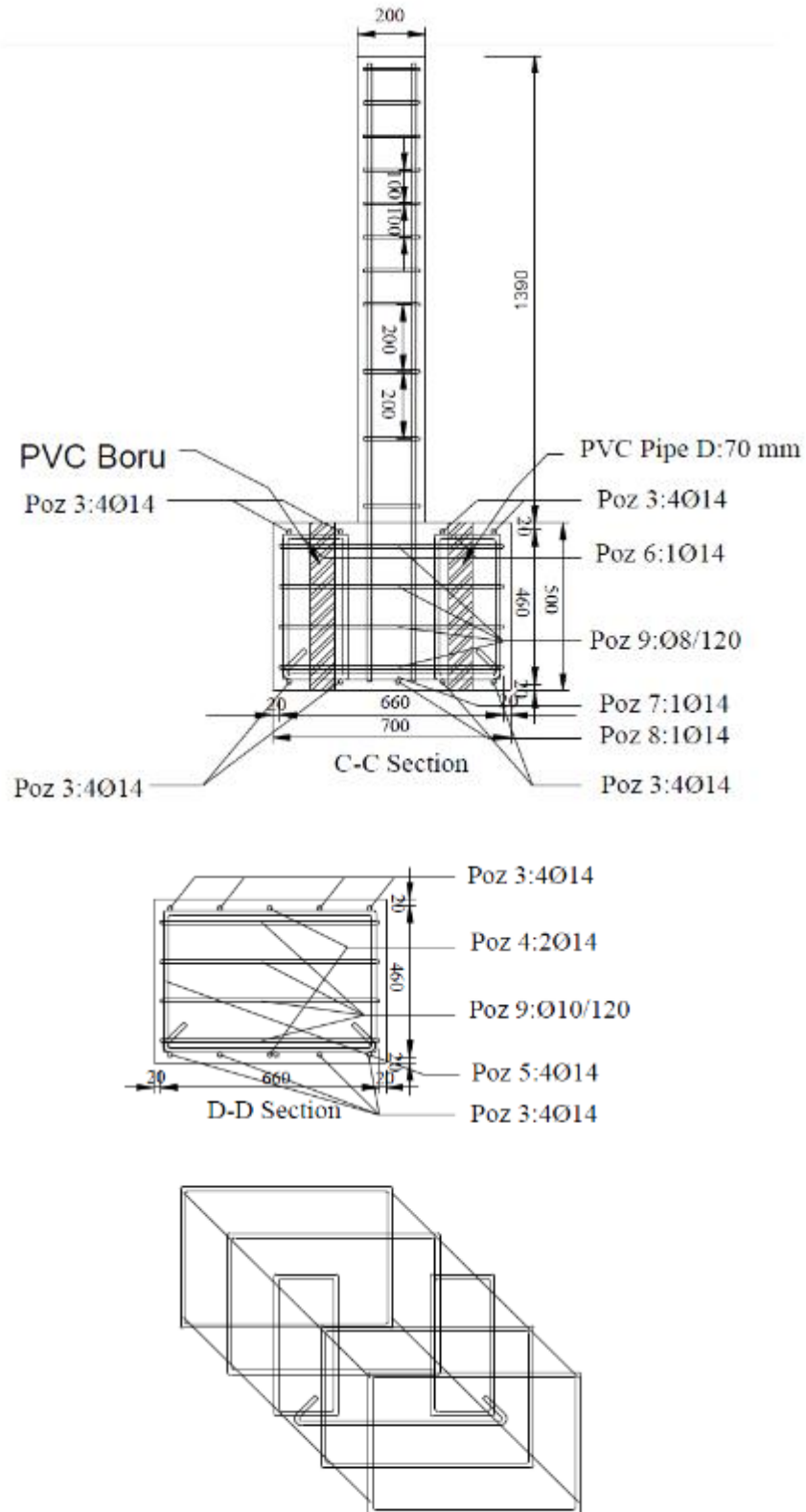
Figure A.2 : Reinforcing cage of the first type specimens(south side).
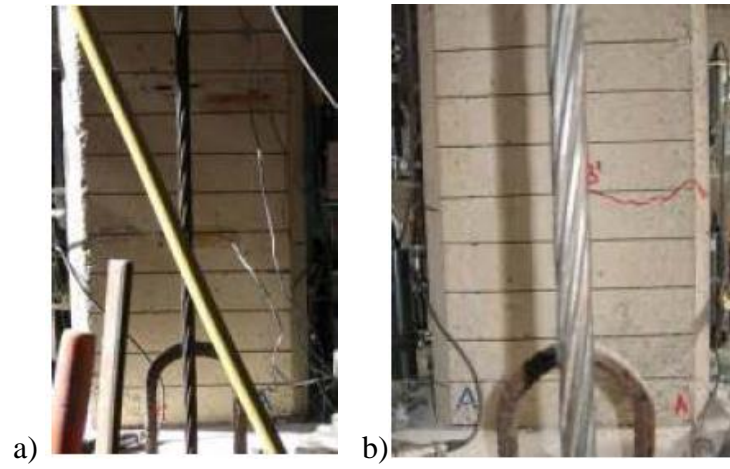
Figure B.1 : a) North, and b) South view of X0-REF1 after -0.50% mm drift ratio.
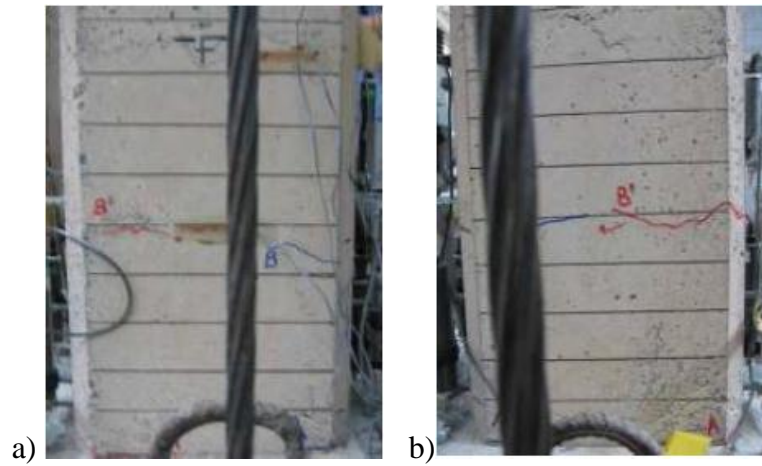
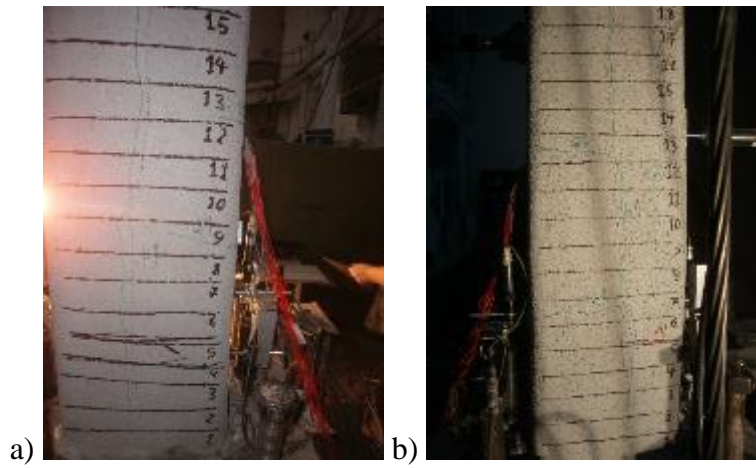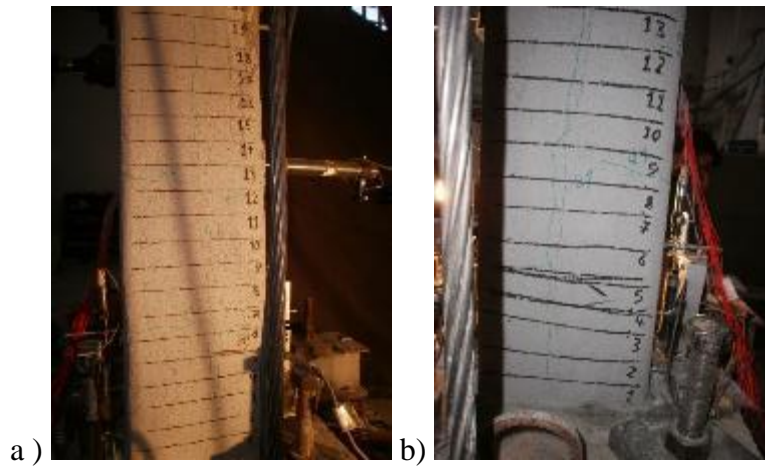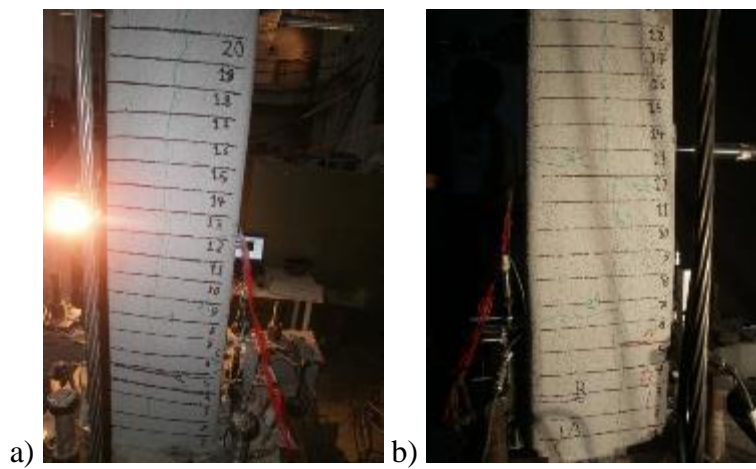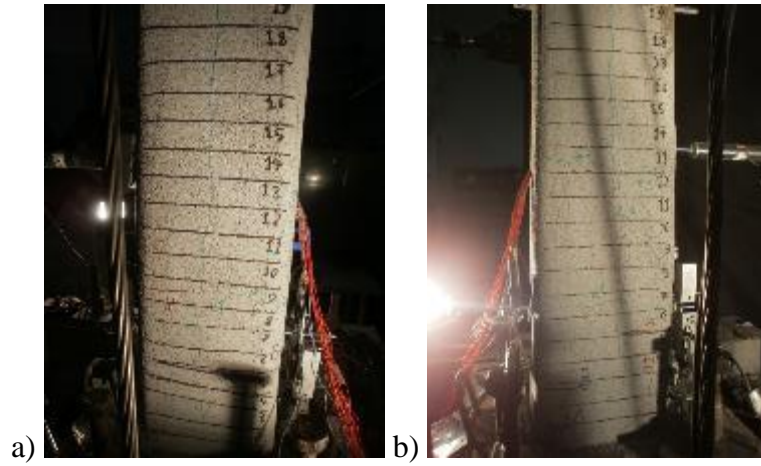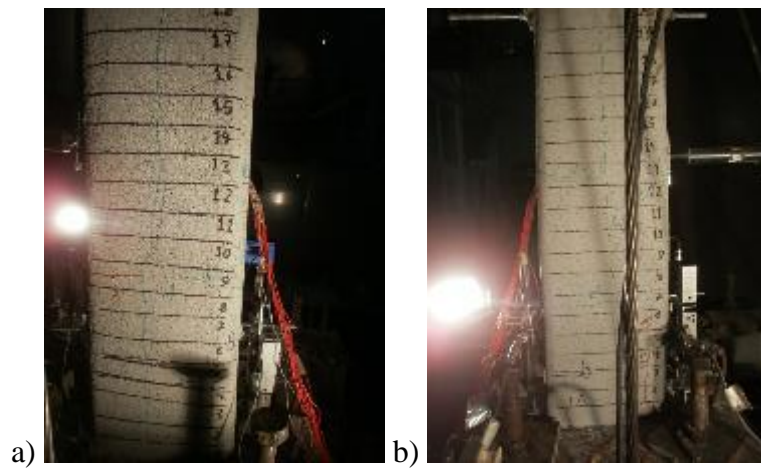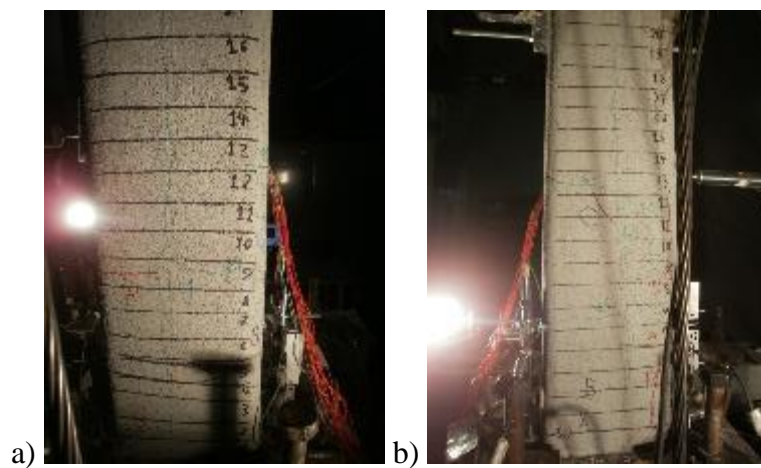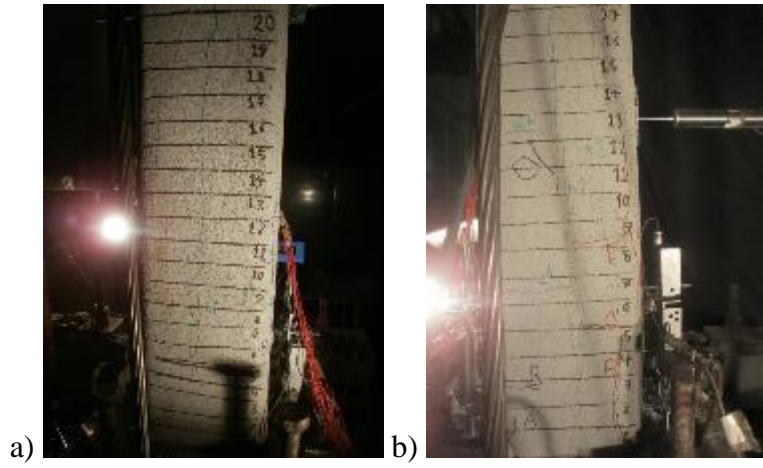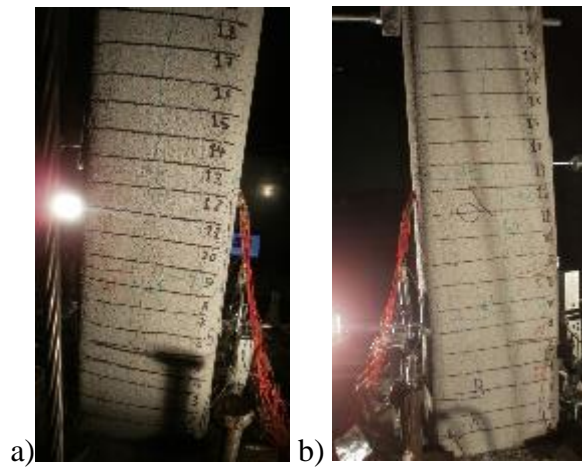**Figure B.2 :** a) North, and b) South view of X0-REF1 after -0.75% mm drift ratio.
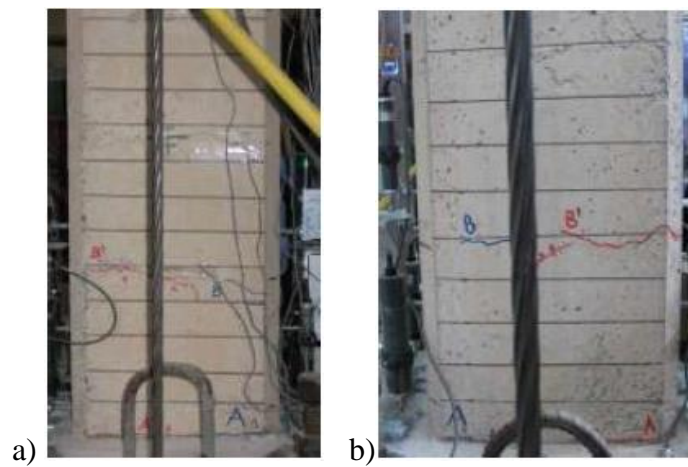
Figure B.3 : a) North, and b) South view of X0-REF1 after -1.00% mm drift ratio.
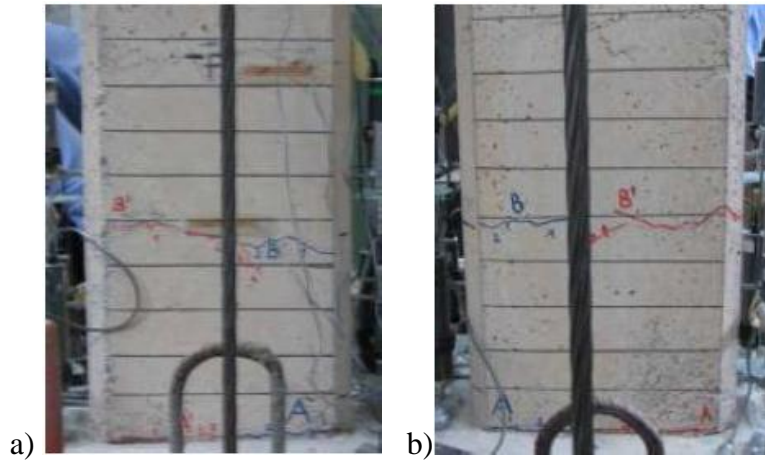
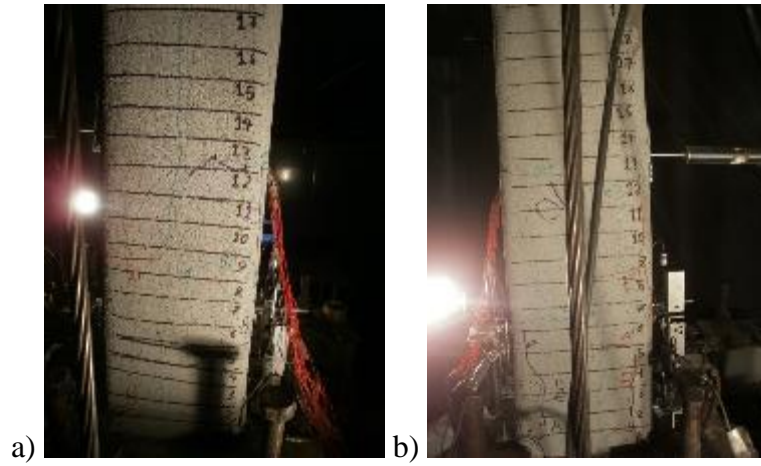**Figure B.4 :** a) North, and b) South view of X0-REF1 after -1.50% mm drift ratio.
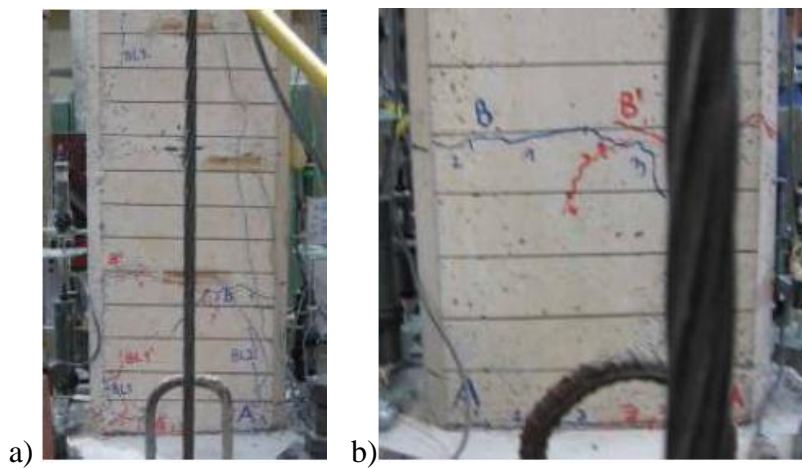
Figure B.5 : a) North, and b) South view of X0-REF1 after -2.00% mm drift ratio.
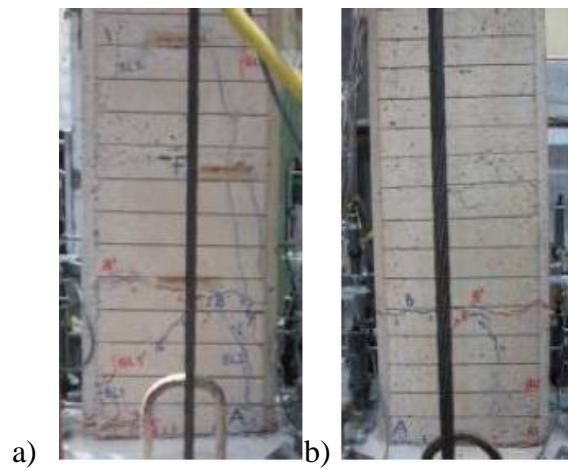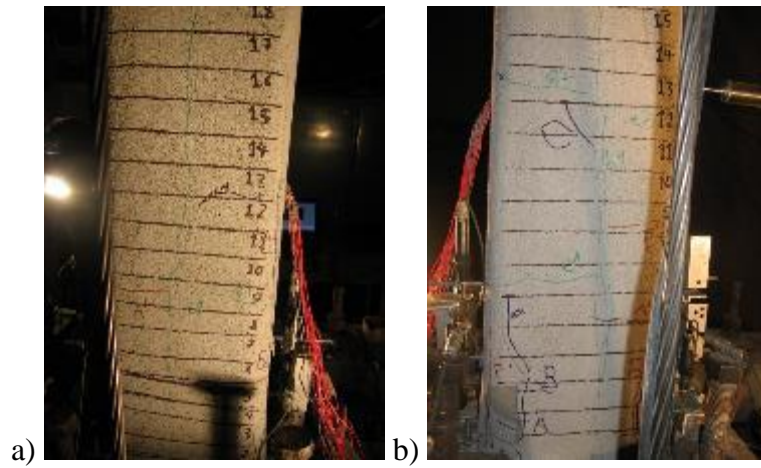

Figure B.6 : a) North, and b) South view of X0-REF1 after -2.50% mm drift ratio.
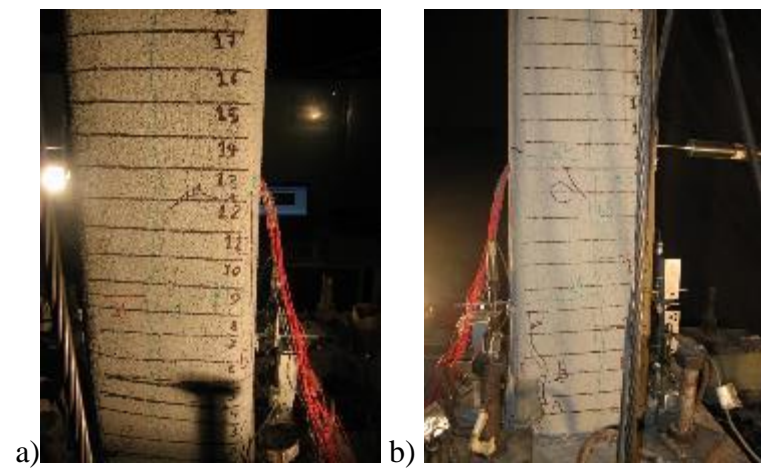
b)
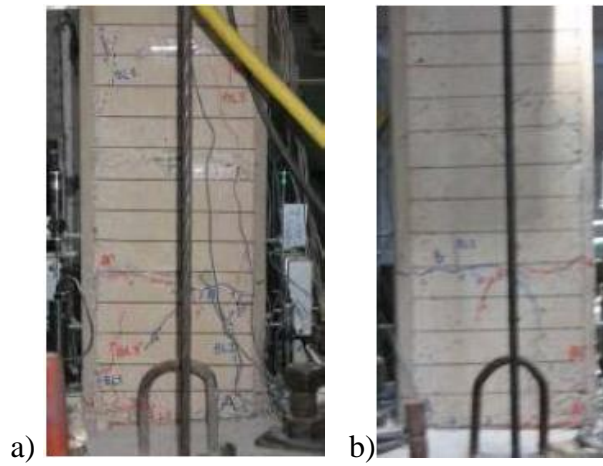
Figure B.7 : a) North, and b) South view of X0-REF1 after -3.00% mm drift ratio.
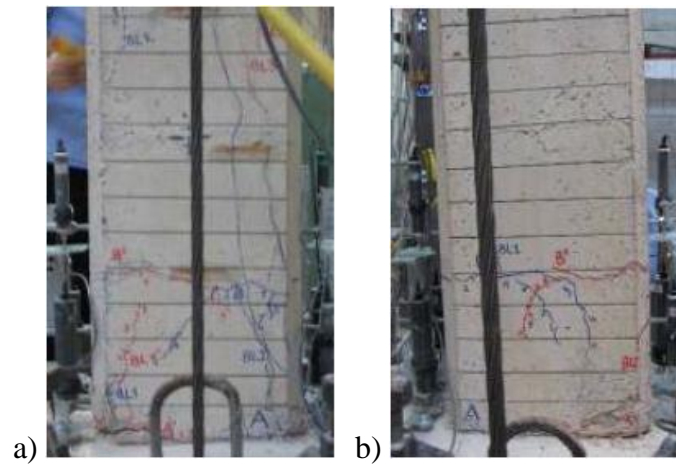
Figure B.8 : a) North, and b) South view of X0-REF1 after -3.50% mm drift ratio.
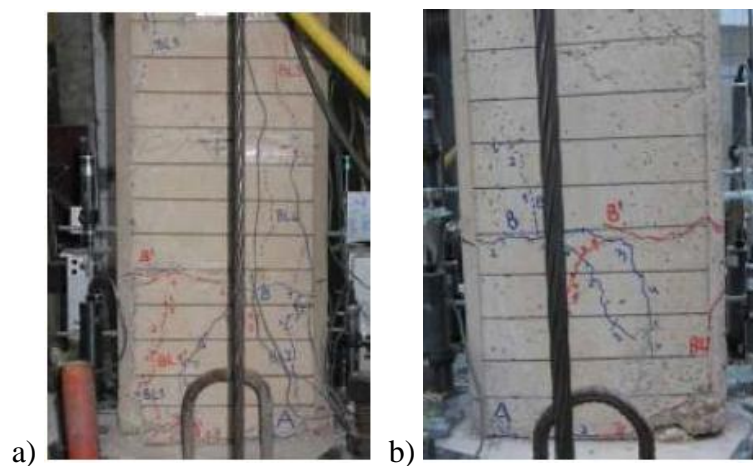
Figure B.9 : a) North, and b) South view of X0-REF1 after -4.00% mm drift ratio.
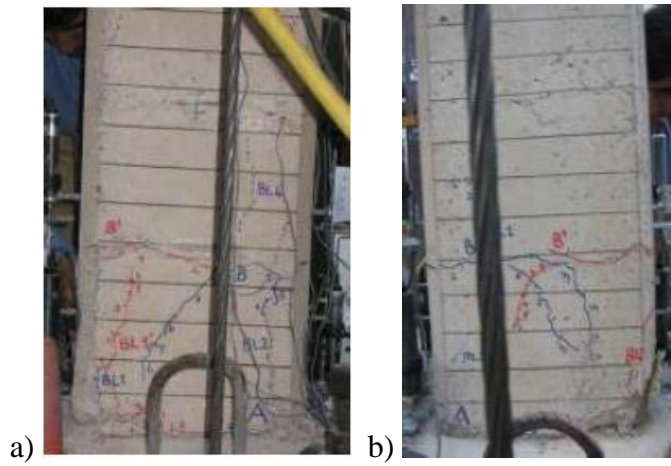
Figure B.10 : a) North, and b) South view of X0-REF1 after -4.50% mm drift ratio.
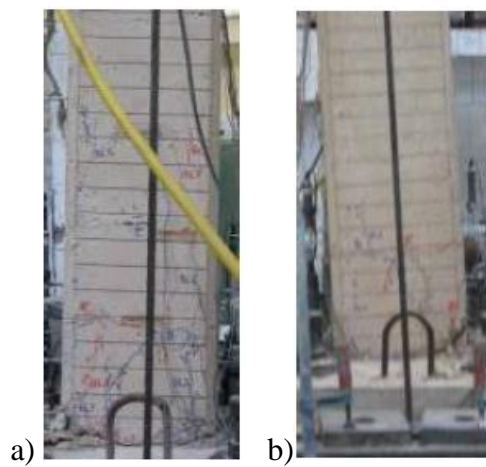
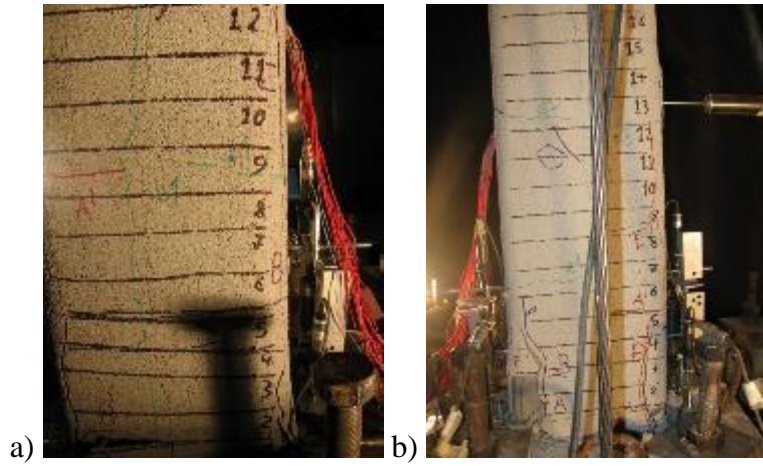**Figure B.11 :** a) North, and b) South view of X0-REF1 after -5.00% mm drift ratio.

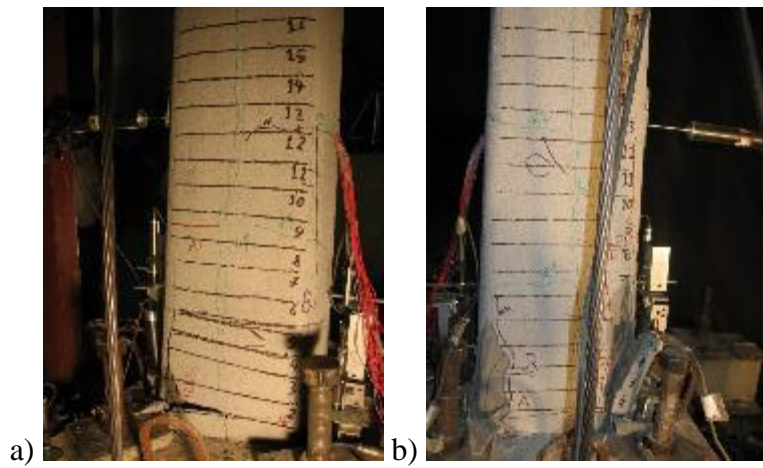**Figure B.12 :** a) North, and b) South view of X26-REF2 after -0.25% mm drift ratio.
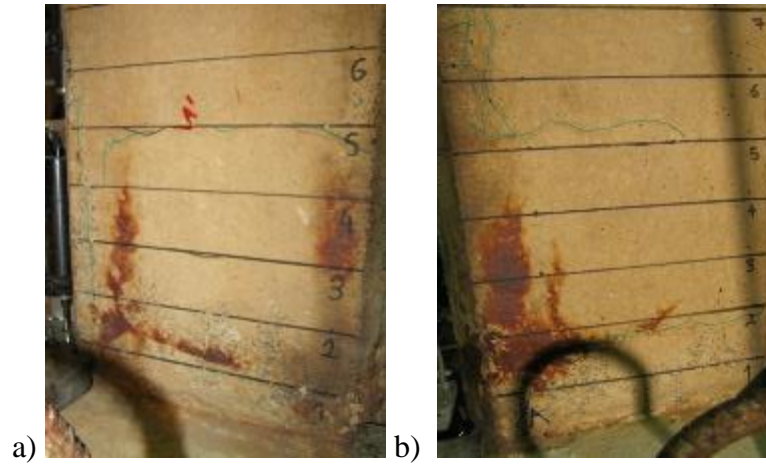
Figure B.13 : a) North, and b) South view of X26-REF2 after -0.5% mm drift ratio.
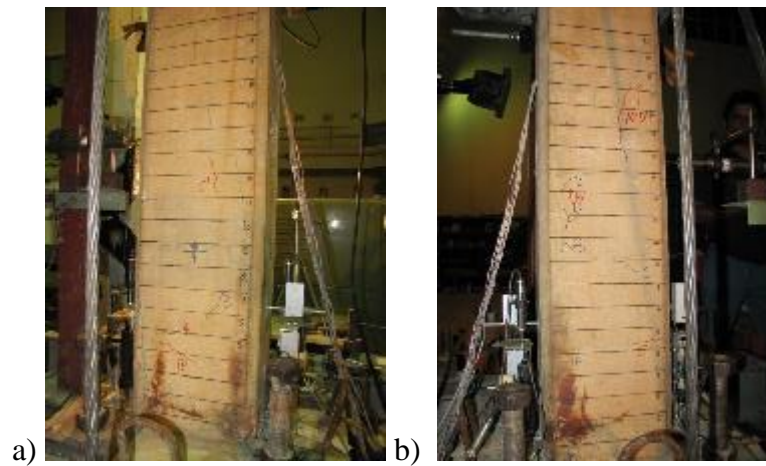
Figure B.14 : a) North, and b) South view of X26-REF2 after -0.75 % mm drift ratio.
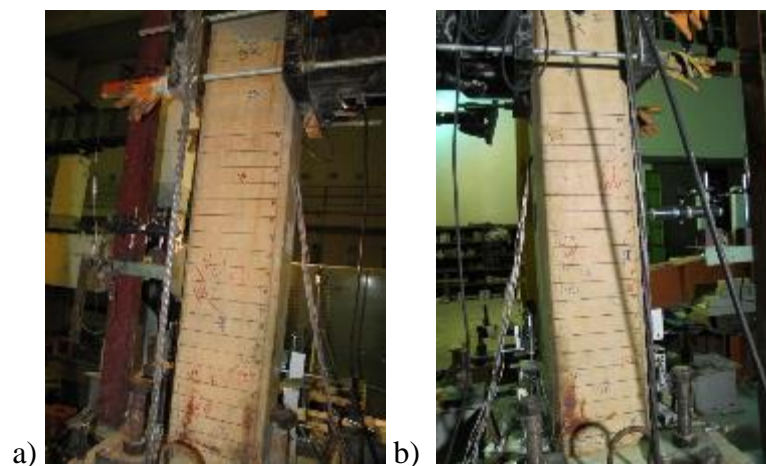
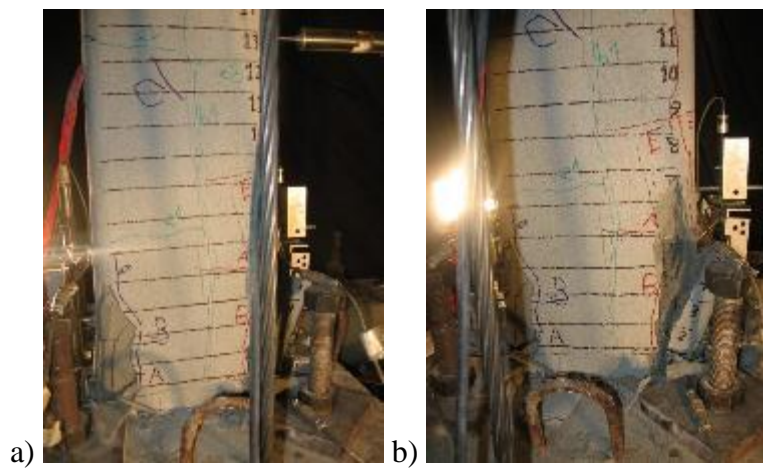**Figure B.15 :** a) North, and b) South view of X26-REF2 after -1.00 % mm drift ratio.

Figure B.16 : a) North, and b) South view of X26-REF2 after -1.50 % mm drift ratio.
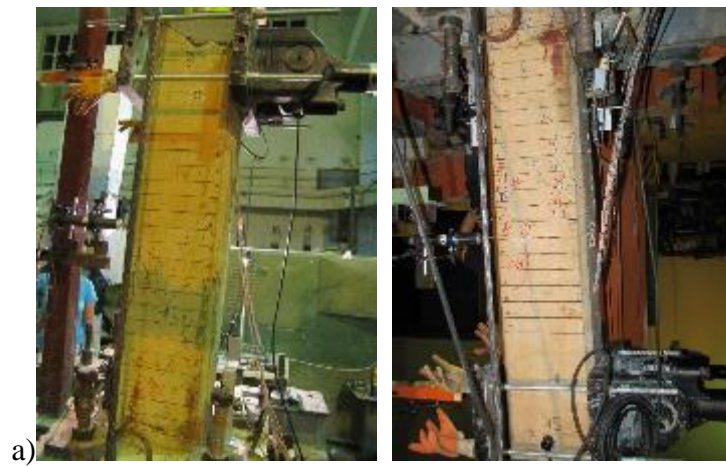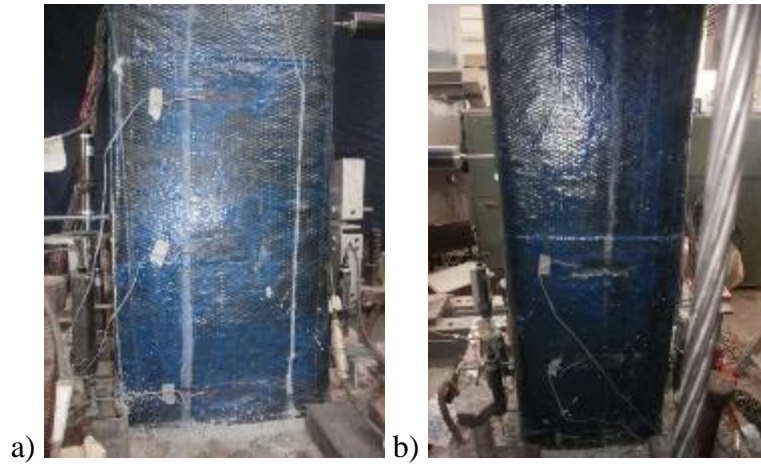

Figure B.17 : a) North, and b) South view of X26-REF2 after -2.00 % mm drift ratio.
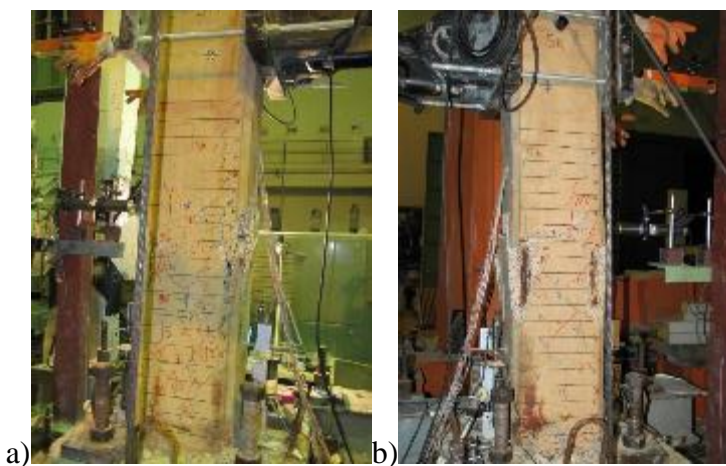
Figure B.18 : a) North, and b) South view of X26-REF2 after -2.50 % mm drift ratio.

Figure B.19 : a) North, and b) South view of X26-REF2 after -3.00 % mm drift ratio.
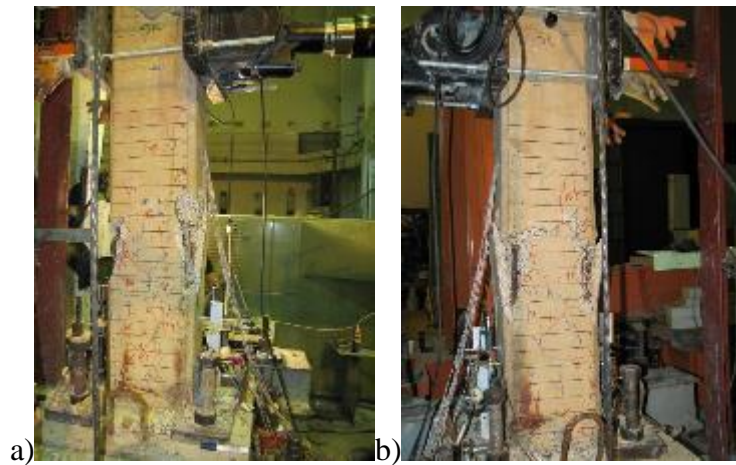
Figure B.20 : a) North, and b) South view of X26-REF2 after -3.50 % mm drift ratio.
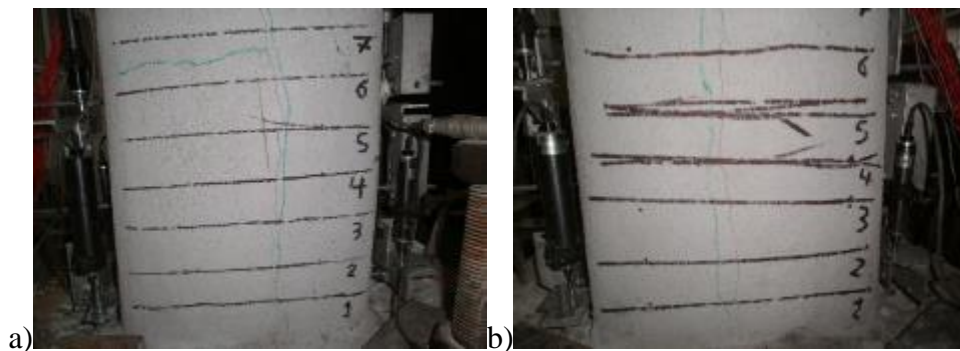
Figure B.21 : a) North, and b) South view of X26-M after -0.10 % mm drift ratio.

Figure B.22 : a) North, and b) South view of X26-M after -0.25 % mm drift ratio.

Figure B.23 : a) North, and b) South view of X26-M after -0.50 % mm drift ratio.

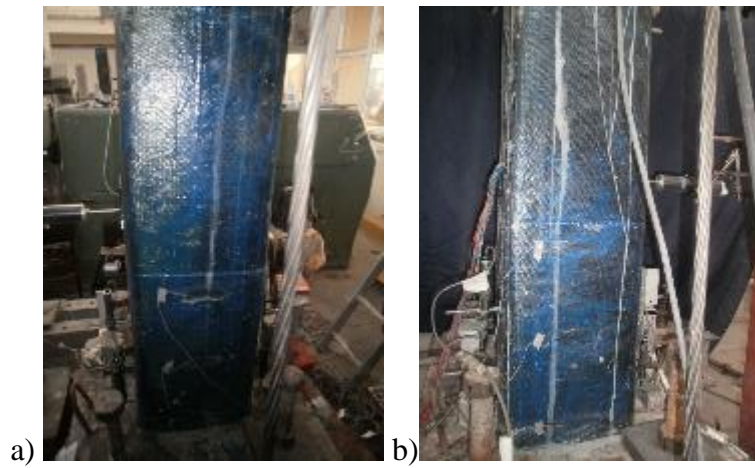**Figure B.24 :** a) North, and b) South view of X26-M after -0.75 % mm drift ratio.

Figure B.25 : a) North, and b) South view of X26-M after -1.00 % mm drift ratio.

Figure B.26 : a) North, and b) South view of X26-M after -1.50 % mm drift ratio.

Figure B.27 : a) North, and b) South view of X26-M after -2.00 % mm drift ratio.

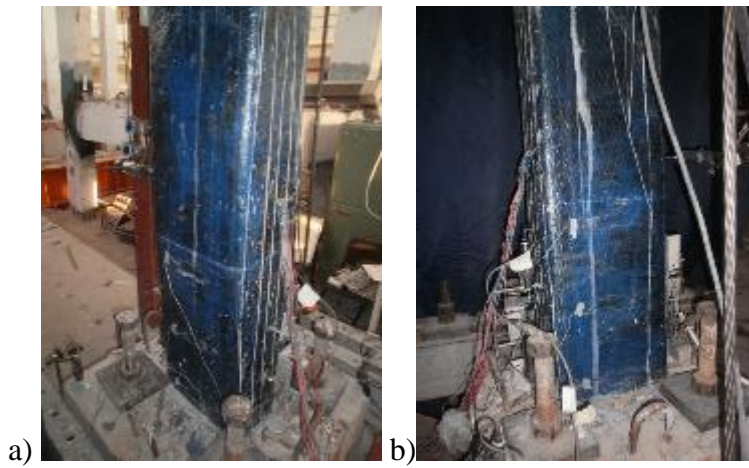**Figure B.28 :** a) North, and b) South view of X26-M after -2.50 % mm drift ratio.

Figure B.29 : a) North, and b) South view of X26-M after -3.00 % mm drift ratio.

Figure B.30 : a) North, and b) South view of X26-M after -3.50 % mm drift ratio.

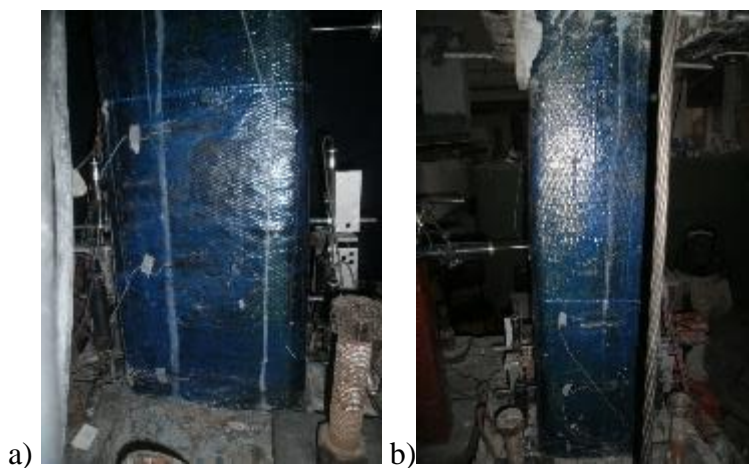**Figure B.31 :** a) North, and b) South view of X26-M after -4.00 % mm drift ratio.

Figure B.32 : a) North, and b) South view of X26-M after -4.50 % mm drift ratio.

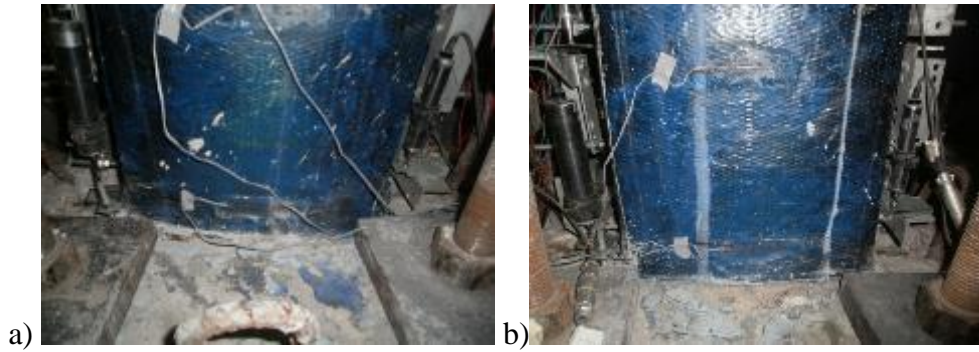**Figure B.33 :** a) North, and b) South view of X26-M after -5.00 % mm drift ratio.

Figure B.34 : a) North, and b) South view of X26-M after -6.00 % mm drift ratio.

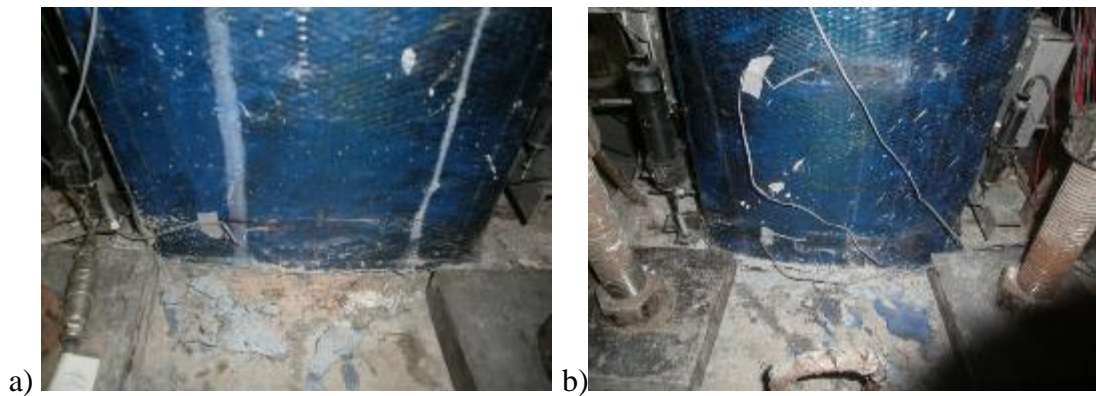**Figure B.35 :** a) North, and b) South view of X26-M after -7.00 % mm drift ratio.

Figure B.36 : a) North, and b) South view of X26-M after the test finished.

Figure B.37 : a) North, and b) South view of X26-M-CFRP1 after -0.10% mm drift ratio.

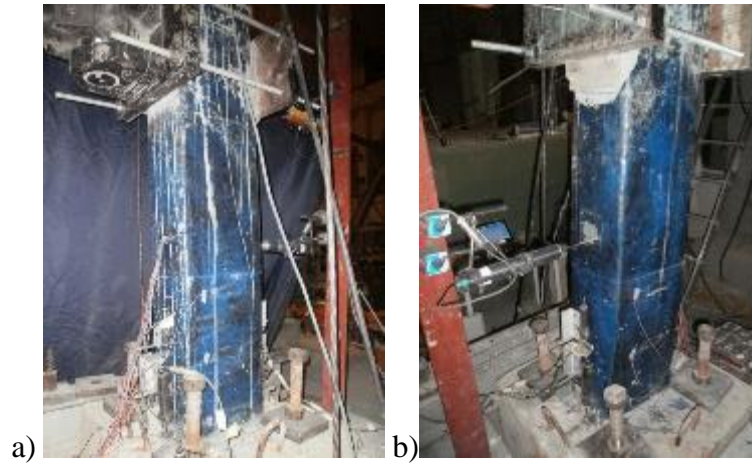**Figure B.38 :** a) North, and b) South view of X26-M-CFRP1 after -0.25% mm drift ratio.

Figure B.39 : a) North, and b) South view of X26-M-CFRP1 after -0.5% mm drift ratio.

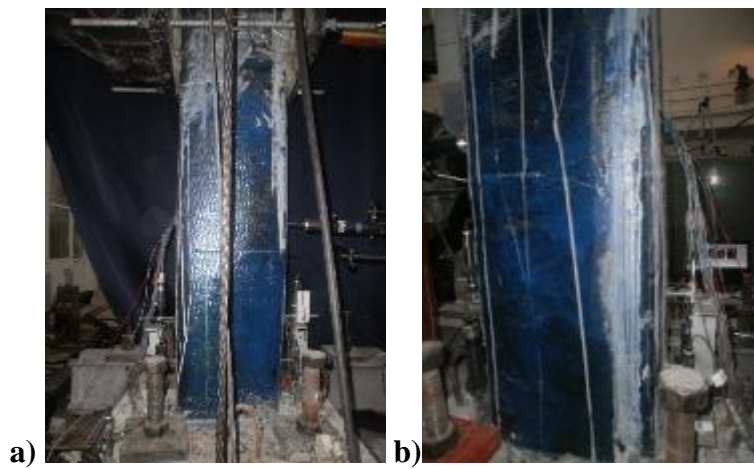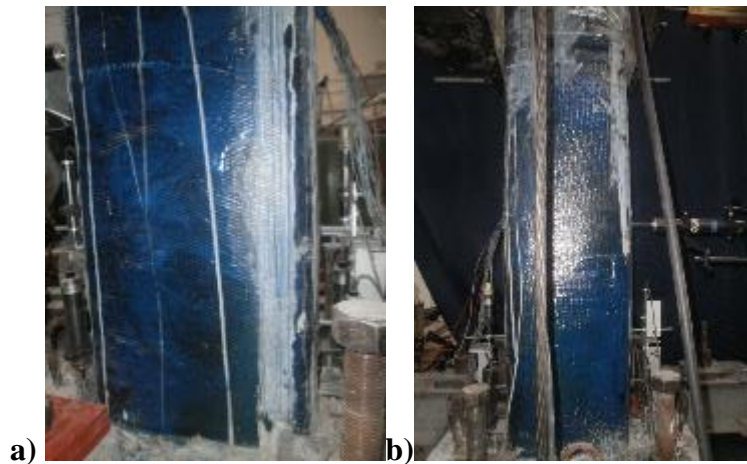**Figure B.40 :** a) North, and b) South view of X26-M-CFRP1 after -0.75% mm drift ratio.

Figure B.41 : a) North, and b) South view of X26-M-CFRP1 after -1.00% mm drift ratio.

Figure B.42 : a) North, and b) South view of X26-M-CFRP1 after -1.50% mm drift ratio.

Figure B.43 : a) North, and b) South view of X26-M-CFRP1 after -2.00% mm drift ratio.

Figure B.44 : a) North, and b) South view of X26-M-CFRP1 after -2.50% mm drift ratio.

Figure B.45 : a) North, and b) South view of X26-M-CFRP1 after -3.00% mm drift ratio.
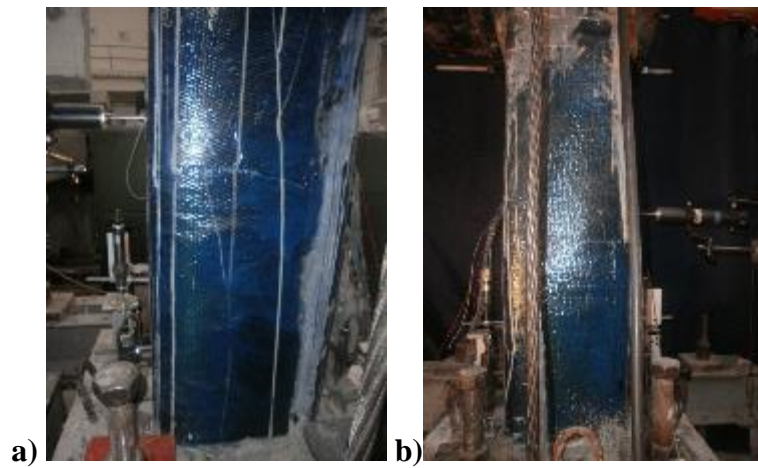
Figure B.46 : a) North, and b) South view of X26-M-CFRP1 after -3.50% mm drift ratio.
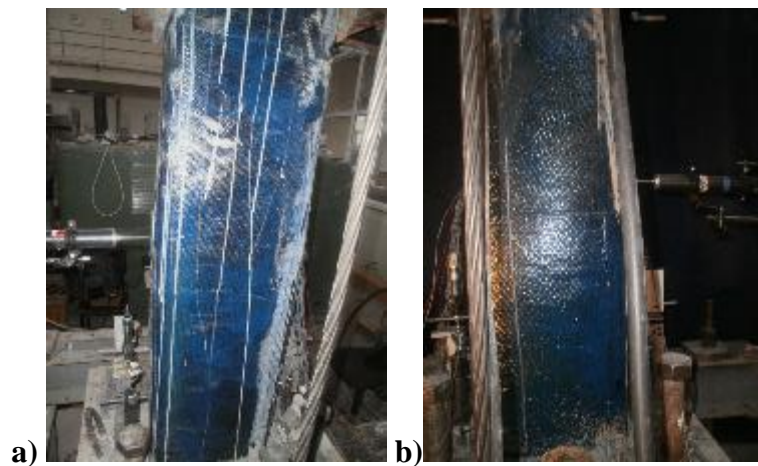

Figure B.47 : a) North, and b) South view of X26-M-CFRP1 after -4.00% mm drift ratio.

Figure B.48 : a) North, and b) South view of X26-M-CFRP1 after -5.00% mm drift ratio.

Figure B.49 : a) North, and b) South view of X26-M-CFRP1 after -5.00% mm drift ratio.

Figure B.50 : a) North, and b) South view of X26-M-CFRP1 after -6.00% mm drift ratio.
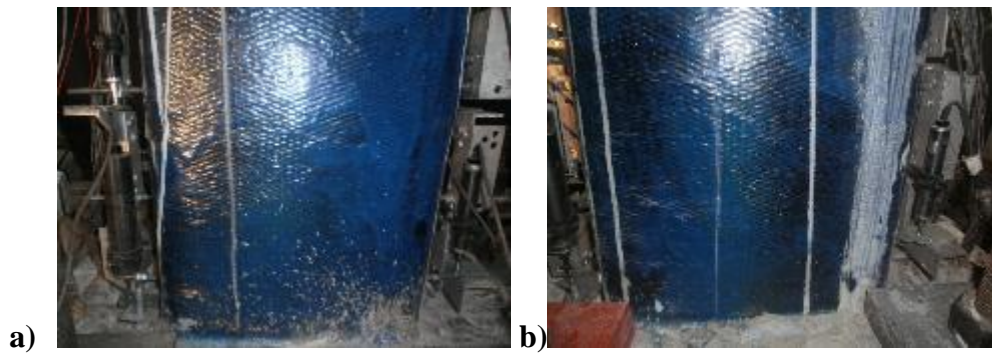

Figure B.51 : a) North, and b) South view of X26-M-CFRP1 after -7.00% mm drift ratio.

Figure B.52 : a) North, and b) South view of X26-M-CFRP1 after test finished.

Figure B.53 : a) North, and b) South view of X43-M-CFRP2 after -0.10% mm drift ratio.

Figure B.54 : a) North, and b) South view of X43-M-CFRP2 after -0.25% mm drift ratio.

Figure B.55 : a) North, and b) South view of X43-M-CFRP2 after -0.5% mm drift ratio.

Figure B.56 : a) North, and b) South view of X43-M-CFRP2 after -0.75% mm drift ratio.
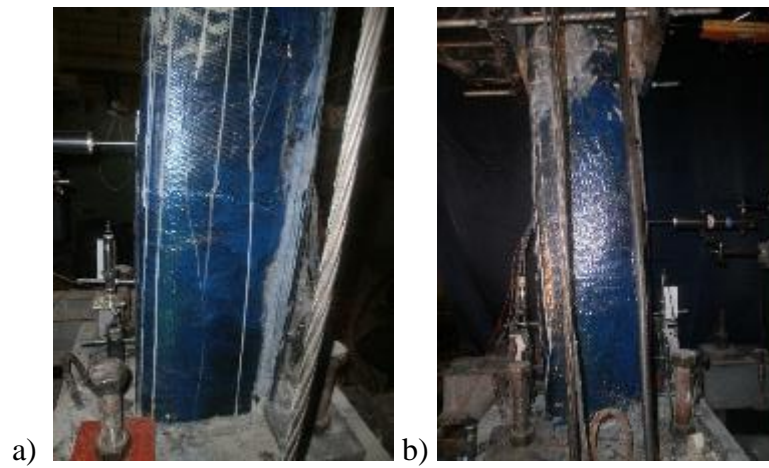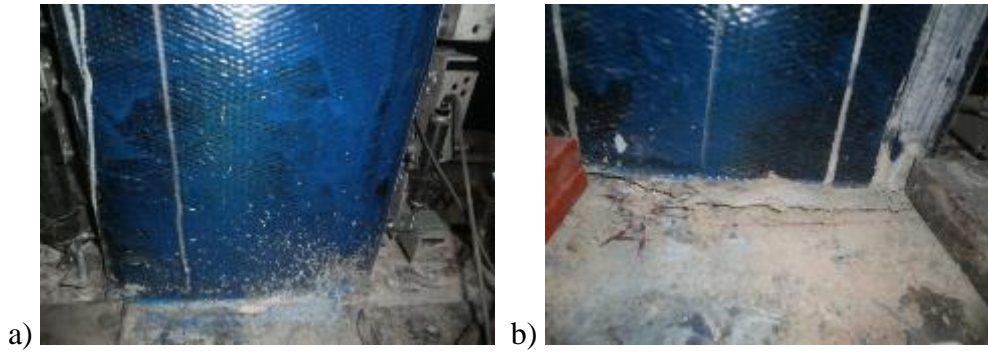

Figure B.57 : a) North, and b) South view of X43-M-CFRP2 after -1.00% mm drift ratio.

Figure B.58 : a) North, and b) South view of X43-M-CFRP2 after -1.50% mm drift ratio.

Figure B.59 : a) North, and b) South view of X43-M-CFRP2 after -2.00% mm drift ratio.

Figure B.60 : a) North, and b) South view of X43-M-CFRP2 after -2.50% mm drift ratio.
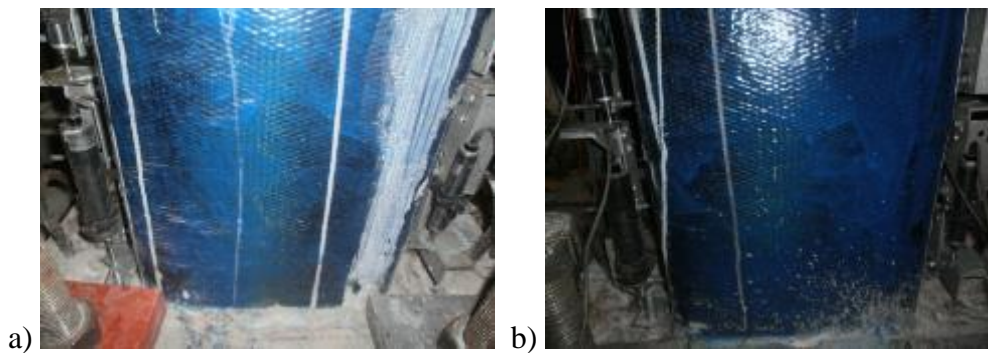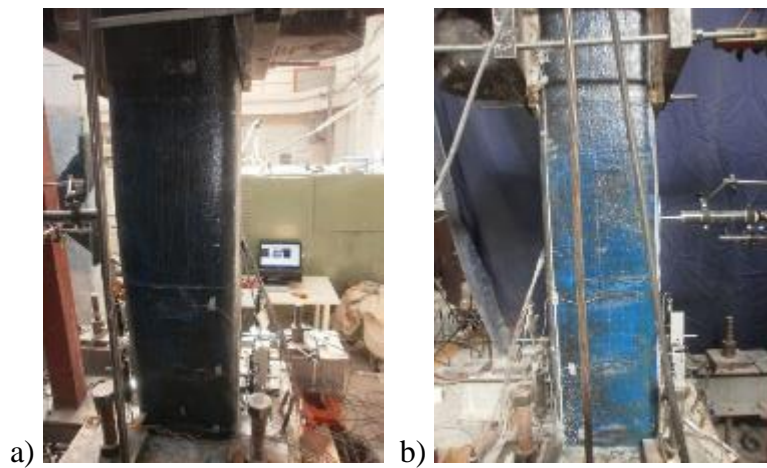
Figure B.61 : a) North, and b) South view of X43-M-CFRP2 after -3.00% mm drift ratio.

Figure B.62 : a) North, and b) South view of X43-M-CFRP2 after -3.50% mm drift ratio.

Figure B.63 : a) North, and b) South view of X43-M-CFRP2 after -4.00% mm drift ratio.

Figure B.64 : a) North, and b) South view of X43-M-CFRP2 after -5.00% mm drift
ratio.

Figure B.65 : a) North, and b) South view of X43-M-CFRP2 after test finished.

Figure B.66 : a) North, and b) South view of X44-M-CFRP3 after -0.10% mm drift
ratio.

Figure B.67 : a) North, and b) South view of X44-M-CFRP3 after -0.25% mm drift ratio.

Figure B.68 : a) North, and b) South view of X44-M-CFRP3 after -0.5% mm drift ratio.

Figure B.69 : a) North, and b) South view of X44-M-CFRP3 after -0.75% mm drift ratio.
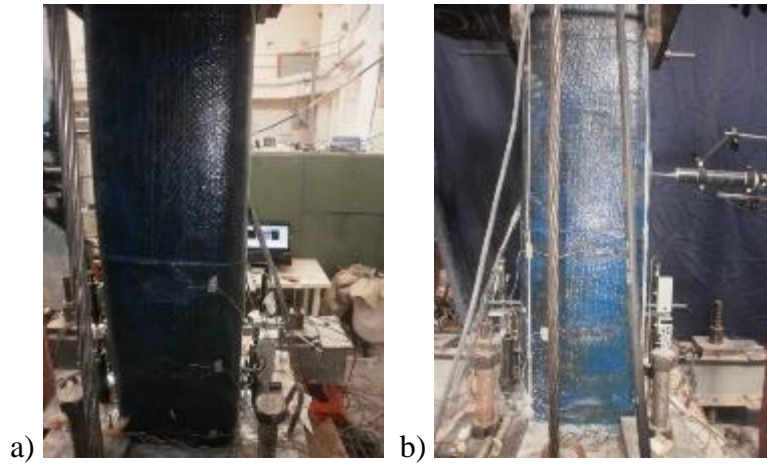
Figure B.70 : a) North, and b) South view of X44-M-CFRP3 after -1.00% mm drift ratio.
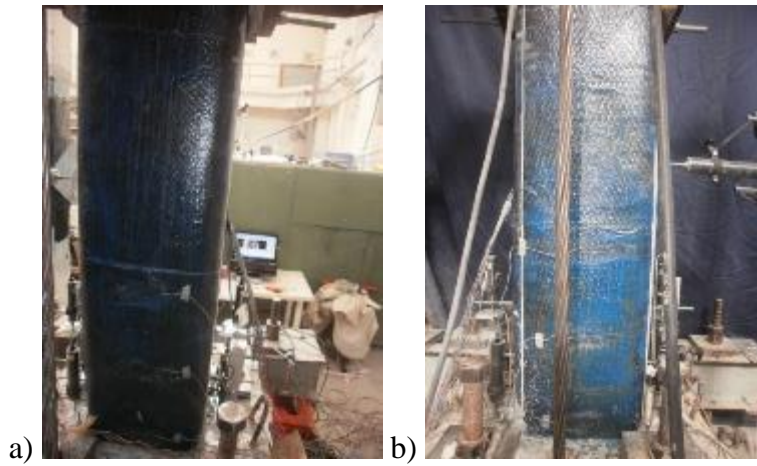

Figure B.71 : a) North, and b) South view of X44-M-CFRP3 after -1.50% mm drift ratio.

Figure B.72 : a) North, and b) South view of X44-M-CFRP3 after -2.00% mm drift ratio.
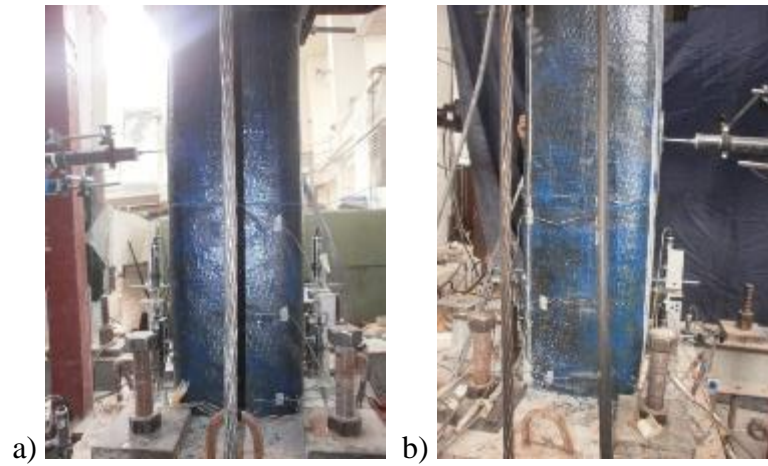
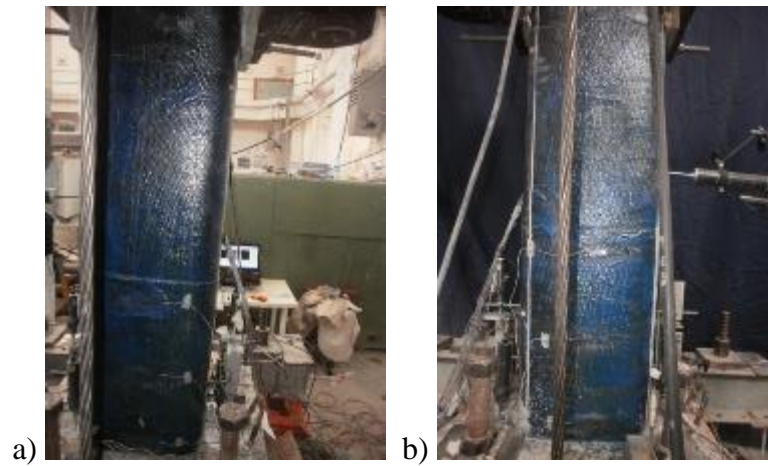**Figure B.73 :** a) North, and b) South view of X44-M-CFRP3 after -2.50% mm drift ratio.

Figure B.74 : a) North, and b) South view of X44-M-CFRP3 after -3.00% mm drift ratio.
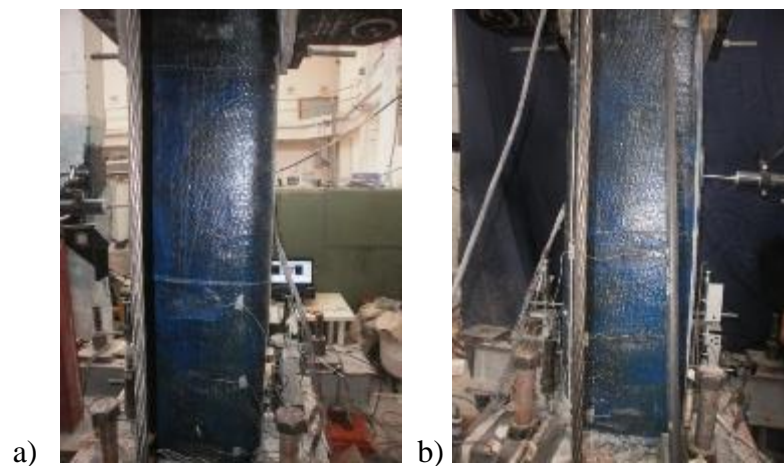

Figure B.75 : a) North, and b) South view of X44-M-CFRP3 after -3.50% mm drift ratio.
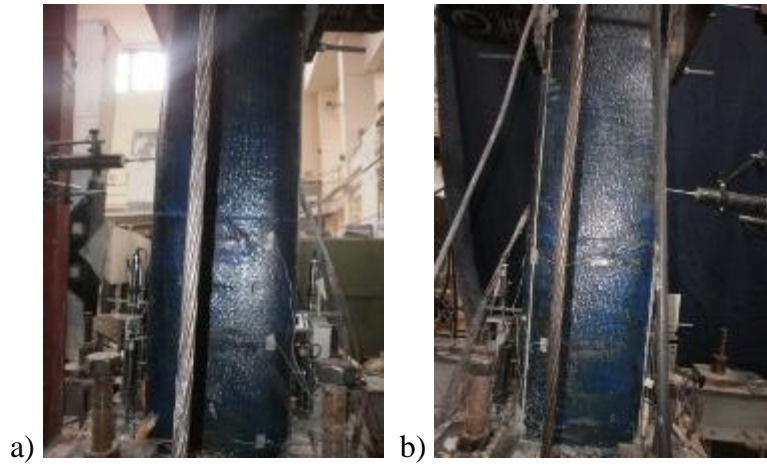
Figure B.76 : a) North, and b) South view of X44-M-CFRP3 after -4.00% mm drift ratio.
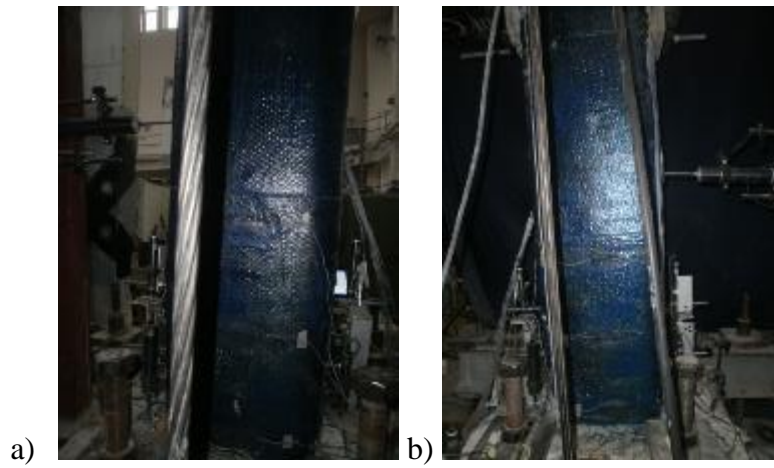

Figure B.77 : a) North, and b) South view of X44-M-CFRP3 after -5.00% mm drift ratio.

Figure B.78 : a) North, and b) South view of X44-M-CFRP3 after test finished.

CURRICULUM VITAE

Name Surname:	ARAS KALYONCUOĞLU
Place and Date of Birth:	17.08.1987 - BAKIRKÖY
Address:	AKBUĞDAY SOK. NO.17 D:3 AVCILAR
E-Mail:	araskalyoncuoglu@gmail.com
B.Sc.:	ANADOLU ÜNİVERSİTESİ
M.Sc.:	İSTANBUL TEKNİK ÜNİVERSİTESİ

PUBLICATIONS/PRESENTATIONS ON THE THESIS

International Reviewed Journal Papers:

A. Kalyoncuoglu, P. Ghaffari, C.Goksu, and A.Ilki, "Rehabilitation of Corrosion-Damaged Substandard RC Columns", Advanced Materials Research, (Volumes 639 - 640), 1096-1103, doi : AMR.639-640.1096

International Conference Papers:

A. Kalyoncuoglu, P. Ghaffari, C.Goksu, and A.Ilki, "Rehabilitation of Corrosion-Damaged Substandard RC Columns", International Conference on Advances in Civil Infrastructure Engineering, September 14-16, 2012, Chang Sha, China.

P. Ghaffari, **A. Kalyoncuoglu**, C.Goksu, and A.Ilki, "A Low-Cost Repair Method for Corrosion Damaged Reinforced Concrete Columns", Vienna Congress on Recent Advances in Earthquake Engineering and Structural Dynamics & 13. D-A-CH Tagung, August 28-30, 2013, Vienna University of Technology, Austria.